DOE/ER-0046/24

Damage Analysis and Fundamental Studies

Quarterly Progress Report
October-December 1985

February 1986

U.S. Department of Energy
Office of Energy Research
Office of Fusion Energy
Washington, DC 20545
B&R No. AT-15-02-03-04

Hanford Engineering Development Laboratory

Operated by
Westinghouse
Hanford Company
for the U.S. DOE

A Subsidiary of
Westinghouse Electric
Corporation

Contract No.
DE-AC06-76FF02170

P.O. Box 1970
Richland, WA 99352

DISCLAIMER

This report was prepared as an account of work sponsored by an agency of the United States Government. Neither the United States Government nor any agency thereof, nor any of their employees, nor any of their contractors, subcontractors or their employees, makes any warranty, express or implied, or assumes any legal liability or responsibility for the accuracy, completeness, or any third party's use or the results of such use of any information, apparatus, product, or process disclosed, or represents that its use would not infringe privately owned rights. Reference herein to any specific commercial product, process, or service by trade name, trademark, manufacturer, or otherwise, does not necessarily constitute or imply its endorsement, recommendation, or favoring by the United States Government or any agency thereof or its contractors or subcontractors. The views and opinions of authors expressed herein do not necessarily state or reflect those of the United States Government or any agency thereof.

Printed in the United States of America
Available from
U.S. Department of Commerce
National Technical Information Service
5285 Port Royal Road
Springfield, VA 22161

NTIS price codes
Printed copy: A 06
Microfiched copy: A01

(12/85)

DOE/ER-OO46/24
uc-20-2oc

Damage Analysis and Fundamental Studies

Quarterly Progress Report
October-December 1985

February 1986

U.S. Department of Energy
Office of Energy Research
Office of Fusion Energy
Washington, DC 2O545
B&R No. AT-15-02-03-04

FOREWORD

This report is the thirty-second in a series of quarterly Technical Progress Reports on *Damage* Analysis and Fundamental Studies (DAFS), which is one element of the Fusion Reactor Materials Program, conducted in support of the Magnetic Fusion Energy Program of the U.S. Department of Energy (DOE). The first eight reports in this series were numbered OOEIET-006511 through 8. Other elements of the Fusion Materials Program are:

- Alloy Development for Irradiation Performance (AOIP)
- Plasma-Materials Interaction (PMI)
- Special Purpose Materials (SPM).

The OAFS program element is a national effort composed of contributions from a number of National Laboratories and other government laboratories, universities, and industrial laboratories. It was organized by the Materials and Radiation Effects Branch, DOE/Office of Fusion Energy, and a Task Group on *Damage Analysis and Fundamental* Studies, which operates under the auspices of that branch. The purpose of this series of reports is to provide a working technical record of that effort for the use of the program participants, the fusion energy program in general, and the OOE.

This report is organized along topical lines in parallel to a Program Plan of the same title so that activities and accomplishments may be followed readily, relative to that Program Plan. Thus, the work of a given laboratory may appear throughout the report. A chapter has been added on Reduced Activation Materials to accommodate work on a topic not included in the early program plan. The Contents is annotated for the convenience of the reader.

This report has been compiled and edited by N. E. Kenny under the guidance of the Chairman of the Task Group on *Damage* Analysis and *Fundamental* Studies, D. G. Doran, Hanford Engineering Development Laboratory (HEOL). Their efforts, those of the supporting staff of HEOL, and the many persons who made technical contributions are gratefully acknowledged. T. C. Reuther, Fusion Technologies Branch, is the DOE counterpart to the Task Group Chairman and has responsibility for the OAFS program within DOE.

G. M. Haas, Chief
Fusion Technologies Branch
Office of Fusion Energy

CONTENTS

Foreword

Page

CHAPTER 1: IRRADIATION TEST FACILITIES

1. RTNS-II IRRADIATIONS AND OPERATIONS (LLNL) 2

Irradiations were performed on nine different experiments during this quarter. The next U.S./Japan Steering Committee meeting will be held February 6 and 7, 1986, at RTNS-II.

CHAPTER 2: DOSIMETRY AND DAMAGE PARAMETERS

1. DOSIMETRY AND DAMAGE ANALYSIS FOR THE HAFNIUM FULL-POWER TEST, JP1, AND JP3 EXPERIMENTS IN HFIR (ANL) 5

Results are reported for the full-power hafnium test for one cycle (22 days) in HFIR. Neutron exposure measurements and damage calculations are similar to the low-power spectral runs reported previously. Analysis has also been completed for the JP1 and JP3 experiments in HFIR. These two experiments had an identical exposure history resulting in a fast (>0.1 MeV) neutron fluence of about 3.9 x 10^{22} n/cm^2 producing 32 dpa and 2147 appm helium in 316 stainless steel.

2. TRANSMUTATIONS IN FUSION TEST FACILITIES (HEDL) 10

Transmutation rates in FFTF, HFIR, STARFIRE, and MARS spectra are compared.

CHAPTER 3: REDUCED ACTIVATION MATERIALS

1. PHASE DEVELOPMENT AND SWELLING IN Fe-Mn AND Fe-Cr-Mn ALLOYS DURING NEUTRON IRRADIATION (HEDL) 22

Second phases form in irradiated Mn-containing iron-based steels, especially at low Cr contents, unlike their Ni-containing counterparts.

2. ACTIVATION CALCULATIONS USING AN EXPANDEO NUCLEAR DATA BASE (HEDL) 30

The water cooling of STARFIRE produces a low energy tail in the neutron spectrum that may impact the use of W in reduced activation alloys intended for service to high fluences.

CHAPTER 4: RADIATION EFFECTS MECHANISMS AND CORRELATIONS

1. OWR/RTNS-II LOW EXPOSURE SPECTRAL EFFECTS EXPERIMENT (HEDL) 38

The first tensile data from OWR are compared to RTNS-II data at 90°C. The data for solution-annealed 316 stainless steel correlate well with dpa; those for copper do not.

2. MICROSTRUCTURAL EXAMINATION OF Fe-Cr BINARY FERRITIC ALLOYS FOLLOWING IRRADIATION TO 15 DPA IN FFTF (HEDL) 43

Six Fe-Cr binary alloys (from 3 Cr to 18 Cr) were irradiated in FFTF at 430°C to 15 dpa. Swelling was highest, 0.26 percent, in the Fe-9Cr alloys with a corresponding dislocation network comprising equal parts of α <100> and $\alpha/2$ <111> Burgers vectors. An example of a deformation slip band containing elongated voids was found which indicates that channel fracture may occur in ferritic alloys that contain uniform void swelling.

Page

3. NUCLEATION OF GRAIN BOUNDARY CAVITIES UNOER THE COMBINED INFLUENCE OF HELIUM AND APPLIED STRESS (U. OF KUWAIT AND U. OF CALIFORNIA-LA) 57

It is shown through modeling that injecting helium to as low as one part per million can result in grain boundary bubble densities on the order of $10^9 cm^{-2}$. Such cavity population exceeds typical grain boundary cavity densities associated with creep experiments. Grain bounddrv bubble densities are shown to reach steady 'state for injected helium amounts on the order of 10 parts per million.

4 NEUTRON-INOUCED SPINOOAL-LIKE OECOMPOSITION OF Fe-Ni AND Fe-Ni-Cr ALLOYS (HEDL) 71

Several new experiments illuminate the nature of the spinodal-like decomposition that occurs during charged particle or neutron irradiation of alloys in the Invar compositional regime.

5. THE INFLUENCE OF UNCERTAINTIES IN MATERIAL PROPERTIES AND THE EFFECTS OF DIMENSIONAL SCALING ON THE PREDICTION OF FUSION STRUCTURE LIFETIMES (U. OF CALIFORNIA-LP) 77

The sensitivity of lifetime predictions for fusion reactor blanket structures is investigated by applying the Monte Carlo numerical technique. Irradiation creep rates are shown to be sufficient for relaxation of swelling-induced stresses under most conditions. A lifetime of several hundred dpa is shown to be highly probable for the MARS blanket design.

CHAPTER 5: FUNDAMENTAL STUDIES OF SPECIAL PURPOSE MATERIALS

1. SWELLING OF PURE COPPEK AND COPPER ALLOYS AFTER HIGH FLUENCE IRRADIATION IN FFTF AT ~450°C (HEDL) 89

Neutron-induced density change data to 47 and 63 dpa at ~450°C fell into two categories--those that exhibit pronounced swellino (often with s-shaped behavior) with dpa level and those that resist' the onset of swelling to very large exposures.

2. NEUTRON IRRADIATION OF COPPER AND HIGH-CONDUCTIVITY COPPER ALLOYS IN EBR-II (LANL AND MIT) 94

The alumina-dispersed copper alloys (Glidcop A1-20 and A1-60) exhibited the greatest resistance to neutron damage (15 dpa at 385°C) among the six materials tested.

CHAPTER 1

IRRADIATION TEST FACILITIES

RTNS-II IRRADIATIONS AND OPERATIONS

D. W. Short and D. W. Heikkinen (Lawrence Livermore National Laboratory)

1.0 Objective

The objectives of this work are operation of RTNS-II (a 14-MeV neutron source facility), mchine development, and support of the experimental program that utilizes this facility. Experimenter services include dosimetry, handling, scheduling, coordination, and reporting. RTNS-II is supported jointly by the U.S. and Japan and is dedicated to materials research for the fusion power program. Its primary use is to aid in the development of models of high-energy neutron effects. Such models are needed in interpreting and projecting to the fusion environment, engineering data obtained in other spectra.

2.0 Summary

Irradiations were performed on nine different experiments during this quarter. HEDL furnace was removed from the left target room. Terminal isolation transformer was replaced on the left machine. The next U.S./Japan Steering Committee meeting will be held February 6 and 7, 1986 at RTNS-II.

3.0 Program

Title: RTNS-II Operations (WZJ-16)
Principal Investigator: D. W. Short
Affiliation: Lawrence Livermore National Laboratory

4.0 Relevant DAFs Program Plan Task/Subtask

TASK II,A,2,3,4,
TASK II,B,3,4
TASK II,C,1,2,6,11,18,

5.0 Irradiation

During this quarter, irradiations (both dedicated and add-on) were done for the following people.

Experimenter	P or A*	Sample Irradiated
D. Heikkinen (LLNL)	A	Nb - dosimetry calibration
H. Heinisch (HEDL) G. Pells (Harwell) F. Clinard (LANL) M. Kiritani (Hokkaido) R. Ohshima (Osaka) H. Yoshida (Kyoto) K. Abe (Tohoku) H. Matsui (Tohoku) H. Kayano (Tohoku) H. Kawanishi (Tokyo) N. Iqata (Tokyo) Y. Shimomura (Hiroshima) N. Yoshida (Kyushu)	P	Metals - displacement damage & mechanical properties. Ceramics - neutron damage - irradiated at 90°C and 290°C

Experimenter	P or A*	Sample Irradiated
A. Kohyama (Tokyo) S. Nanao (Tokyo) H. Kawanishi (Tokyo) K. Miyahara (Tokyo) M. Kiritani (Hokkaido) H. Takahashi (Hokkaido) K. Abe (Tohoku) Y. Higasiguchi (Tohoku) H. Kayano (Tohoku) K. Okamura (Tohoku) H. Matsui (Tohoku) M. Hasegawa (Tohoku) K. Ono (Hiroshima) N. Yoshida (Kyushu)	P	Metals - displacement damage & mechanical properties. Ceramics - neutron damage - irradiated at room temperature.
K. Kawamura	A	$Pd_{80}Si_{20}$ - Property change
M. Kiritani/T. Yoshiie (Hokkaido)	P	Ni, Au, Ag, Cu & Fe - cascade damage
S. Iwasaki (Tohoku)	A	$^{27}Al(n,2n)$ - cross section
S. Iwasaki (Tohoku)	A	SS & Ni alloy - tensile
E. Goldberg (LLNL)	A	Al-^{24}Na calibration source
T. Yoshiie (Hokkaido)/ H. Kawanishi (Tokyo) A. Kohyama (Tokyo) K. Miyahara (Tokyo) S. Ishino (Tokyo) M. Kiritani (Hokkaido) H. Takahashi (Hokkaido) K. Abe (Tohoku) H. Kayano (Tohoku) K. Okamura (Tohoku) H. Matsui (Tohoku) N. Yoshida (Kyushu) C. Kinoshita (Kyushu) K. Kamata (Nagoya) K. Saka (Nagoya) M. Iseki (nagoya) K. Hirata (Osaka) R. Oshima (Osaka) Y. Shimomura (Hiroshima) T. Kino (Hiroshima) H. Yoshida (Kyoto) H. Heinisch (HEDL) F. Clinard (LANL)	P	Metals - displacement damage & mechanical properties. Ceramics - neutron damage - irradiated at 200° and 450°C

*P = Primary, A = Add on

5.1 RTNS-II Status - W. Short and D. W. Heikkinen

HEDL Furnace removed from left machine.
Terminal isolation transformer replaced on the left machine.
Both neutron sources operated on a near 24/hr, 5-day week schedule.

6.0 Future Work

Irradiations will be continued for D. Heikkinen (LLNL), T. Yoshiie (Hokkaido)/H. Kawanishi (Tokyo) et al. and G. Goldberg (LLNL). Also during this period, irradiations for M. Sugisaki (Kyushu), M. Guinan/J. Huang (LLNL), R. Borg (LLNL), H. Vonach (Vienna), Y. Shimomura (Hiroshima) et al. and K. Tanimura/N. Itoh (Nagoya) will be initiated.
The Sixth U.S./Japan Steering Committee Meeting will be held February 6 and 7, 1986 at RTNS-II.
Operations will begin to be reduced toward the end of next quarter.

CHAPTER 2

DOSIMETRY AND DAMAGE PARAMETERS

DOSIMETRY AND DAMAGE ANALYSIS FOR THE HAFNIUM FULL-POWER TEST, JP1, AND JP3 EXPERIMENTS IN HFIR

L. R. Greenwood (Argonne National Laboratory)

1.0 Objective

To characterize material experiments in terms of neutron fluence, spectra, and damage parameters (dpa, gas).

2.0 Summary

Results are reported for the full-power hafnium test for one cycle (22 days) in HFIR. Neutron exposure measurements and damage calculations are similar to the low-power Spectral runs reported previously. Analysis has also been completed for the JP1 and JP3 experiments in HFIR. These two experiments had an identical exposure history resulting in a fast 00.1 MeV) neutron fluence of about 3.9 X 10^{22} n/cm^2 producing 32 dpa and 2147 appm helium In 316 stainless steel. The status of all other experiments is reported in Table 1.

3.0 Program

Title: Dosimetry and Damage Analysis
Principal Investigator: L. R. Greenwood
Affiliation: Argonne National Laboratory

4.0 Relevant DAFS Program Plan Task/Subtask

Task II.A.l Fission Reactor Dosimetry

5.0 Accomplishments and Status

5.1 Full-Power Hafnium Tests in HFIR-RB Position

Results were reported previously[1] for tests of a hafnium shield to reduce the thermal neutron flux in the RB position of HFIR. These low-power (~11 MW) experiments for one hour allowed us to make spectral measurements employing our full range of dosimetry materials including short-lived products, fissile materials, and thermal shields. The present measurements were performed at full power (100 MW) for one reactor cycle (22 days) for 2350 MWH from August 10 to September 3, 1985 in order to validate our previous results in the normal range of HFIR operations.

Two dosimetry tube9 were irradiated. one in the hafnium sleeve in the RB-1 position and one in aluminum in the RB-3 position. Each tube measured 3.2 mm O.D. x 55.6 cm in length and each was located in the center of the RB assemblies. Smaller dosimetry tubes were also located on the outside of the assemblies in order to measure the radial flux gradients in the RB positions. The main dosimetry tubes contained Fe, Ni. Ti. Cu, Nb. Al, Co, Mn, Zn, Cr, Mo, and V dosimeters and helium gas monitors (Rockwell International). After irradiation all of the samples were gamma counted at Argonne and selected samples were sent to Rockwell for helium analysis.

The measured activation rates are listed in Table 2. The midplane values Were determined by fitting the data at eight different vertical heights to our equation:

$$f(z) = a\,(1 + bz + cz^2)$$

where a = midplane value, b = 1.80 X 10^{-3}, c = -1.20 X 10^{-3}, and z = height in cm. The radial activities show an interesting pattern. The thermal flux is nearly constant while the fast neutron flux is falling rapidly (44%) from the inner to the outer surface. a distance of about 3 cm. This radial gradient will clearly produce a significant gradient in the damage production radially across material samples.

The midplane activities were used to adjust the neutron flux spectrum determined previously[1] in our spectral measurements. The results of this STAY'SL analysis are listed in Table 3. Comparison to our previous low-power runs indicates a small spectral shift. The full-power fast flux is about 6% lower than at low power; however. the thermal flux is about 11% higher in the bare case and only 4% higher in the hafnium case. On balance, the total flux is about the Same in the 11 MW and 100 MW irradiations and the small spectral differences may be due to the presence of the hafnium.

Table 1. Status of Dosimetry Experiments

Facility/Experiment		Status/Comments
ORR	- MFE 1	Completed 12/79
	- MFE 2	Completed 06/81
	- MFE 4A1	Completed 12/81
	- MFE 4A2	Completed 11/82
	- MFE 4B	Completed 04/34
	- MFE 4A3, 4B2	Samples received 11/85
	- TRC 07	Completed 07/80
	- TRIO-Test	Completed 07/82
	- TRIO-1	Completed 12/83
	- HF Test	Completed 03/84
	- J6 Test	Completed 07/85
	- J6, J7	Irradiations in Progress
HFIR	- CTR 32	Completed 04/82
	- CTR 31, 34, 35	Completed 04/83
	- T2, RB1	Completed 09/33
	- T1, CTR 39	Completed 01/84
	- CTR 40-45	Completed 09/84
	- CTR 30, 36, 46	Completed 03/85
	- RB2	Completed 06/85
	- CTR 47-56	Irradiations in Progress
	- JP1, JP3	Completed 12/85
	- JP 2-8	Irradiations il Progress
	- Hf Spectral Analysis	Completed 09/85
	- Hf Test	Completed 12/85
Omega West	- Spectral Analysis	Completed 10/80
	- HEDL1	Completed 05/81
	- HEDL2	Samples Sent 04/85
	- LRNL 1	Completed 03/84
EBR II	- X287	Completed 09/31
IPNS	- Spectral Analysis	Completed 01/82
	- LANL 1 (Hurley)	Completed 06/82
	- Hurley	Completed 02/83
	- Coltman	Completed 08/83

In any case, these adjusted spectra produce a small shift in the damage parameters calculated with SPECTER, as listed in Table 4. For a I-year irradiation (365 FPD), we estimate damage rates of 11.3 (bare) to 8.9 (Hf) dpa in 316 SS wlth a helium production of 854 (bare) to 26.5 (Hf) appm. In other words, the hafiium reduces the yearly helium production by a factor of 32 while the damage rate only falls by 20%. Whether or not this reduction is sufficient for planned materials experiments is now being evaluated at Oak Ridge National Laboratory.

5.? Results of the JP1 and JP3 Experiments in HFIR

The JP1 and JP3 experiments are par? of a U.S./Japanese collaboration described in previous reports.[2] Both experlments were Irradiated for very nearly the same exposure in the target position of HPIR. JP1 was lrradiated for 33,634 MWd between January 4, 1984 and February 1, 1984, whlle JP3 was irradiated for 34,009 MWd between May 1, 1984 and May 28, 1985.

Table 2. Activation Rates for Hf Test in HFIR-RB
Midplane values at full power (100 MW)

Reaction	Activation Rate, at/at-s Hf	Bare
$^{58}Fe(n,\gamma)\ ^{59}Fe(x\ 10^{-10})$	1.14	10.11
$^{59}Co(n,\gamma)\ ^{60}Co(x\ 10^{-8})$	0.452	3.25
$^{54}Fe(n,p)\ ^{54}Mn(x\ 10^{-11})$	1.34	1.51
$^{46}Ti(n,p)\ ^{46}Sc(x\ 10^{-12})$	1.88	2.09
$^{63}Cu(n,\gamma)\ ^{60}Co(x\ 10^{-14})$	9.19	10.00
$^{55}Mn(n,2n)\ ^{54}Mn(x\ 10^{-14})$	4.28	4.67

Radial Activity Gradients

Values are listed at three vertical heights on the outer surfaces of the hafnium tube.

Reaction	-15.0 cm		0.2 cm		+15.5 cm	
	Inner	Outer	Inner	Outer	Inner	Outer
$^{58}Fe(n,\gamma)\ ^{59}Fe(x\ 10^{-10})$	6.17	7.16	11.32	10.58	6.28	6.63
$^{59}Co(n,\gamma)\ ^{60}Co(x\ 10^{-8})$	2.32	2.35	3.13	3.56	2.49	2.56
$^{54}Fe(n,p)\ ^{54}Mn(x\ 10^{-11})$	1.23	U.714	1.92	I.02	1.20	0.671
$^{46}Ti(n,p)\ ^{46}Sc(x\ 10^{-12})$	1.84	1.04	2.73	1.53	-	1.10

Table 3. Neutron Fluxes for HFIR-RB-Hf Test
Midplane values at full power (100 MW)

Energy, MeV	Neutron Flux, $x\ 10^{14}$ n/cm^2-s Hf	Bare
Total	9.61	24.77
Thermal (<0.5 eV)	1.14	11.07
0.5 eV - 0.1 MeV	3.78	8.53
>0.1 MeV	4.15	5.17

Dosimetry capsules Were placed at six different vertical heights in each experiment. Each capsule measured about 0.05-in. O.D. x 0.25-in. length and contained Fe, Co, Mn, and Ti wires. The uppermost dosimeters could not be retrieved and the Ti wires were not usable due to severe oxidation. The remaining samples were gamma counted and the resultant activation rates are listed in Table 5. As can be seen, there is virtually no difference between the two experiments. Consequently, the results were averaged for subsequent flux adjustments and damage calculations.

The Vertical activity gradients are well-described by our equation determined in the nearby PTP position, as follows:

$$f(z) = a\ (1 + bz + cz^2) \qquad (1)$$

where a = midplane value, b = 5.02 x 10^{-4}, c = -1.00 x 10^{-3}, and z = vertical height (cm). Comparison of these results to those reported previously[3] in the nearby PTP position indicates a slight spectral shift. In the present case, the thermal flux is about 9% higher while the fast flux is about 5% lower than in the PTP positions. This shift is expected since we are about 1-2 cm further into the central target region; however, differences in the capsule designs may also have an influence.

Neutron flux, fluence, and damage rates were calculated using the STAY'SL and SPECTER computer codes and the results are listed in Tables 6 and 7. These values represent the conditions at midplane and values at other vertical heights can be determined using Eq. 1 above. Helium production and displacement damage in nickel and stainless steel is listed separately in Table 8. Thermal damage effects are also listed for copper in Table 6. In the copper case the helium production is increased by a factor of 7.5 due to the three-stage reaction through ^{65}Zn.

Table 4. Estimated Yearly Fluence and Damage Parameters for HFIR-RB Position
Midplane values for 365 FPD at 100 MW

		Hf		Bare	
Fluence >0.1 MeV		1.50×10^{22}		1.63×10^{22} n/cm^2	
Element		DPA	He, appm	DPA	He, appm
Al		11.2	4.21	19.1	4.52
Ti		9.6	3.68	11.2	4.01
V		11.3	0.14	13.0	0.15
Cr		9.6	1.03	10.9	1.13
Mn[a]		10.4	0.87	12.8	0.94
Fe		8.5	1.84	9.6	1.99
Co[a]		9.6	0.87	13.1	0.94
	Fast	9.5	26.5	10.9	29.0
Ni	^{59}Ni	0.3	166.1	11.5	6528.0
	Total	9.8	193.2	22.4	6551.0
	Fast	8.5	1.26	9.1	1.36
Cu	^{65}Zn	-	0.02	0.01	1.21
	Total	8.5	1.28	9.11	8.57
Nb		8.8	0.34	9.6	0.38
Mo		6.8	-	1.5	-
316 SS[b]		8.9	26.5	11.3	854.0

[a] Thermal neutron self-shielding may reduce damage in Mn, Co.

[b] 316 SS: Fe(0.645), Ni(0.13), Cr(0.18), Mn(0.019), Mo(0.026).

Table 5. Activation Rates for HFIR-JP1, JP3
Values normalized to 100 MW

	Activation Rate, at/at-s							
	^{58}Fe(n,p) ^{59}Fe ($\times 10^{-9}$)		^{59}Co(n,p) ^{60}Co ($\times 10^{-8}$)		^{54}Fe(n,γ) ^{54}Mn ($\times 10^{-11}$)		^{55}Mn(n,2n) ^{54}Mn ($\times 10^{-12}$)	
Height. cm	JP1	JP3	JP1	JP3	JP1	JP3	JP1	JP3
16.5	1.73	1.72	5.41	5.60	4.91	5.02	1.41	1.51
1.1	2.14	2.15	6.21	1.02	6.52	6.51	1.96	2.00
2.1	2.29	2.28	6.49	1.36	6.44	6.85	2.01	2.01
-12.1	1.96	1.96	5.10	6.36	5.61	5.68	1.70	1.66
-21.0	1.41	1.31	4.51	4.60	3.19	3.14	1.13	1.15

6.0 References

1 L. R. Greenwood, Damage Analysis and Fundamental Studies Quarterly Progress Report, DOE/ER-0046/23, 1985.

2 J. L. Scott and M. P. Tanaka. Alloy Development for Irradiation Performance, Semiannual Progress Report, DOE/ER-0045/14, pp. 10-19, July 1985.

3 L. R. Greenwood. ibid. pp. 22-26. July 1985.

7.0 Future Work

Dosimeters have been received from the MFE4A and MFE4B experiments which have now been concluded in the Oak Ridge Research Reactor. Analysis is in progress.

Table 6. Neutron Flux and Fluences for HFIR-JP1, JP3
Exposure about 340 MWd at 100 MW

Energy. MeV	Flux (x 10^{15} n/cm^2-s)	Fluence (x 10^{22} n/cm^2)
Total	5.18	15.2
Thermal (<0.5 eV)	2.24	6.57
0.5 eV - 0.1 MeV	1.62	4.76
Fast 00.1 MeV)	1.32	3.88

Table 7. Damage Parameters for HFIR-JP1, JP3
Midplane Values at 340 FPD (100 MW)

Element		DPA	He, appm
Al		49.6	24.0
Ti		31.6	15.9
V		35.4	0.81
Cr		31.1	5.50
Mn[a]		34.5	4.86
Fe		27.5	9.76
Co[a]		35.4	4.81
	Fast	29.7	12R.0
Ni	^{59}Ni	28.8	16331.0
	Total	58.5	16459.0
	Fast	26.9	7.1
cu	^{65}Zn	0.1	45.8
	Total	27.0	52.9
Nb		26.6	1.78
Mo		19.8	-
316 SS		32.1	2147.0

[a] Thermal neutron self-shielding may reduce damage in Mn. Co.

[b] 316 SS: Fe(0.645), Ni(0.13), Cr(0.18), Mn(0.019), Mo(0.026).

Table 8. Helium and DPA for 316 SS in HFIR JP1, JP3

He includes ^{59}Ni and fast reactions
DPA includes extra kick from thermals (He/567)

Height, cm	He, appm	DPA
0	2147.	32.1
3	2125.	31.8
6	2062.	31.0
9	1954.	29.5
12	1802.	27.5
15	1603.	24.8
18	1357.	21.6
21	1063.	17.7
24	727.	13.3

TRANSMUTATIONS IN FUSION TEST FACILITIES

F. M. Mann (Hanford Engineering Development Laboratory)

1.0 Objective

The objective of this work is to determine how typical materials transmute in various fusion test facilities.

2.0

Using an expanded nuclear data base, the transmutation of PCA, AMCR33 (a reduced activation austenitic steel), HT-9, RAFER2 (a reduced activation ferritic steel), V-15%Cr-5%Ti alloy, and SiAlON (a ceramic) were calculated for two positions in the Fast Flux Test Facility (FFTF), three positions in the High Flux Isotope Reactor (HFIR), and the first wall position of both the STARFIRE and MARS conceptual fusion reactors. The peripheral test (PTP) position, and to a lesser extent the radial beryllium (RB) position, of HFIR show significant transmutations which are often in the opposite direction to the transmutations in the fusion conceptual designs. The positions in FFTF, as well as the hafnium-covered location in the HFIR RB position, show relative minor transmutations.

3.0 Program

Title: Irradiation Effects Analysis
Principal Investigator: D. G. Ooran
Affiliation: Westinghouse Hanford Company

4.0 Relevant Program Plan Task/Subtask

II.A.4	Gas Generation Rates
II.C.4 and II.C.10	Effects of Solid Transmutants

5.0 Accomplishments and Status

5.1 Introduction

Because no facility exists which has a spectrum similar to that expected in a fusion reactor, existing fission reactors are being used to test the behavior of materials. Although it is believed that the change in material behavior will be most sensitive to displacement damage, the transmutation of composition has long been considered important. The major effort is in the gaseous transmutation products. particularly helium. However, now the importance of solid transmutants is being raised. Also, it is becoming realized that the transmutations in thermal reactors can be very large and can completely distort the composition of a material.

To determine the compositional change in typical fusion materials, calculations were performed for the first wall positions of two conceptual fusion designs and for positions in high flux test reactors used by the fusion materials program. The materials were chosen to be candidate first wall materials, an insulator, and various elements to provide a broad treatment of possible material combinations. For the first wall candidates, reduced activation versions were also included.

5.2 Description of the Calculations

To gain insight into the behavior in a fusion facility, the first wall positions of the STARFIRE and MARS conceptual designs were chosen. Because of its use of water as a coolant, STARFIRE has a strong 1/E low energy neutron flux shape. The MARS design, on the other hand, has relatively few low energy neutrons. Most of the high fluence irradiations for the fusion materials program will be in the FFTF or the HFIR. Therefore, two positions were chosen in the FFTF. one at core center [comparable to the midplane (or highest flux) position of the Material Open Test Assembly (MOTA)], and the other at the midplane position of the outer row (which is similar to the top of the MOTA). Calculations for three positions in HFIR were also performed, the first corresponding to the PTP, the second to a radial beryllium (RB) position, and the last to a hafnium shielded radial beryllium (RB-Hf) position. The fluxes for the last two positions (RB and RB-Hf) were kindly supplied by L. Greenwood (Argonne National Laboratory) from his dosimetry measurements, while fluxes for the other positions were taken from the standard REAC flux library.

The cross section and decay data needed for the calculations were taken from the newly expanded REAC libraries.[1] It should be noted that for many of the reactions, the needed cross sections were estimated.

The REAC computer code system[2] was used to calculate the change in composition for a six-year exposure at each position. For the HFIR positions, time steps were taken to be 0.125 year; for the other positions time steps were taken to be 0.25 year. The materials included in the calculation are PCA, VCrTi, HT-9, AMCR33 (a reduced activation austenitic), RAFER2 (a reduced activation ferritic), CuBe, Sialon, Be, C, Al, Si, Cu, Mo, Nb, and W.

5.3 Results of the Calculations

Tables 1 through 15 give the results of the calculations for an exposure of five years. Figures 1 and 2 show the change of V in HT-9 and the change of Mn in RAFER2, respectively, as a function of exposure.

In general, the most significant transmutations occur for the PTP position of HFIR, particularly for odd mass and for high mass nuclei. The RE positions of HFIR often show similar but smaller changes than the PTP positions. The hafnium-covered RB position (like the FFTF positions) shows practically no change in composition. The first wall positions show little change. The most notable changes in composition at a five-year exposure are: (1) the large burnout of Mn in HFIR (for PTP and RB) contrasted to the increase shown for STARFIRE and MARS for PCA, (2) the switch in composition from 80%V 15%Cr 5%Ti to 12%V 67%Cr 5%Ti again at the PTP position, (3) the 1300% increase in iron in VCrTi for PTP, (4) the 200% increase of Mn in HT-9 in the fusion designs, (5) the burnout of Mn (which replaces Ni in the reduced austenitic AMCR33) in PTP from an initial 15% to 1.5%, and (6) the transformation of N (initially 36%) to C (ending will be 18%) for Sialon in PTP. Various new elements are also created. How significant these additions are depends upon their metallurgical importance.

It should be noted some of the compositional changes are not linear functions of time. Vanadium in HT-9 (see Figure 1) shows this quite dramatically for the PTP position in HFIR. The amount of V first increases (as it does for all the positions studied), but then in the PTP position, the vanadium burns out.

5.7 Conclusion

Whenever materials are exposed to a significant fluence in the PTP position in HFIR, the compositional change of the material should be investigated. However, other facilities (including fusion devices) also show some large changes for certain materials.

6.0 References

1. F. M. Mann, "Cross Sections for Reduced Activation Studies", OAFS Quarterly Progress Report, DOE/ER-0046/20, February 1985, p. 18.

2. F. M. Mann, "Transmutation of Alloys in MFE Facilities as Calculated by REAC (A Computer Code System for Activation and Transmutation", HEDL-TME-81-37, Westinghouse Hanford Company.

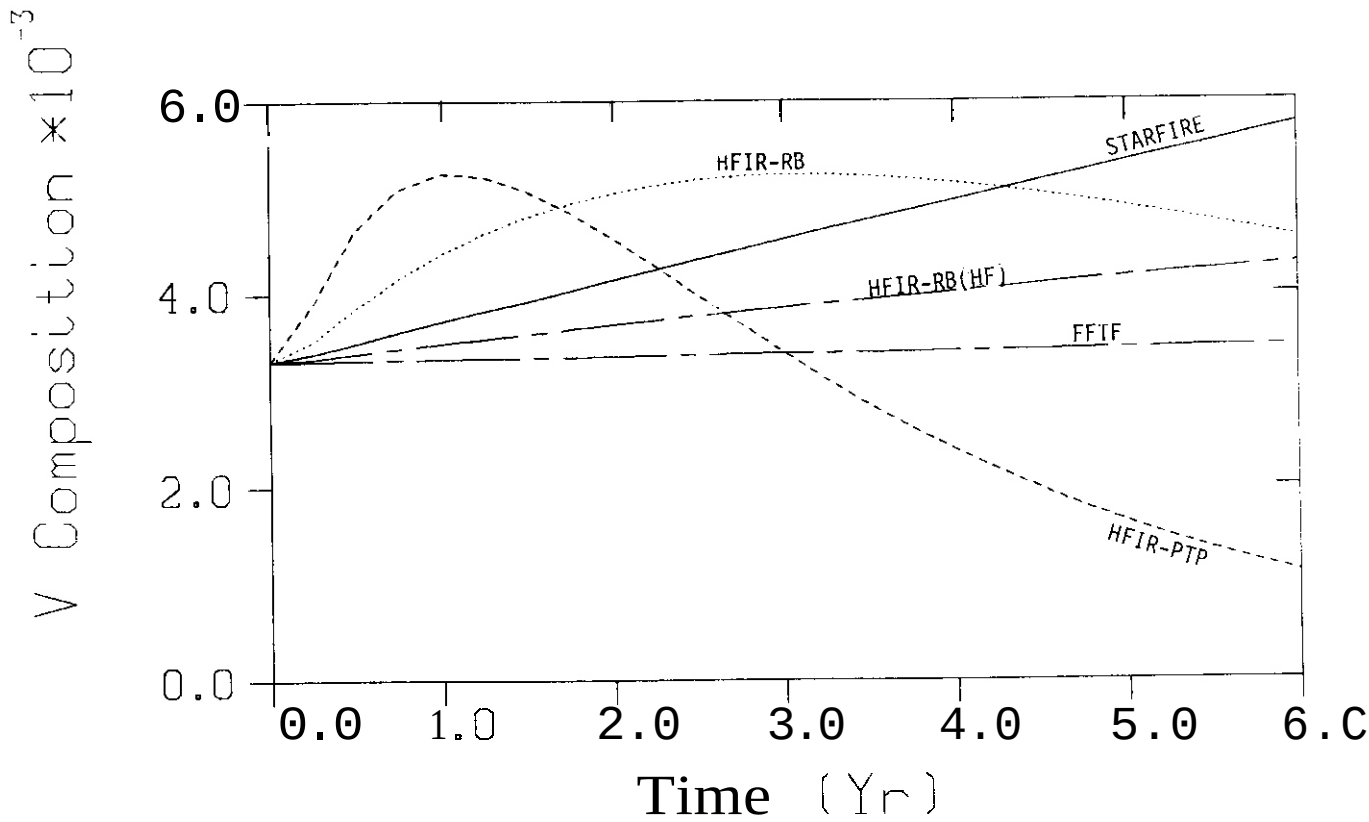

FIGURE 1. The Amount of V in HT-9 as a Function of Time in STARFIRE, FFTF, and Three Positions in HFIR.

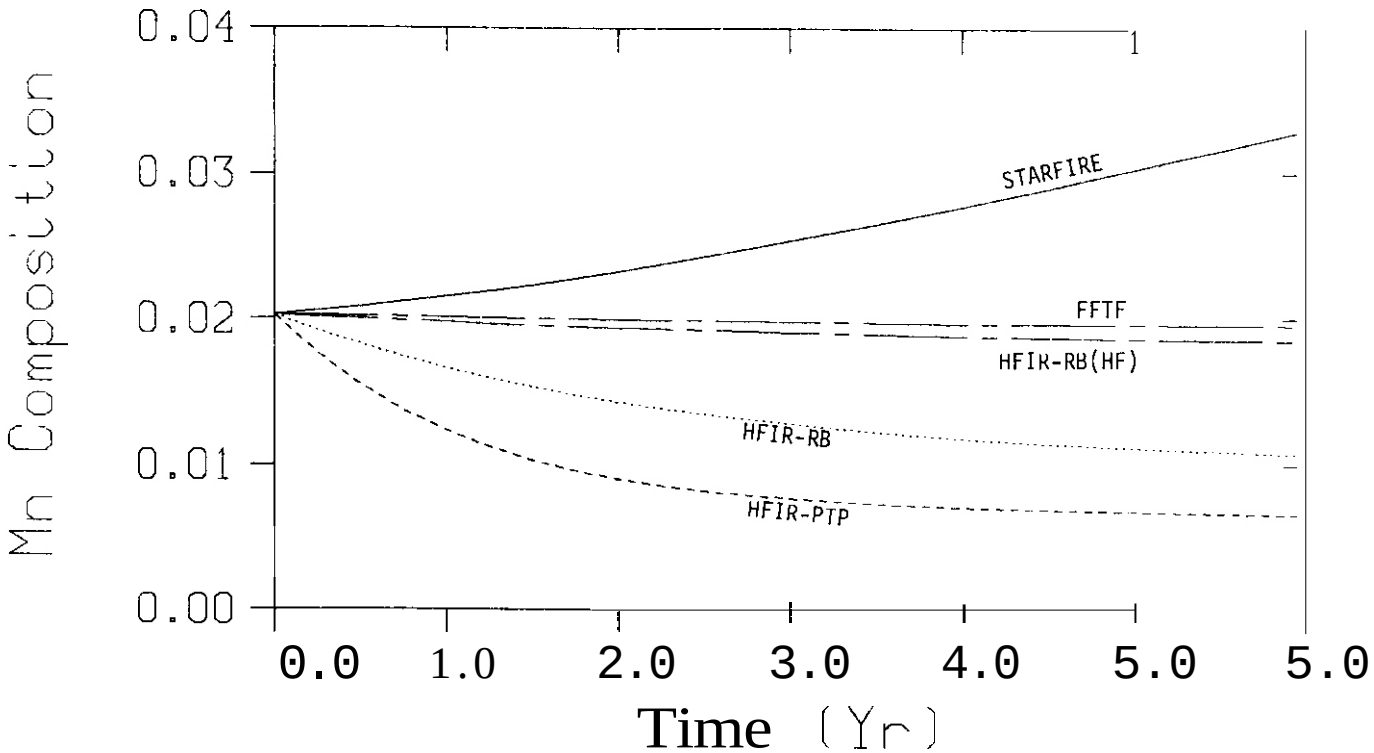

FIGURE 2. The Amount of Mn in RAFER2 as a Function of Time in STARFIRE, FFTF, and Three Positions in HFIR.

TABLE 1

TRANSMUTATIONS IN PCA AFTER 5 YEARS IN 7 FUSION TEST FACILITIES

Fractional Change (%) in Initial Constituents

Element	Initial Amount	FFTF 2101	FFTF 2909	HFIR PTP	HFIR RB4	HFIR RB4(HF)	First Wall STARFIRE	First Wall MARS
Fe	0.651	0.36	0.13	0.55	2.16	0.39	0.41	0.75
Ni	0.152	-1.52	-0.02	-14.0	-5.3	-0.88	-5.6	-5.6
Cr	0.150	0.10	-0.06	-4.0	-2.85	-0.77	-0.43	-0.30
Mn	0.0190	-3.4	-4.6	-66.0	-48.0	-8.7	39.0	51.0
Mo	0.0116	-3.8	-1.03	-7.1	-2.83	-0.91	-2.72	-2.01
Si	0.0099	-0.02	-0.00	-0.14	-0.04	-0.01	-1.36	-1.37
Ti	0.0035	0.15	-0.00	-0.13	-0.14	0.01	14.8	15.2
C	0.0028	-0.03	-0.00	-0.02	-0.00	0.00	-1.33	-1.34

New Elements (parts per thousand)

Element	FFTF 2101	FFTF 2909	HFIR PTP	HFIR RB4	HFIR RB4(HF)	First Wall STARFIRE	First Wall MARS
H	2.8	0.009	3.6	1.49	0.66	17.4	17.6
He	0.170	0.016	11.5	6.1	0.60	3.1	2.97
Be	0.001		0.001			0.011	0.011
Mg	0.001		0.001			0.049	0.049
Al						0.085	0.086
P	0.001		0.012	0.004	0.001		
Ca						0.002	0.002
Sc						0.004	0.004
V	0.201	0.086	1.45	3.8	1.37	2.57	2.31
Co	0.219	0.013	20.4	2.55	0.178	1.25	1.29
cu		0.006	12.0	0.96	0.055	0.018	0.004
Zn			2.37	0.059	0.001		
Ga			0.019				
Ge			0.06				
Sr						0.001	0.001
P						0.004	0.004
Zr						0.020	0.019
Nb						0.050	0.057
Tc	0.262	0.078	0.44	0.199	0.073	0.016	0.108
Ru	0.136	0.030	0.285	0.093	0.021	0.046	0.021
Rh	0.001		0.014	0.002			
Pd			0.005				

TABLE 2

TRANSMUTATIONS IN VCrTi AFTER 5 YEARS IN 7 FUSION TEST FACILITIES

Fractional Change (%) in Initial Constituents

E	Initial Amount	FFTF 2101	FFTF 2909	HFIR PTP	HFIR RB4	HFIR RB4(HF)	First Wall STARFIRE	First Wall MARS
V	0.797	-1.22	-0.50	-85.0	-46.0	-7.6	-2.20	-0.40
Cr	0.146	6.6	2.70	460.0	248.0	41.0	9.3	-0.51
Ti	0.0528	0.07	-0.00	-1.28	-0.17	-0.01	7.1	7.2
N	0.00189	2.66	-0.17	-50.0	-20.0	-3.2	-2.98	-2.81
O	0.00073	-0.13	-0.00	-0.15	-0.03	-0.03	-1.33	-1.32
C	0.00072	3.7	0.44	128.0	52.0	7.8	5.0	4.3
Fe	0.00050	-0.10	-0.02	1270.0	36.0	0.14	-1.71	-1.80
Mo	0.00030	-0.38	-1.03	-7.1	-2.82	0.91	-2.73	-2.01
cu	0.00005	-5.8	-2.07	-66.0	-36.0	-6.4	-7.6	-4.9

TABLE 2 (Cont'd)

New Elements (parts per thousand)

Element	FFTF 2101	FFTF 2909	HFIR PTP	HFIR RB4	HFIR RB4(HF)	First Wall STARFIRE	First Wall MARS
H	0.174	0.004	1.07	0.40	0.083	5.3	5.3
He	0.037		0.035	0.009	0.007	1.32	1.33
Ot						0.003	0.003
Be						0.003	0.003
8	0.025		0.020	0.005	0.005	0.017	0.019
Ca	0.001		*0.001*			0.033	0.033
Sc	0.001					0.065	0.067
Mn	0.006	0.001	7.6	0.55	0.021	0.012	0.009
co			0.023	0.001			
Ni	0.001	0.001	0.018	0.009	0.002	0.003	0.002
Zn	*0.001*		0.008	0.003			
Zr						0.001	
Nb						0.001	0.001
Tc	0.007	0.002	0.011	0.005	0.002	0.004	0.003
Ru	0.004	0.001	0.007	0.002	0.001	0.001	0.001

TABLE 3

TRANSMUTATIONS IN HT-9 AFTER 5 YEARS IN 7 FUSION FACILITIES

Fractional Change (%) in Initial Constituents

Element	Initial Amount	FFTF 2101	FFTF 2909	HFIR PTP	HFIR RB4	HFIR RB4(HF)	First Wall STARFIRE	First Wall MARS
Fe	0.840	-0.09	0.01	-3.5	-0.34	-0.04	-1.68	-1.77
Cr	0.122	0.27	-0.04	-1.68	-1.58	-0.64	0.14	0.17
C	0.0092	-0.03	-0.00	-0.02	-0.00	-0.00	-1.33	-1.34
Si	0.0078	0.03	0.00	-0.07	-0.03	0.00	-1.21	-1.21
Mo	0.0057	-3.8	-1.03	-7.1	-2.82	4.7	-2.72	-2.01
Mn	0.0055	5.2	-2.00	14.9	14.6	-0.90	211.0	228.0
Ni	0.0047	-1.52	-0.01	154.0	1.70	-0.71	-5.6	-5.6
V	0.0033	3.8	1.62	-50.0	49.0	26.0	62.0	58.0
W	0.0015	-17.5	-29.2	-90.0	-59.0	-35.0	-36.0	-10.0
P	0.0003	-0.35	-0.03	-3.9	-1.31	-0.21	-1.92	-1.92
S	0.0003	-0.67	0.03	5.1	1.93	0.13	-2.09	-2.23

New Elements (parts per thousand)

Element	FFTF 2101	FFTF 2909	HFIR PTP	HFIR R84	HFIR RB4(HF)	First Wall STARFIRE	First Wall MARS
H	0.85	0.002	0.75	0.189	0.171	12.3	12.4
He	0.078	0.001	0.42	0.206	0.032	2.33	2.34
Be	0.002		0.002			0.036	0.036
Mg	0.001		0.001			0.039	0.039
Al						0.067	0.068
Cl			0.001				
Ti	0.005		0.007	0.001	0.001	0.44	0.45
co	0.035		24.6	2.27	0.056	0.065	0.045
cu	*0.001*		0.493	0.030	0.002	*0.001*	
Zn			0.083	0.002			
Ga			0.001				
Sr						0.001	0.001
Y						0.002	0.002
Zr						0.010	0.010
Nb						0.025	0.028
Tc	0.129	0.038	0.214	0.098	0.036	0.080	0.053
Ru	0.067	*0.015*	0.140	0.046	0.010	0.023	*0.010*

TABLE 3 (Cont'd)

New Elements (parts per thousand)

Element	FFTF 2101	FFTF 2909	HFIR PTP	HFIR RB4	HFIR RB4(HF)	First Wall ~ F	First Wall R E MARS
Rh	0.001		0.007	0.001			
Pd			0.003				0.001
Ta	0.001	0.001				0.003	0.033
Re	0.176	0.233		0.233	0.111	0.210	0.108
os	0.083	0.183	0.118	0.119	0.191	0.241	0.008
Ir		0.016	0.65	0.278	0.167	0.066	
Pt		0.002	0.079	0.112	0.045	0.015	
Au				0.006			
Hg			0.33	0.109			
Tl			0.37	0.003			
Pb			0.059				

TABLE 4

TRANSMUTATIONS IN AMCR33 AFTER 5 YEARS IN 7 FUSION TEST FACILITIES
(AMCRSS IS A REDUCED ACTIVATION AUSTENITIC ALLOY)

Fractional Change (%) in Initial Constituents

Element	Initial Amount	FFTF 2101	FFTF 2909	HFIR PTP	HFIR RB4	HFIR RB4(HF)	First Wall ~ F	First Wall R E MARS
Fe	0.777	1.18	1.12	15.7	13.5	2.59	0.48	-1.70
Mn	0.155	-5.8	-5.2	-91.0	-65.0	-12.1	-6.1	3.4
Cr	0.107	0.24	-0.06	-3.9	-2.83	-0.85	3.5	3.8
Si	0.0107	-0.02	-0.00	-0.01	-0.04	-0.01	-1.37	-1.37
C	0.0048	-0.03	-0.00	-0.02	-0.00	-0.00	-1.34	-1.35
Ni	0.0005	-1.49	0.05	1480.0	53.0	-0.29	-5.3	-5.6

New Elements (parts per thousand)

Element	FFTF 2101	FFTF 2909	HFIR PTP	HFIR RB4	HFIR RB4(HF)	First Wall STARFIRE	First Wall MARS
H	0.69	0.001	0.60	0.135	0.138	10.9	11.0
He	0.065		0.105	0.035	0.014	2.12	2.14
Be	0.001		0.001			0.018	0.019
Mg	0.001		0.001			0.053	0.053
Al						0.093	0.093
P	0.001		0.013	0.004	0.001		
Ti	0.004		0.006	0.001	0.001	0.38	0.38
V	0.145	0.061	1.01	2.73	0.98	1.88	1.70
co	0.024	0.010	23.3	2.01	0.043	0.026	0.008
cu			0.150	0.003			
Zn			0.017				

TABLE 5

TRANSMUTATIONS IN RAFER2 AFTER 5 YEARS IN 7 FUSION TEST FACILITIES
(RAFER2 IS A REOUCEO ACTIVATION FERRITIC ALLOY)

Fractional Change [%) in Initial Constituents

Element	Initial Amount	FFTF 2101	FFTF 2909	HFIR PTP	HFIR RB4	HFIR RB4(HF)	First Wall STARFIRE	First Wall MARS
Fe	0.863	0.01	0.10	-2.05	0.77	0.17	-1.53	-1.79
Cr	0.0961	-3.0	-0.00	-1.46	-1.48	-0.60	1.16	1.18
Mn	0.0203	0.40	-4.4	-66.0	-45.0	-7.7	50.0	61.0
W	0.01305	-17.5	-29.2	-90.0	-59.0	-35.0	-36.0	-10.0
C	0.00457	-0.03	-0.00	-0.02	-0.00	-0.00	-1.33	-1.35

New Elements [parts per thousand)

Element	FFTF 2101	FFTF 2909	HFIR PTP	HFIR RB4	HFIR RB4(HF)	First Wall STARFIRE	First Wall MARS
H	0.78	*0.001*	0.66	0.147	0.155	12.0	12.1
He	0.070		0.069	0.016	0.013	2.08	2.09
Be	0.001		0.001			0.018	0.018
Ti	0.004		0.005	0.001	0.001	0.35	0.36
Co	0.028	0.012	25.4	2.31	0.051	0.026	0.005
Ni			8.4	0.342	0.003	0.002	
cu			0.127				
Zn			0.010				
Hf						0.003	0.005
Ta	0.005	0.007			0.006	0.022	0.287
Re	1.53	1.59		2.02	0.97	1.82	0.94
os	0.72	0.180	1.027	1.03	1.67	2.10	0.063
Ir		0.139	5.6	2.41	1.45	0.58	
Pt		0.017	0.68	0.97	0.39	0.134	
Au				0.055	0.003		
Hg			2.87	0.95	0.001		
Tl			3.2	0.030			
Pb			0.52				

TABLE 6

TRANSMUTATIONS IN CuBe AFTER 5 YEARS IN 7 FUSION TEST FACILITIES

Fractional Change (%) in Initial Constituents

Element	Initial Amount	FFTF 2101	FFTF 2909	HFIR PTP	HFIR RB4	HFIR RB4(HF)	First Wall STARFIRE	First Wall MARS
cu	0.874	-4.4	-1.38	-43.0	-23.6	-4.2	-5.9	-4.1
Be	0.126	-2.26	-0.01	-2.66	-0.48	-0.46	-3.8	-3.9

New Elements (parts per thousand)

Element	FFTF 2101	FFTF 2909	HFIR PTP	HFIR RB4	HFIR RB4(HF)	First Wall STARFIRE	First Wall MARS
H	2.96	0.007	302.(?)	1.34	0.49	13.4	10.2
He	3.40	0.008		0.49	0.77	8.5	8.5
Li	0.46	0.003			0.011	0.197	0.47
Fe						0.019	0.021
co	0.077		0.216	0.010	0.015	1.97	2.05
Ni	25.7	8.9	219.0	151.0	28.3	44.0	32.0
Zn	9.06	3.2	148.0	56.0	8.6	5.4	1.70
Ga			5.3	0.197			
Ge			2.92	0.033			

TABLE 7

TRANSMUTATIONS IN SIALON AFTER 5 YEARS IN 7 FUSION TEST FACILITIES

Fractional Change (%) in Initial Constituents

Element	Initial Amount	FFTF 2101	FFTF 2909	HFIR PTP	HFIR RB4	HFIR RB4(HF)	First Wall STARFIRE	First Wall MARS
N	0.357	-2.66	-0.17	-50.0	-20.0	-32.0	-2.96	-2.78
O	0.214	-0.13	-0.00	-0.16	-0.03	-0.03	-1.33	-1.32
Al	0.214	-0.28	-0.04	-8.4	-2.81	-0.39	-0.46	-0.39
Si	0.214	0.24	0.04	8.2	2.76	0.38	-1.24	-1.31

New Elements (parts per thousand)

Element	FFTF 2101	FFTF 2904	HFIR PTP	HFIR RB4	HFIR RB4(HF)	First Wall STARFIRE	First Wall MARS
H	5.2	0.60	180.0	71.0	10.7	14.1	13.1
He	5.0	0.015	1.86	0.95	1.01	9.5	9.8 .
Li	0.001		0.001			0.56	0.53
Be						0.024	0.026
8	4.7	0.015	3.8	0.89	0.94	3.3	3.6
C	5.1	0.60	175.0	71.0	10.7	9.5	8.6
Ne						0.004	0.005
Na						0.024	0.024
Mg	0.055		0.049	0.010	0.010	3.6	3.6
P	0.016	0.003	0.268	0.089	0.013	0.006	0.003
S			0.009	0.001			

TABLE 8

TRANSMUTATIONS IN Be AFTER 5 YEARS IN 7 FUSION TEST FACILITIES

Fractional Change (%) in Initial Constituents

Element	Initial Amount	FFTF 2101	FFTF 2909	HFIR PTP	HFIR R84	HFIR RB4(HF)	First Wall STARFIRE	First Wall MARS
Be	1,000	-2.26	-0.01	-2.66	-0.48	-0.46	-3.8	-3.9

New Elements (parts per thousand)

Element	FFTF 2101	FFTF 2909	HFIR PTP	HFIR RB4	HFIR RB4(HF)	First Wall STARFIRE	First Wall MARS
H	not calculated separately						
He	not calculated separately						
Li	*3.1*	0.024			0.087	1.56	*3.1*

TABLE 9

TRANSMUTATION IN C AFTER 5 YEARS IN 7 FUSION TEST FACILITIES

Fractional Change (%) in Initial Constituents

Element	Initial Amount	FFTF 2101	FFTF 2909	HFIR PTP	HFIR RB4	HFIR RB4(HF)	First Wall STARFIRE	First Wall MARS
C	1.000	-0.03	-0.00	-0.02	-0.00	-0.00	-1.33	-1.35

TABLE 9 (Cont'd)

New Elements (parts per thousand)

Element	FFTF 2101	FFTF 2909	HFIR PTP	HFIR RB4	HFIR RB4(HF)	First Wall STARFIRE	First Wall MARS
H	not calculated separately						
He	not calculated separately						
Be	0.212		0.197	0.039	0.037	3.85	3.89

TABLE 10

TRANSMUTATIONS IN Al AFTER 5 YEARS IN 7 FUSION TEST FACILITIES

Fractional Change (%) in Initial Constituents

Element	Initial Amount	FFTF 2101	FFTF 2909	HFIR PTP	HFIR RB4	HFIR RB4(HF)	First Wall STARFIRE	First Wall MARS
Al	1.000	-0.29	-0.00	-8.4	-2.81	-0.39	-1.32	-1.26

New Elements (parts per thousand)

Element	FFTF 2101	FFTF 2909	HFIR PTP	HFIR RE4	HFIR RB4(HF)	First Wall STARFIRE	First Wall MARS
H	0.68	0.001	7.4	0.139	0.130	8.2	8.2
He	0.139		0.120	0.024	0.024	5.7	5.7
Ne						0.012	0.012
Na	0.001					0.099	0.100
Mg	0.171		0.137	0.029	0.028	11.8	11.9
Si	2.77	0.042	84.0	28.1	3.9	1.26	0.56

TABLE 11

TRANSMUTATIONS IN Si AFTER 5 YEARS IN 7 FUSION TEST FACILITIES

Fractional Change (%) in Initial Constituents

Element	Initial Amount	FFTF 2101	FFTF 2909	HFIR PTP	HFIR RB4	HFIR RB4(HF)	First Wall STARFIRE	First Wall MARS
Si	1.000	-0.02	-0.01	-0.14	-0.04	-0.01	-1.36	-1.37

New Elements (parts per thousand)

Element	FFTF 2101	FFTF 2909	HFIR PTP	HFIR RB4	HFIR RB4(HF)	First Wall STARFIRE	First Wall MARS
H	not calculated separately						
He	not calculated separately						
Na						0.011	0.012
Mg	0.095		0.092	0.017	0.016	5.0	5.0
Al	0.034		0.016	0.005	0.004	8.6	8.7
P	0.072	0.013	1.25	0.41	0.061	0.029	0.016
S			0.044	0.005			

TABLE 12

TRANSMUTATIONS IN Cu AFTER 5 YEARS IN 7 FUSION TEST FACILITIES

Fractional Change (%) in Initial Constituents

Element	Initial Amount	FFTF 2101	FFTF 2909	HFIR PTP	HFIR RB4	HFIR RB4(HF)	First Wall STARFIRE	First Wall MARS
cu	1.000	-4.0	-1.38	-43.0	-23.7	-4.2	-5.8	-4.1

New Elements (parts per thousand)

Element	FFTF 2101	FFTF 2909	HFIR PTP	HFIR RB4	HFIR RB4(HF)	First Wall STARFIRE	First Wall MARS
H	not separately calculated						
He	not separately calculatea						
Fe						0.022	0.024
co	0.088		0.247	0.011	0.017	2.25	2.35
Ni	29.4	10.2	251.0	173.0	32.0	50.0	37.0
Zn	10.3	3.6	169.0	64.0	9.8	6.2	2.04
Ga			6.1	0.225			
Ge			3.3	0.038			

TABLE 13

TRANSMUTATIONS IN Nb AFTER 5 YEARS IN 7 FUSION TEST FACILITIES

Fractional Change (%) in Initial Constituents

Element	Initial Amount	FFTF 2101	FFTF 2909	HFIR PTP	HFIR RB4	HFIR RB4(HF)	First Wall STARFIRE	First Wall MARS
Nb	1.000	-10.6	-4.0	-66.0	-30.0	-3.5	-9.2	-5.3

New Elements (parts per thousand)

Element	FFTF 2101	FFTF 2909	HFIR PTP	HFIR RB4	HFIR RB4(HF)	First Wall STARFIRE	First Wall MARS
H	0.109		0.236	0.022	0.005	5.5	5.5
He	0.034			0.005	0.005	1.15	1.22
Sr						0.001	0.013
Y	0.005		0.002	0.001	0.001	0.261	0.293
Zr	0.236		0.126	0.037	0.040	26.5	28.8
Mo	106.0	40.0	660.0	298.0	35.0	65.0	24.4
Tc	0.001		1.48	0.020			
Ru			0.151	0.001			
Rh			0.001				

TABLE 14

TRANSMUTATIONS IN Mo AFTER 5 YEARS IN 7 FUSION TEST FACILITIES

Fractional Change (%) in Initial Constituents

Element	Initial Amount	FFTF 2101	FFTF 2909	HFIR PTP	HFIR RB4	HFIR RB4(HF)	First Wall STARFIRE	First Wall MARS
Mo	1.000	-3.5	-0.93	-6.3	-2.54	-0.81	-2.44	-1.81

TABLE 14 (Cont'd)

New Elements (parts per thousand)

Element	FFTF 2101	FFTF 2909	HFIR PTP	HFIR RB4	HFIR RB4(HF)	First Wall STARFIRE	First Wall MARS
H	not calculated separately						
He	not calculated separately						
Sr						0.109	0.113
Y	0.001					0.31	0.32
Zr	0.029		0.020	0.004	0.005	1.71	1.62
Nb	0.039		0.038	0.010	0.009	4.3	5.0
Tc	22.5	6.72	38.0	17.2	6.3	14.0	9.3
Ru	11.7	2.56	24.6	8.0	1.81	4.0	1.78
Rh	0.109	0.003	1.22	0.162	0.003	0.009	0.001
Pd	0.009		0.046	0.019			

TABLE 15

TRANSMUTATIONS IN W AFTER 5 YEARS IN 7 FUSION TEST FACILITIES

Fractional Change (%) in Initial Constituents

Element	Initial Amount	FFTF 2101	FFTF 2909	HFIR PTP	HFIR RB4	HFIR RB4(HF)	First Wall STARFIRE	First Wall MARS
W	1.000	-17.2	-29.0	-90.0	-57.0	-34.0	-36.0	-10.0

New Elements (parts per thousand)

Element	FFTF 2101	FFTF 2909	HFIR PTP	HFIR RB4	HFIR RB4(HF)	First Wall STARFIRE	First Wall MARS
H	0.003		0.001			0.218	0.254
He	0.002					0.213	0.226
Hf	0.002					0.211	0.39
Ta	0.41	0.54	0.001	0.008	0.47	1.69	22.0
Re	117.0	155.0	360.0	155.0	74.0	140.0	72.0
os	55.0	122.0	66.0	80.0	128.0	161.0	5.2
Ir	0.080	10.8		185.0	111.0	44.0	
Pt	0.005	1.29	44.0	74.0	30.0	10.3	
Au				4.2	0.263	0.012	
Hg			185.0	72.0	0.086	0.007	
Tl			207.0	2.31			
Pb			34.0	0.058			

CHAPTER 3

REDUCED ACTIVATION MATERIALS

PHASE DEVELOPMENT AND SWELLING IN Fe-Mn AND Fe-Cr-Mn ALLOYS DURING NEUTRON IRRADIATION

F. A. Garner, D. S. Gelles, H. R. Brager, and J. M. McCarthy, (Hanford Engineering Development Laboratory)

1.0 Objective

Tie object of this effort is to determine those factors which control the swelling of alloy systems which have the potential for reduced long-term activation.

2.0 *Summary*

Whereas second phases do not form in Fe-Cr-Ni ternary alloys during neutron irradiation in the range 400-600°C, iron-rich ferrite precipitates form in simple Fe-Mn and Fe-Cr-Mn alloys at 520 and 600°C at 14 dpa. The cause of the large densification (2.2%) earlier observed in Fe-35Mn at 9 dpa and 420°C does not appear to be related to precipitation, however, and is thought to be the result of compositional segregation on a rather fine scale.

3.0 *Program*

Title: Irradiation Effects Analysis (AKJ)
Principal Investigator: D. G. Doran
Affiliation: Hanford Engineering Development Laboratory

4.0 Relevant OAFS Program Plan Task/Subtask

Subtask II.C.I Effects of Material Parameters on Microstructure

5.0 Accomplishments and Status

5.1 Introduction

In previous reports[1-3] it was shown that the swelling of simple Fe-Mn binary and Fe-Cr-Mn ternary alloys in FFTF-MOTA at 520 and 600°C at 14 dpa was remarkably insensitive to the chromium content and only weakly dependent on the manganese level, as shown in Figures 1 and 2. It was also shown that the swelling of these alloys at 420°C and 9 dpa was likewise rather insensitive to composition but that there was an increasing tendency to densify with increasing manganese content, approaching 2.2% densification at Fe-35Mn, as shown in Figure 2.

This densification was also thought to account for the slight dependence of density change on manganese content observed at 520 and 600°C at 16 dpa. In effect, the observed swelling as measured by density change was the sum of relatively composition-independent void swelling and composition-sensitive phase instabilities.

In the most recent report it was shown that there was some basis for assuming that there was a compositional dependence of precipitation at 520°C.[3] In Fe-10Cr-XMn alloys, there was an increase found in the formation of large precipitates (unidentified at that time) when the manganese level fell from 30 to 20%.

There was also a concomitant increase in swelling, however, showing that the increase in precipitation was somehow related to the onset of swelling and was not in itself the sole cause of the slight dependence of density change on composition.

In this report a number of the binary and ternary alloys have been examined using transmission election microscopy and x-ray analysis. In some cases the examination was only cursory and all specimens continue to be examined.

5.2 Examination of Fe-5Cr-15Mn Irradiated at 600°C to 14 dpa

As shown in Figure 3, there were two exceptions to the general trend established by the swelling data of all other alloys at 520 and 600°C. These exceptions both involved Fe-5Cr-15Mn. At both 520°C and 600°C the swelling was significantly below that expected from the trends observed at higher chromium levels. The 520°C specimen has not yet been examined but the 600°C specimen has been examined. AS shown in Figures 4a-4b the matrix has decomposed into large elongated ferrite precipitates, on the order of 2-10 microns in size) and a matrix of retained austenite. The relative volume of the two phases is difficult to determine because the austenite is easily attacked and destroyed in the polishing. leaving the ferrite particles protruding far from the surfaces and edge of the foil.

An even more interesting observation is that voids were found but they appeared to be coated with a shell that also resisted electropolishing. Note in Figure 4b that some coated voids are also suspended from precipitates hanging over the edge of the foil. At this point it is assumed that the void shells are ferritic in nature, but this assumption has not yet been tested.

5.3 Examination of Specimens Irradiated at 520°C to 14 dpa

To date we have examined Fe-35Mn, Fe-10Cr-30Mn, Fe-15Cr-20Mn and Fe-10Cr-20Mn.

5.3.1 Examination of Fe-35Mn

As shown in Figure 5. once again we observe a decomposition into ferrite precipitates which resist electropolishing and the more easily removed retained austenite. The precipitates range from 0.2 to 1.5 μm in size. In this case the precipitates were analyzed by EDX and found to be essentially pure iron. Once again the voids appear to be coated and resistant to electropolishing. Within any one grain the swelling and phase decomposition appeared to be rather uniform, but adjacent grains often exhibited quite different levels of evolution. In some grains in which the precipitation was low, void swelling was present but at obviously lower levels.

5.3.2 Examination of Fe-10Cr-30Mn

This specimen as originally polished possessed a poorly polished surface and insufficient thin area. It was later flash-polished, yielding a thinner region for examination but also causing the ferrite precipitates to preferentially etch instead of the austenite matrix, as shown in Figure 6. Once again it was obvious that substantial ferrite formation had occurred. Since the ferrite particles did not protrude from the foil edge and could not be easily analyzed for their composition. a broad beam scan of a large area was performed. A drop in the overall iron level from 70 to 65% was observed, confirming that the lost ferrite precipitates were again rich in iron.

5.3.3 Examination of Fe-10Cr-20Mn

As shown in Figure 7 there is substantially less ferrite in this specimen, indicating that decreasing the manganese from 30 to 20% at 10% chromium affects the rate of formation of ferrite. The local swelling levels are in general larger than that of the Fe-10Cr-30Mn alloy. The dislocation evolution is easier to study in the absence of precipitation and appears to be typical of that observed in Fe-Cr-Mn alloys. The relative orientation of the ferrite precipitates were analyzed with respect to the matrix. They were found to exhibit the well-known Kurdjimov-Sachs relationship where $(111)_\gamma \parallel (011)_\alpha$ and $[\bar{1}01]_\gamma \parallel [\bar{1}\bar{1}1]_\alpha$.

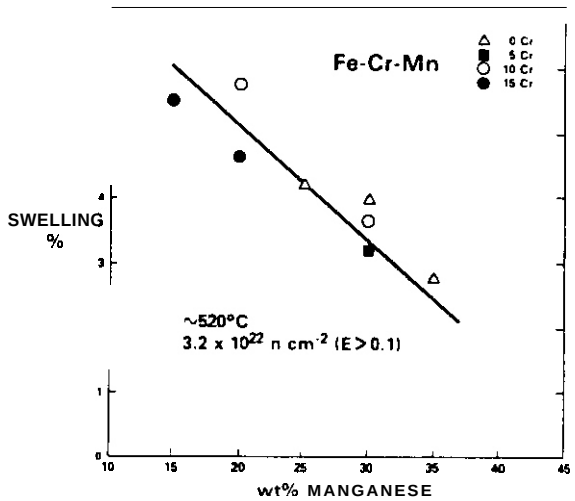

figure 1. Neutron-induced swelling of Fe-Mn and Fe-Cr-Mn alloys in FFTF at 520°C and 14 dpa as determined by immersion density measurements.(1-3)

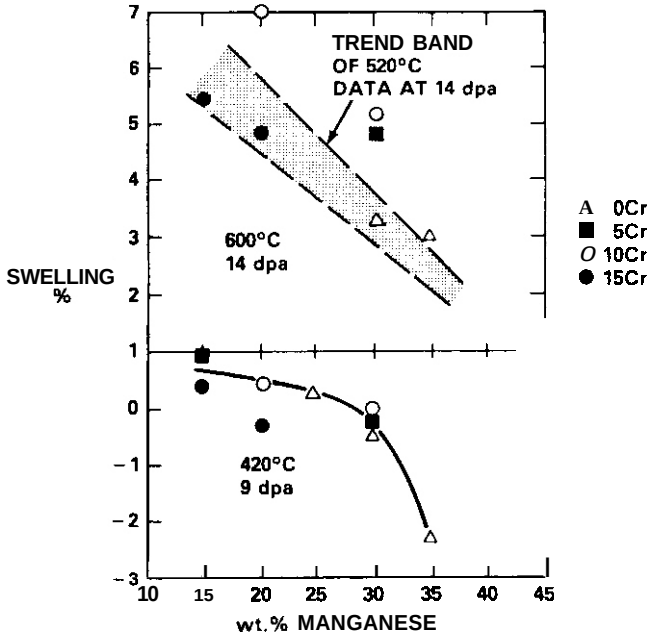

Figure 2. Neutron-induced density changes of Fe-Mn and fe-Cr-Mn alloys at (14 dpa, 600°C) and (9 dpa, 420°C).(3)

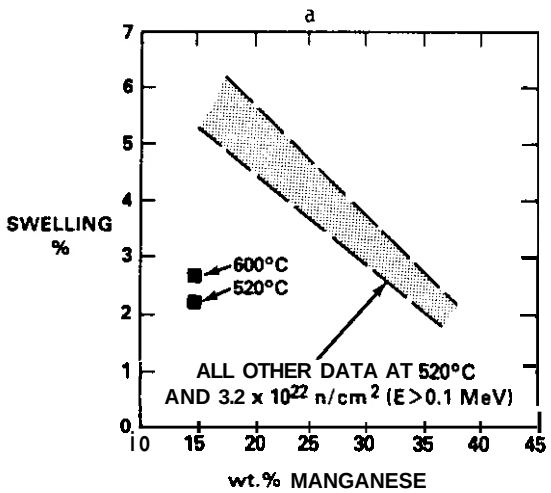

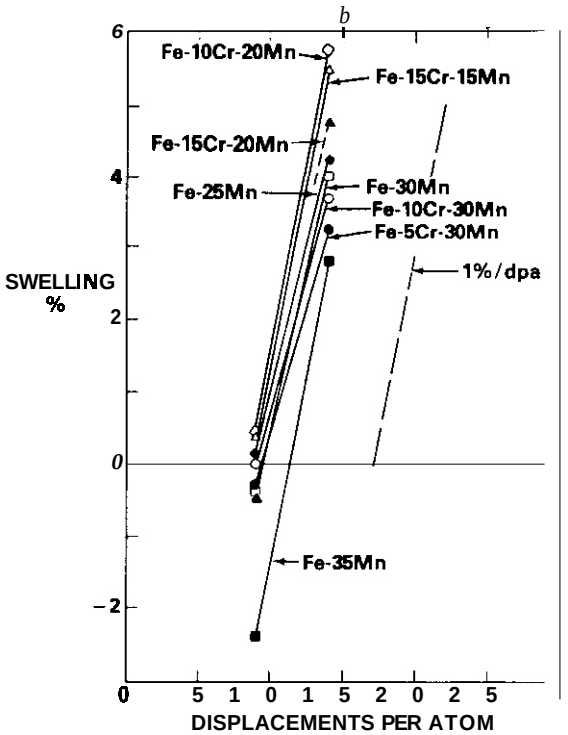

Figure 3. (a) Comparison of swelling of Fe-5Cr-15Mn at 14 dpa with the trend of other Fe-Cr-Mn alloys at 520°C and 14 dpa. (b) Plot of 420 and 520°C data ignoring temperature, with the exception of Fe-5Cr-15Mn at 520°C.

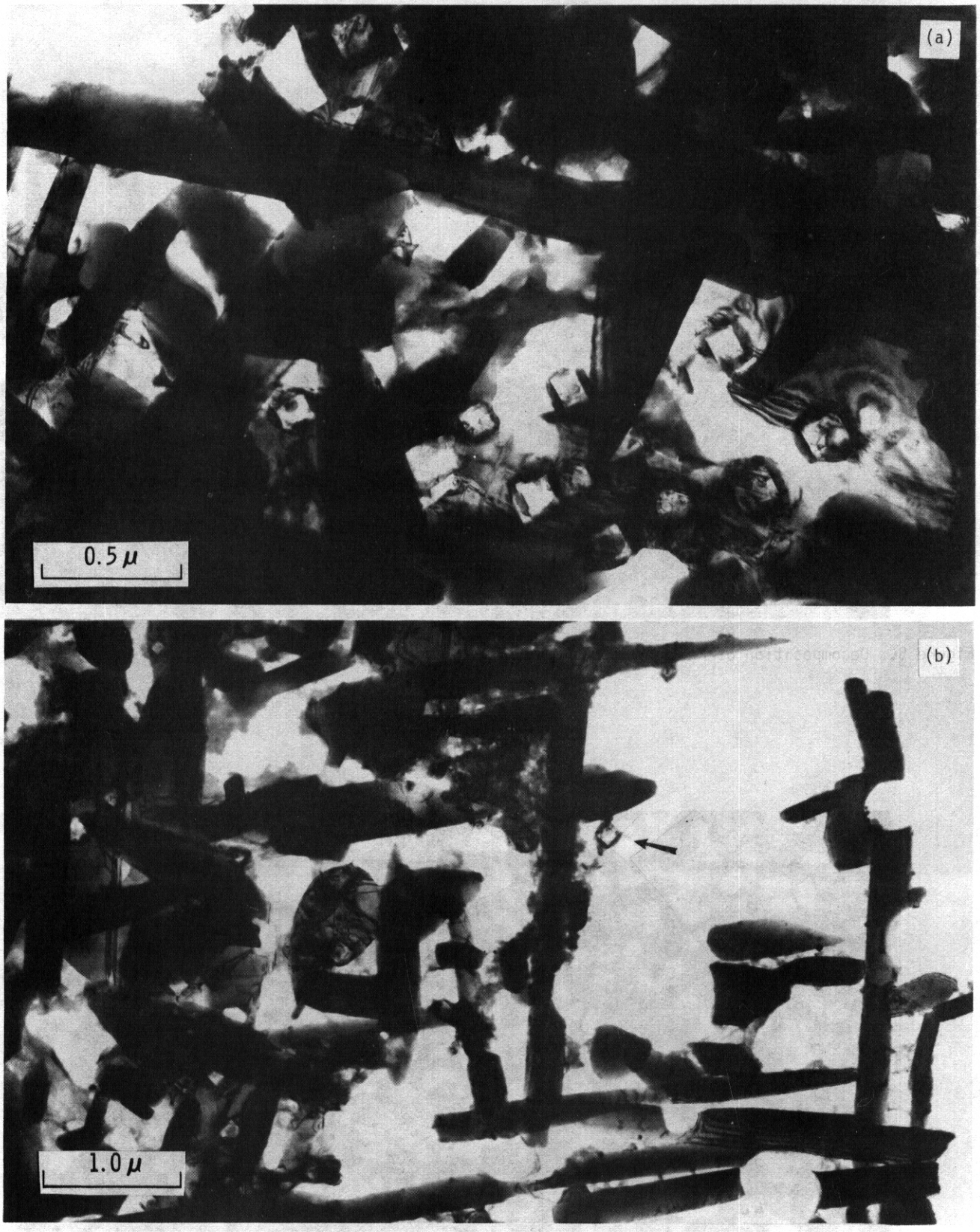

Figure 4. Micrographs showing formation of large iron-rich ferrite precipitates protuding from the strongly etched austenite matrix in Fe-5Cr-15Mn at 600°C and 14 dpa. Voids are also coated with ferrite and resist electropolishing. The arrow in (b) points to an almost unsupported void which has resisted electropolishing.

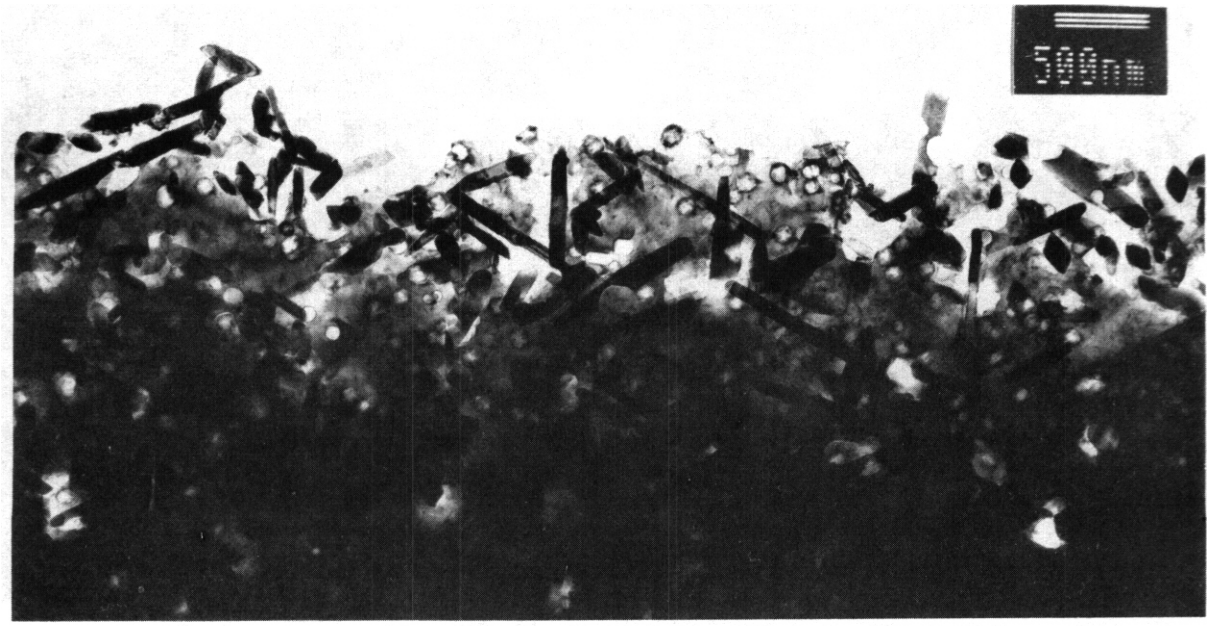

Figure 5. Decomposition of Fe-35Mn at 520°C and 14 dpa.

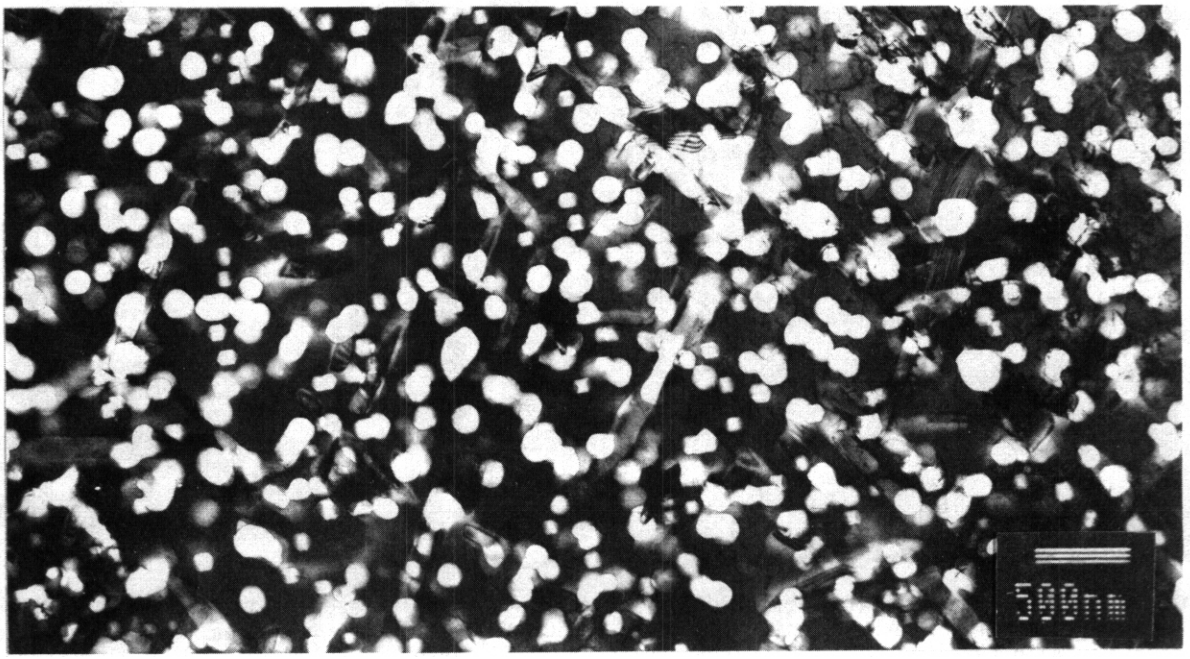

Figure 6. Preferential attack of ferrite particles during flash-polishing of Fe-10Cr-30Mn (520°C, 14 dpa).

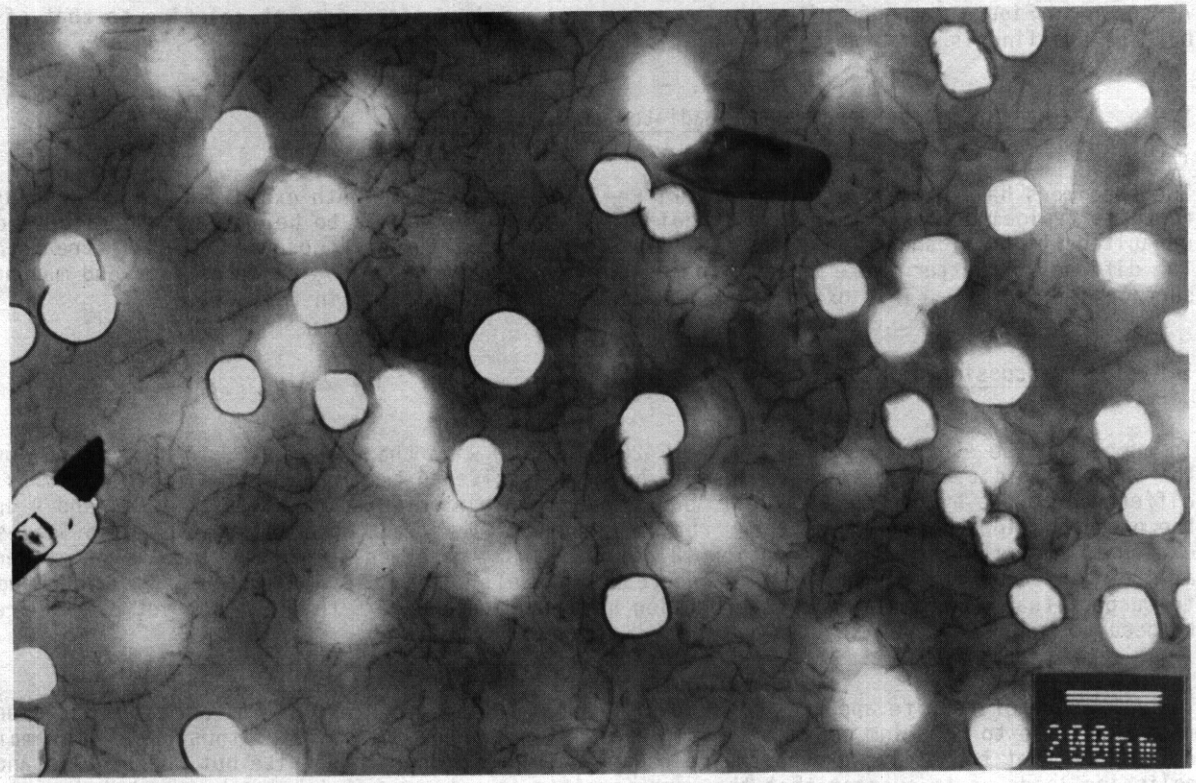

Figure 7. Micrograph of Fe-10Cr-20Mn after irradiation at 520°C to 14 dpa.

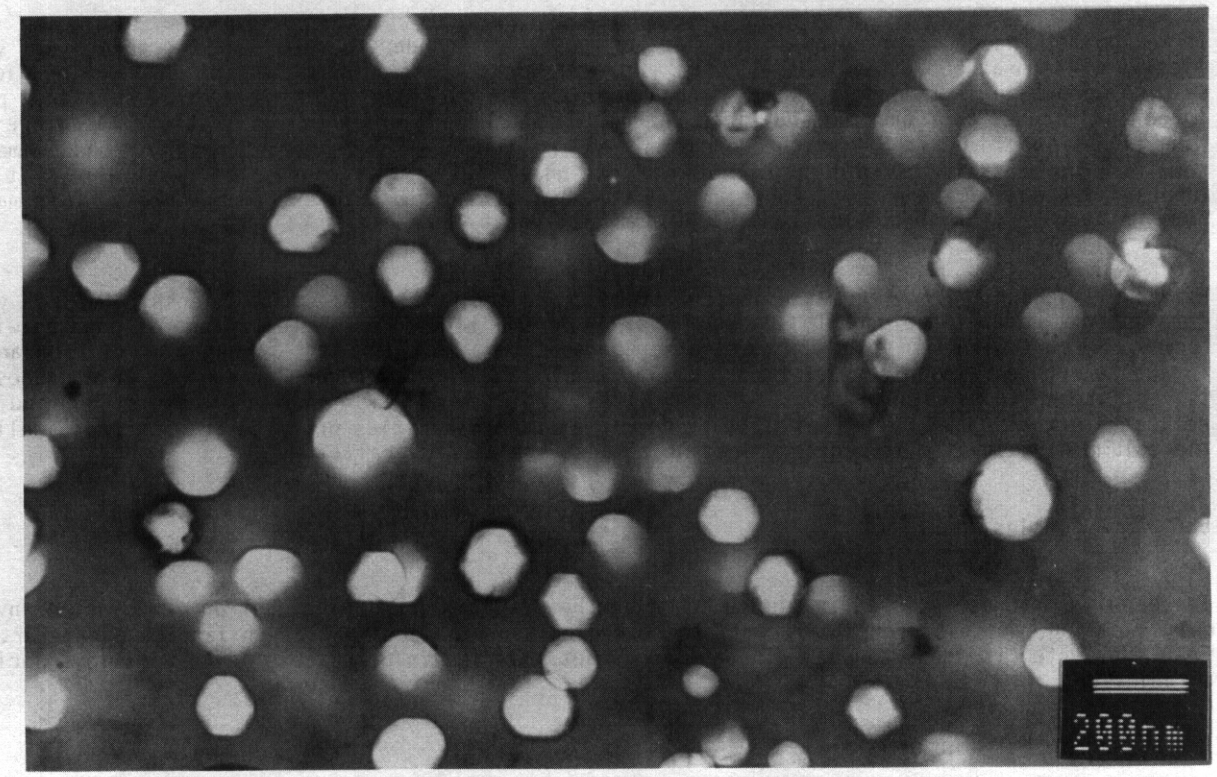

Figure 8. Micrograph of Fe-15Cr-20Mn after irradiation at 520°C to 14 dpa.

5.3.4 Examination of Fe-15Cr-20Mn

As shown in Figure 8 the ferrite density seems to have decreased somewhat relative to that of Fe-10Cr-20Mn but the swelling is comparable. The precipitates were found to average 75-80% iron.

5.4 Examination of Specimens Irradiated at 420°C and 9 dpa

Two specimens have been examined thus far, Fe-35Mn and Fe-30Mn. Both exhibited a high density of contrast features typical of low temperature irradiation. These were found to be small dislocation loops. largely unfaulted. (<500 A) and small voids (<100 A). No precipitates were observed. Small streaks observed in the diffraction pattern were found to be associated with an oxide-hydroxide of iron and manganese on the surface of the foil. This oxidation reflects the lack of chromium in these alloys.

5.5 Discussion of Results

In comparing the evolution of Fe-35Mn at (420°C, 9 dpa) with that at (520°C, 14 dpa) it is obvious that the phase stability at this composition is quite sensitive to temperature. We could possibly ascribe the difference to the higher dose as well, but there is no hint of precipitation at 420°C and 9 dpa. Otherwise the precipitation response must occur rather abruptly. This lack of precipitation also leaves us with no explanation of the large densification (2.2%) previously observed at 420°C. The amount of densification at 420°C is comparable to the relative decrease in swelling of this alloy at 520°C, which leads us in turn to suspect that substantial microsegregation has occurred at 420°C that has not yet caused precipitation to occur.

The formation of ferrite appears to be sensitive to manganese content at 10% chromium but appears to be most sensitive to chromium content at all levels of manganese investigated thus far. It remains to be determined that the shells around the voids are actually iron-rich ferrite but their resistance to electropolishing leads us to suspect that they are ferritic in nature. It is also known that iron is the slowest diffusing species compared to manganese and chromium in both the iron-based fcc and bcc crystal structures. Based on the observed behavior in the Fe-Cr-Ni system the slowest diffusing species is expected to segregate at the void surface via the Inverse-Kirkendall mechanism.

If we look at the equilibrium phase diagram for Fe-Mn the boundary between the two phase ($\alpha + \gamma$) region lies at ~14% Mn at 600°C, ~18% Mn at 520°C and ~23% Mn at 420°C. The α ferrite phase is predicted to contain no more than 3% manganese, which is consistent with the finding of essentially pure iron precipitates in Fe-35Mn at 520°C. Chromium additions change the phase boundaries only a little. Therefore all but the 15Mn alloys should be stable at the conditions of irradiation, unless the inverse-Kirkendall mechanism or some other process is operating. Even though the phase boundary is closest for most alloys at 420°C, the Inverse Kirkendall mechanism is known to operate most strongly at higher temperatures. This may account for the lack of ferrite observed in the 30-35Mn alloys at 420°C.

Void swelling and ferrite formation appear to be connected but the exact relationship has not yet been determined. Part of the density change may arise from a lattice parameter change associated with ferrite formation, part with the voidage, and another part associated with micro-segregation of iron and manganese in the fcc phase. In an earlier report it was shown that the dependence of density on manganese content is very strong in the fcc phase. The inconsistent swelling behavior of Fe-5Cr-15Mn at 500 and 600°C may reflect a situation where the precipitate formed at such quantities prior to the onset of swelling that the volume of austenite is reduced, leading to less swelling overall.

5.6 Conclusions

The density changes observed in simple Fe-Mn and Fe-Mn-Cr alloys during neutron irradiation involve not only swelling, but also ferrite formation and segregation-induced changes in lattice parameter. The Fe-Cr-Mn system is prone to phase instabilities not observed in comparable Fe-Cr-Ni alloys during neutron irradiation.

6.0 References

1. H. R. Brager and F. A. Garner, "Swelling of Fe-Cr-Nn Ternary Alloys in FFTF," DAFS Quarterly Progress Report, DOE/ER-0046/19, November 1984, pp. 31-33.

2. F. A. Garner and H. R. Brager, "Neutron-Induced Swelling of Fe-Cr-Mn Ternary Alloys," OAFS quarterly Progress Report, DOE/ER-0046/21, May 1985, pp. 41-45.

3. F. A. Garner and H. R. Brager, "Neutron-Induced Swelling and Microstructural Development of Simple Fe-Mn and Fe-Cr-Mn Alloys in FFTF," OAFS Quarterly Progress Report, DOE/ER-0046/23, November 1985, pp, 18-23.

7.0 Future Work

Microcopy at the 9 and 16 dpa levels will continue. Density data at (35 dpa, 600°C), (45 dpa, 420°C) and (45 dpa, 500°C) will be obtained.

8.0 Publications

None

ACTIVATION CALCULATIONS USING AN EXPANDED NUCLEAR DATA EASE

F. M. Mann (Hanford Engineering Development Laboratory)

1.0 Objective

The objective of this work is to calculate with reasonable accuracy and completeness the activation that elements in fusion reactors will exoerience.

2.0 *Summary*

Using an expanded nuclear data base, the activation of nitrogen, aluminum, iron, nickel, copper, zirconium, niobium, molybdenum, tungsten, and lead were calculated for the first wall positions of the STARFIRE and MARS conceptual fusion reactors.

3.0 Program

Title: Irradiation Effects Analysis
Principal Investigator: D. G. Doran
Affiliation: Westinghouse Hanford Company

4.0 Relevant Program Plan TasklSubtask

No tasks on reduced activation were identified in the original DAFS Program Plan.

5.0 Accomplishments and Status

5.1 Introduction

The activation of elements at a fusion reactor first wall have been calculated at this and other laboratories. However, all these calculations are generally incomplete because their associated nuclear data libraries are incomplete, multi-step reactions may be excluded or treated only crudely, and high fluence effects may be inferred incorrectly from low fluence effects. A preliminary treatment of these effects was given in a previous progress report.(1)

Previous work(2) has demonstrated that the reactor design can also have a significant effect on the production of activated material. For example, STARFIRE with its large number of low energy neutrons tranmutes more quickly through (n,gamma) reactions than does the MARS design.

The approach in the present work is to expend the needed cross section and decay data libraries and then rerun the activation calculations to determine the effect of large exposures. Thus, different compositional limits may be found. Also, reactions which need more accurate cross sections and isotopes needing disposal limits can be determined.

This report addresses the effect of the new cross section library(3) on these questions. However, because of uncertainties in the cross sections of certain transnutation chains and in the limits which may be relevant in waste disposal, the quantitative results must be considered tentative.

5.2 Calculational Results and Discussions

The REAC computer code system[4] was used to calculate the activation of the various elements after a six-year exposure at the first wall position of STARFIRE (corresponding to 21.6 MW-Y/meter**2 wall loading) and of MARS (corresponding to 25.8 MW-Y/meter**2) followed by a 3000-day cooling period. Time steps for the six-year exposure were 0.25 years each.

Tables 1 through 15 display the decay rate of product isotopes for C, N, Al, Ti, V, Cr, Mn, Fe, Ni, Cu, Zr, Nb, Mo, W, and Pb.

The disposal limits shown in Tables 1-15 are for class C near surface burial disposal for metals. Following the example of the NRC, the disposal limits for metals are a factor of 10 higher than for general waste. Unless otherwise noted, the disposal limits are taken from 10 CFR 61.[5] Other limits are taken from the work of Kennedy.[6]

There exist some isotopes which are produced in the calculations, however, where limits have neither been established by the NRC or estimated. The most important are IR-192* and Pt193 which are produced when tungsten is irradiated. These isotopes may potentially limit the use of tungsten in reduced activation alloys for reactors which use water as a coolant such as STARFIRE. It should be noted that not only does the production of these isotopes require the addition of at least 6 neutrons and hence varies rapidly with the fluence but also that any of the (n,gamma) cross sections involved are only estimates and not true evaluations. For other cases where disposal limits do not exist, it is unlikely that previously found composition limits will be significantly changed.

Besides the case of tungsten which was mentioned above, the most significant difference from previous work is for lead. The new libraries allow the calculation of bismuth isotopes which lower the allowable amount of lead (by a factor of 2 for STARFIRE and by a factor of 10 for MARS). Other differences are less than a factor of 2 and involve the burnout of the limiting isotope.

5.3 Conclusions

Calculations with REAC using the expanded data libraries suggest that the disposal of tungsten and lead may be more of a concern. However, the reaction data and disposal limits for tungsten are highly uncertain so that the exact magnitude of the effect is unknown. Other elements show no significant change using the new libraries.

6.0 References

1. D. G. Doran and F. M. Mann, "Activation Calculations with an Expanded Cross-Section Library", DAFS quarterly Progress Report, August 1985, DOE/ER-046/22, (1985) 25.

2. H. L. Heinisch, F. M. Mann and D. G. Doran, "Spectral Dependence of Activation at Fusion Reactor First Walls", Fusion Technology,, 8 (1985) 2704.

3. F. M. Mann, "Cross Sections for Reduced Activation Studies", OAFS quarterly Progress Report, February 1985, DOE/ER-0046/20, (1985) 18.

4. F. M. Mann. "Transmutation of Alloys in MFE Facilities as Calculated by REAC (A Computer Code System for Activation and Transmutation", HEDL-TME 81-37, Westinghouse Hanford Company (1982).

5. Code of Federal Regulations, "Licensing Requirements for Land Disposal of Radioactive Waste", Title 10, Part 61.55 (cited as 10 CFR 61), Nuclear Regulatory Commission (December 20, 1982).

6. W. E. Kennedy, Jr., and F. M. Mann, "Potential Low-Level Waste Disposal Limits for Fusion Radionuclides", Trans. Am. Nucl. Soc., 45 (1983) 51.

7.0 Future Work

The near term effort will be concentrated on estimating waste disposal limits for the isotopes potentially limiting the use of tungsten and on determining the accuracy of the cross sections involved in the production of those isotopes. The longer term will see the estimation of other waste disposal limits, calculations for other materials (particularly isotopically tailored ones), and the beginning of the investigation of the possibilities of recycling.

8.0 Publications

H. L. Heinisch, F. M. Mann and D. G. Doran, "Spectral Dependence of Activation at Fusion Reactor First Walls", Fusion Technology, 8 (1985) 2704.

TABLE 1

ACTIVATION AFTER 6-YEAR RAOIATION, 3000-DAY COOLING
CARBON

Product	Disposal Limits (Curies/cm**3)	STARFIRE Oecay Rate (Curies/cm**3)	STARFIRE Ratio	MARS Oecay Rate (Curies/cm**3)	MARS Ratio
T	•	1.93e-2	*	7.92e-3	*
C 14	8.0e-3	5.91e-6	1350.	6.52e-6	1220.

TABLE 2

ACTIVATION AFTER 6-YEAR RADIATION, 3000-DAY COOLING
NITROGEN

Product	Disposal Limits (Curies/cm**3)	STARFIRE Oecay Rate (Curies/cm**3)	STARFIRE Ratio	MARS Decay Rate (Curies/cm**3)	MARS Ratio
T	*	1.77e+0	*	1.57e+0	•
C 14	8.0e-3	5.20e-2	0.15	4.12e-2	0.19

TABLE 3

ACTIVATION AFTER 6 YEAR RADIATION, 3000-DAY COOLING
ALUMIUM

Product	Oisposal Limits (Curies/cm**3)	STARFIRE Oecay Rate (Curies/cm**3)	STARFIRE Ratio	MARS Decay Rate (Curies/cm**3)	MARS Ratio
T	*	2.13e-2	*	1.97e-2	*
Na 22	*	1.01e-4	*	1.04e-4	*
Al 26	2.0e-5+	6.52e-5	0.31	6.57e-5	0.30

TABLE 4

ACTIVATION AFTER 6-YEAR RADIATION, 3000-DAY COOLING
TITANIUM

Product	Disposal Limits (Curies/cm**3)	STARFIRE Decay Rate (Curies/cm**3)	STARFIRE Ratio	MARS Decay Rate (Curies/cm**3)	MARS Ratio
T	*	3.34e-1	*	2.92e-1	*
Ar 39	?	4.39e-5	?	4.50e-5	?
Ar 42	?	1.13e-4	?	1.16e-4	?
Ca 45	*	2.14e-5	•	2.22e-5	*

* NRC limts are established by heating and personnel shielding requirements at time of disposal.
+ Disposal limits estimated by Kennedy (reference 6).
? No limits have been established by the NRC or estimated by Kennedy.

TABLE 5

ACTIVATION AFTER 6-YEAR RADIATION, 3000-DAY COOLING
VANADIUM

Product	Disposal Limits (Curies/cm**3)	STARFIRE Decay Rate (Curies/cm**3)	STARFIRE Ratio	MARS Decay Rate (Curies/cm**3)	MARS Ratio
T	*	1.53e-1	*	1.46e-1	*
V 49	*	1.11e-2	*	1.37e-2	•

TABLE 6

ACTIVATION AFTER 6-YEAR RADIATION, 3000-DAY COOLING
CHROMIUM

Product	Disposal Limits (Curies/cm**3)	STARFIRE Decay Rate (Curies/cm**3)	STARFIRE Ratio	MARS Decay Rate (Curies/cm**3)	MARS Ratio
T	•	8.72e-1	*	7.36e-1	*
V 49	*	1.51e-2	*	1.63e-2	*
Mn 54	•	1.79e-5	•	5.35e-6	*
Fe 55	*	2.68e-5	*		

TABLE 7

ACTIVATION AFTER 6-YEAR RAOIATION, 3000-DAY COOLING
MANGANESE

Product	Disposal Limits (Curies/cm**3)	STARFIRE Decay Rate (Curies/cm**3)	STARFIRE Ratio	MARS Decay Rate (Curies/cm**3)	MARS Ratio
T	*	5.34e-2	*	4.97e-2	*
Mn 53	6.0e-4+	2.31e-6	260.0	2.83e-6	210.0
Mn 54	*	4.65e-1	*	5.29e-1	*
Fe 55	*	1.78e+0	•	8.07e-2	*
Co 60	*	7.29e-6	*		

TABLE 8

ACTIVATION AFTER 6-YEAR RADIATION, 3000-DAY COOLING
IRON

Product	Disposal Limits (Curies/cm**3)	STARFIRE Decay Rate (Curies/cm**3)	STARFIRE Ratio	MARS Decay Rate (Curies/cm**3)	MARS Ratio
T	*	1.46e-1	*	9.82e-2	•
Mn 53	6.0e-4+	2.61e-5	23.0	3.12e-5	19.0
Mn 54	*	3.53e-2	*	2.86e-2	*
Fe 55	•	2.45e+1	*	2.36e+1	*
Co 60	•	3.27e-2	•	8.83e-5	*

* NRC limits are established by heating and personnel shielding requirements at time of disposal.
+ Disposal limits estimated by Kennedy (reference *6).*

TABLE 9

ACTIVATION AFTER 6-YEAR RADIATION, 3000-DAY COOLING
NICKEL

Product	Disposal Limits (Curies/cm**3)	STARFIRE Decay Rate (Curies/cm**3)	STARFIRE Ratio	MARS Decay Rate (Curies/cm**3)	MARS Ratio
T	•	6.94e-1	*	6.21e-1	*
Mn 54	*	2.18e-3	*	2.32e-3	*
Fe 55	•	8.27e+0	•	8.40e+0	•
Fe 60	?	1.69e-6	?	1.37e-6	?
co 57	*	1.17e-1	*	1.47e-1	*
Co 60	•	8.09e+0	•	6.73e+0	*
Ni 59	2.2e-4	9.26e-3	0.024	5.32e-3	0.041
Ni 63	7.0e-3	1.58e+0	0.0044	3.30e-1	0.021

TABLE 10

ACTIVATION AFTER 6-YEAR RADIATION, 3000-DAY COOLING
COPPER

Product	Disposal Limits (Curies/cm**3)	STARFIRE Decay Rate (Curies/cm**3)	STARFIRE Ratio	MARS Decay Rate (Curies/cm**3)	MARS Ratio
T	•	?	*	?	*
Fe 55	*	1.04e-5	*	1.09e-5	*
Fe 60	?		*	1.22e-6	?
Co 60	*	7.15e+0		7.04e+0	*
Ni 59	2.2e-4			3.55e-6	62.0
Ni 63	7.0e-3	1.74e+0	0.0040	1.30e+0	0.0054
Zn 65	*	4.26e-4	*	1.39e-4	•

TABLE 11

ACTIVATION AFTER 6-YEAR RADIATION. 3000-DAY COOLING
ZIRCONIUM

Product	Disposal Limits (Curies/cm**3)	STARFIRE Decay Rate (Curies/cm**3)	STARFIRE Ratio	MARS Decay Rate (Curies/cm**3)	MARS Ratio
T	•	2.16e-1	*	1.94e-1	*
Kr 85	?	6.72e-5	?	6.65e-5	?
Sr 90	7.0e-2	1.10e-2	6.4	9.59e-3	7.3
Zr 93	2.2e-3+	1.25e-4	18.0	1.33e-4	17.0
Nb 93*	?	5.01e-4	?	5.35e-4	?
Mo 93	3.0e-5+	2.53e-6	12.0	2.62e-6	11.5
Nb 94	2.0e-7	1.86e-6	0.11	2.94e-6	0.068

* NRC limits are established by heating and personnel shielding requirements at time of disposal
\+ Disposal limits estimated by Kennedy (reference 6).
? No limits have been established by the NRC or estimated by Kennedy.

TABLE 12

ACTIVATION AFTER 6-YEAR RADIATION, 3000-DAY COOLING
NIOBIUM

Product	Disposal Limits (Curies/cm**3)	STARFIRE Decay Rate (Curies/cm**3)	STARFIRE Ratio	MARS Decay Rate (Curies/cm**3)	MARS Ratio
T	*	1.37e+0	*	1.27e+0	*
Sr 90	7.0e-2	9.35e-4	75.0	7.50e-4	93.0
Zr 93	2.2e-3+	4.00e-5	55.0	4.50e-5	49.0
Nb 91	?	3.50e-2	?	7.2 9e-2	?
Nb 92	3.0e-4+	9.67e-6	11.0	2.72e-5	11.0
Nb 93*	?	4.09e+1	?	3.64e+1	?
Nb 94	2.0e-7	1.14e-1	0.000002	1.11e-1	0.0000018
Mo 93	3.0e-5+	1.39e-4	0.22	6.23e-6	4.8

TABLE 13

ACTIVATION AFTER 6-YEAR RADIATION, 3000-DAY COOLING
CARBON

Product	Disposal Limits (Curies/cm**3)	STARFIRE Decay Rate (Curies/cm**3)	STARFIRE Ratio	MARS Decay Rate (Curies/cm**3)	MARS Ratio
T	*	4.30e-1	*	4.14e-1	*
Kr 85	?	1.42e-5	?	1.46e-5	?
Sr 90	7.0e-2	1.66e-4	420.0	1.17e-4	420.0
Zr 93	2.2e-3+	4.76e-6	460.0	4.69e-6	470.0
Nb 91	?	1.88e-1	?	2.13e-1	?
Nb 93*	?	7.25e-1	?	2.99e-1	?
Nb 94	2.0e-7	7.11e-4	0.00028	1.66e-3	0.00012
Mo 93	3.0e-5+	1.11e-1	0.00027	6.09e-2	0.00049
Tc 98	?	4.36e-6	?	2.97e-6	?
Tc 99	3.0e-5	2.90e-3	0.010	1.93e-3	0.016
Rh 102	*	2.84e-4	•	1.51e-5	*

TABLE 14

ACTIVATION AFTER 6-YEAR RADIATION, 3000-DAY COOLING
TUNGSTEN

Product	Disposal Limits (Curies/cm**3)	STARFIRE Decay Rate (Curies/cm**3)	STARFIRE Ratio	MARS Decay Rate (Curies/cm**3)	MARS Ratio
T	*	1.62e-2	*	1.46e-2	*
Hf 178*	?	9.12e-3	?	4.94e-2	?
Ta 179	*	1.48e-2	*	9.48e-2	*
Re 184*	*	5.64e-6	*	3.07e-5	•
Re 186*	?	1.40e-2	?	1.35e-3	?
Ir 192'	?	4.28e+0	?		
Pt 193	?	5.41e+0	?		

• NRC limits are established by heating and personnel shielding requirements at time of disposal.
+ Disposal limits estimated by Kennedy [reference 6).
? No limits have been established by the NRC or estimated by Kennedy.

TABLE 15

ACTIVATION AFTER 6-YEAR RADIATION, 3000-DAY COOLING
LEAD

Product	Disposal Limits (Curies/cm**3)	STARFIRE Decay Rate (Curies/cm**3)	STARFIRE Ratio	MARS Decay Rate (Curies/cm**3)	MARS Ratio
T	*	2.13e-3	*	2.17e-3	*
Tl 204	*	1.59e+0	*	1.59e-1	*
Pb 205	5.0e-6+	2.95e-5	0.17	2.96e-5	0.17
Bi 207	1.13e-5	4.99e-5	0.23	8.39e-4	0.013
Bi 208	1.13e-5			2.46e-6	4.6
Bi 210*	1.13e-5	1.42e-6	8.0		

• NRC limits are established by heating and personnel shielding requirements at time of disposal.
+ Disposal limits estimated by Kennedy (reference 6).

CHAPTER 4

RADIATION EFFECTS MECHANISMS AND CORRELATIONS

OWR/RTNS-II LOW EXPOSURE SPECTRAL EFFECTS EXPERIMENT

H. L. Heinisch and J. S. Pintler (Hanford Engineering Development Laboratory)

1.0 Objective

The objective of this experiment is to determine the effect of the neutron spectrum on radiation-induced changes in mechanical properties for metals irradiated with fusion and fission neutrons.

2.0 *Summary*

The status of the OWR/RTNS-II Low Exposure Spectral Effects Experiment is reviewed. The primary RTNS-II irradiations and six of the eight Omega West reactor (OWR) irradiations have been completed. Tensile tests on specimens from the first elevated temperature RTNS-II irradiation have been completed. Tests have begun on specimens irradiated in OWR. Yield stress and ultimate tensile strength as a function of 14 MeV neutron fluence are reported here for pure iron and A302B pressure vessel steel. Both exhibit a definite temperature dependence in their response to 14 MeV neutron irradiation. The first tensile data from OWR are compared to RTNS-II data at 90°C. When compared on the basis of dpa, the data for solution annealed 316 stainless steel correlate and those for copper do not.

3.0 Program

Title: Irradiation Effects Analysis
Principal Investigator: D. G. Ooran
Affiliation: Westinghouse Hanford Company

4.0 Relevant OAFS Program Plan TasklSubtask

Subtask II.B.3.2	Experimental Characterization of Primary Damage State; Studies of Metals
Subtask II.C.6.3	Effects of Damage Rate and Cascade Structure on Microstructure; Low-EnergylHigh Energy Neutron Correlations
Subtask II.C.16.1	14-MeV Neutron Damage Correlation

5.0 Accomplishments and Status

5.1 Irradiations

The OWR/RTNS-II Spectral Effects Experiment (HEDL-SEX) originally called for three RTNS-II irradiations and eight OWR irradiations. The first two RTNS-II irradiations, R-1 and R-2, have been completed to peak fluences of 2.4 x 10^{18} n/cm^2 and 8.8 x 10^{18} n/cm^2 respectively in the HEOL dual-temperature furnace at temperatures of 90°C and 290°C. The third, short-term RTNS-II irradiation has been eliminated. As an adjunct to the fusion neutron portion of the experiment, some HEDL-SEX tensile specimens have been included in the ongoing joint Japan/U.S. long-term irradiation using the Japanese dual-temperature furnace at temperatures of 200°C and 450°C. Other specimens were irradiated at room temperature in an earlier Japanese-sponsored irradiation. The four OWR irradiations at 90°C have been completed, 0-1 to a total neutron fluence of 5.42 x 10^{19} n/cm^2, 0-2 to 1.44 x 10^{19}, 9-3 to 5.18 x 10^{18}, and 9-4 to an estimated 1.3 x 10^{20} n/cm^2. The two shorter irradiations at 290°C, 0-6 and 0-7, have also been completed to doses comparable to 0-2 and 0-3, respectively. Irradiation 0-5 is in progress, and 0-8 will follow immediately. Dosimetry for the OWR irradiations is being analyzed by L. R. Greenwood of Argonne National Laboratory.

5.2 Tensile Testing

The primary tensile testing of the R-1 specimens has been completed. Tests were done on 150 specimens covering 10 combinations of temperature and material. The materials are annealed iron, annealed copper, annealed 316 stainless steel, 20% cold worked 316 stainless steel, and A3028 pressure vessel steel. Specimens with fluences ranging from 6 x 10^{16} to 2 x 10^{18} n/cm^2 were tested for each material.

The results for copper and solution annealed 316 stainless steel were reported in an earlier progress report.[1] In both materials the change in yield strength as a function of 14 MeV neutron fluence exhibited temperature dependence in the range from room temperature to 290°C.

The chanae in yield strenath of annealed Marz arade iron as a function of 14 MeV neutron fluence in R-1 is plotted in Figure 1. There is a large scatter in the data for iron at both 90°C and 290°C. One might conclude that the change in yield strength is nearly independent of fluence, but at a different vaiue for each temperature. -However, there appears to be a slight tendency toward larger changes in yield strength with increasing fluence. Generally the largest source of error in miniature tensile tests is uncertainty in the specimen dimensions (which are used to compute the stresses). In the case of iron, the specimens were remarkably uniform, so uncertainty in the dimensions should be small. The most likely source of scatter in the iron data is contamination of the specimens by impurities, probably oxygen and nitrogen, which may have occurred when the vacuum in the furnace failed early on in the irradiation. The loadldisplacement curves for iron show a variety of yield point phenomena, from distinct upper and lower yield points to none at all, but having no apparent correlation with neutron dose. Tests on iron specimens irradiated in R-2, which has a fluence range overlapping that of R-1, should provide reliable results.

The change in yield strength of A302B pressure vessel steel as a function of 14 MeV neutron fluence is plotted in Figure 2. There is less scatter in the A3028 data than in iron. However, the uncertainty in specimen dimensions may very likely contribute to this scatter, since the A3028 specimens were considerably less uniform in thickness than usual miniature tensile specimens. There is a definite temperature dependence of change in yield stress with 14 MeV neutron fluence. The curves, fitted to the data points at each temperature, are functions of the form

$$\Delta\sigma_y = A + B\sqrt{\Phi t}$$

where $\Delta\sigma_y$ is the change in yield strength, Φt is the fluence, and A and 8 are constants. Dependence of the yield stress change on the square root of the fluence is what one might expect if a loop production strengthening mechanism is in effect. The addition of data from R-2 at higher fluences will provide a better data base from which to investigate strengthening mechanisms.

The ultimate tensile strengths of iron and A302B pressure vessel steel at both 90°C and 290°C are plotted as a function of fluence in Figure 3. There is little effect of 14 MeV neutron irradiation or temperature on tensile strength in this range of temperatures and fluences.

Specimens from R-2, 0-1, 0-2 and 0-3 are now being tested. The specimens in R-2 will provide data at higher fluences of 14 MeV neutrons than ever achieved before. There are also specimens in R-2 that have been irradiated in the same dose range as R-1, but at a slower rate. Comparisons of R-1 and R-2 data will address possible rate effects.

The first data from OWR irradiations is presented in Figures 4 and 5, for annealed 316 stainless steel and annealed copper, respectively. The change in yield strength is plotted as a function of displacement per atom (dpa) for specimens irradiated in 0-1, 0-2, and 0-3 and compared with those from R-2 at 90°C. These preliminary results indicate that displacements per atom (dpa) is a good damage parameter for correlating yield stress changes in solution annealed 316 stainless steel in fission and fusion environments. The failure of dpa to completely correlate earlier 316 SS tensile data is apparently due to temperature effects, which are observed in the present data. In pure copper, however, dpa is not an effective correlation parameter. In 316 SS the strengthening effect per dpa is the same in both neutron spectra, while there are additional spectral effects in copper. Tensile tests are in progress on higher fluence 316 SS and copper specimens, as well as on ferritic materials and copper alloys.

6.0 References

1. H. L. Heinisch. Damage Analysis and Fundamental Studies, Quarterly Progress Report July-September 1985, DOE/ER-0046/23, U. S. Department of Energy, 58 (1985).

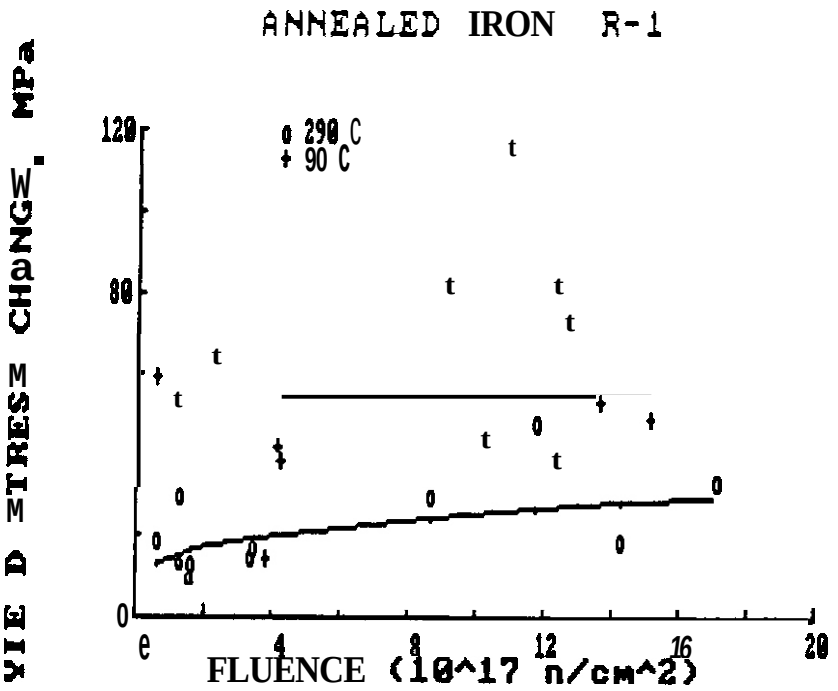

FIGURE 1. Change in 0.2% Offset Yield Stress as a Function of 14-MeV Neutron Fluence in Annealed Marz Grade Iron at 90°C and 290°C.

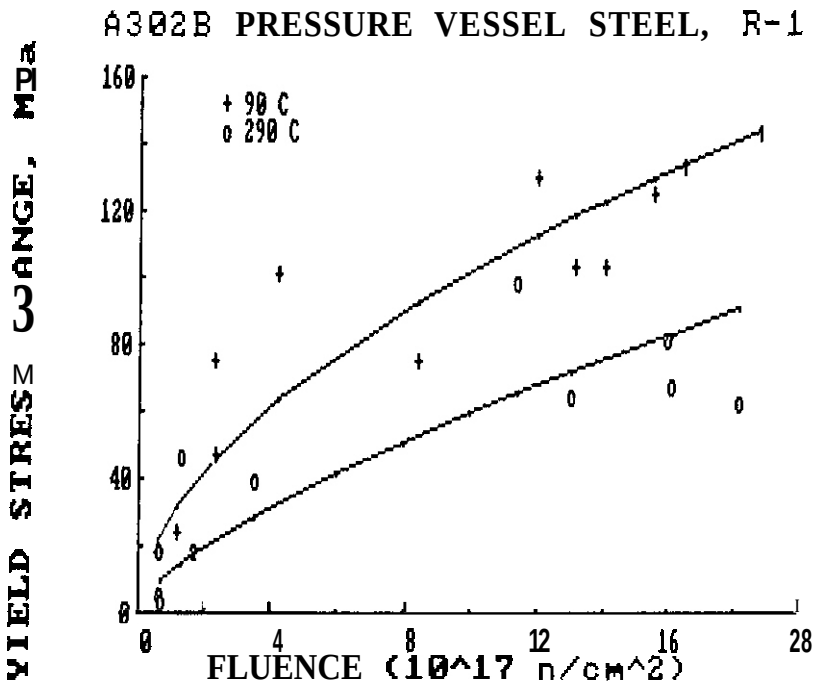

FIGURE 2. Change in 0.2% Offset Yield Stress as a Function of 14-MeV Neutron Fluence in A3028 Pressure Vessel Steel at 90°C and 290°C.

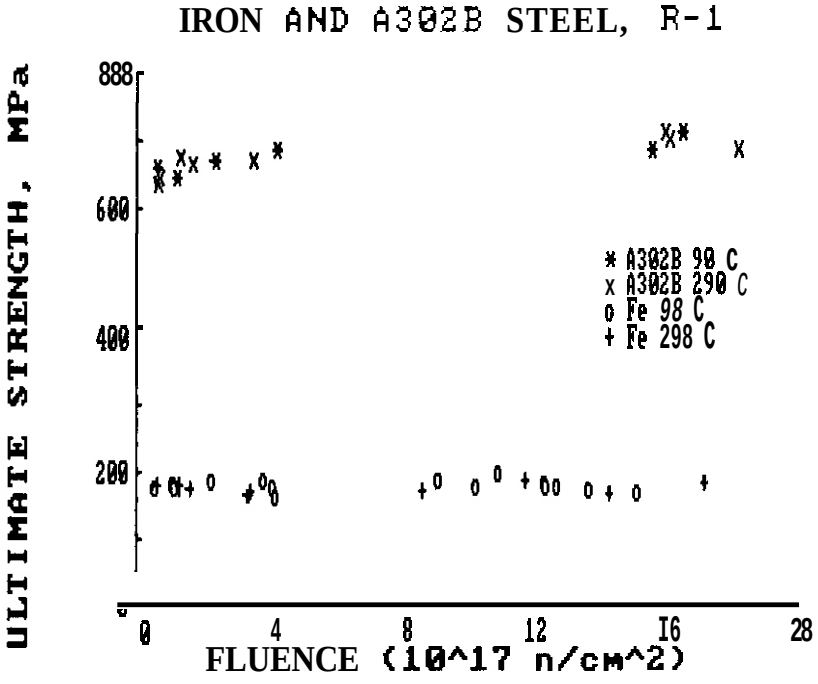

FIGURE 3. Ultimate Tensile Strength of Iron and A3028 Steel as a Function of 14-MeV Neutron Fluence at 90°C and 290°C.

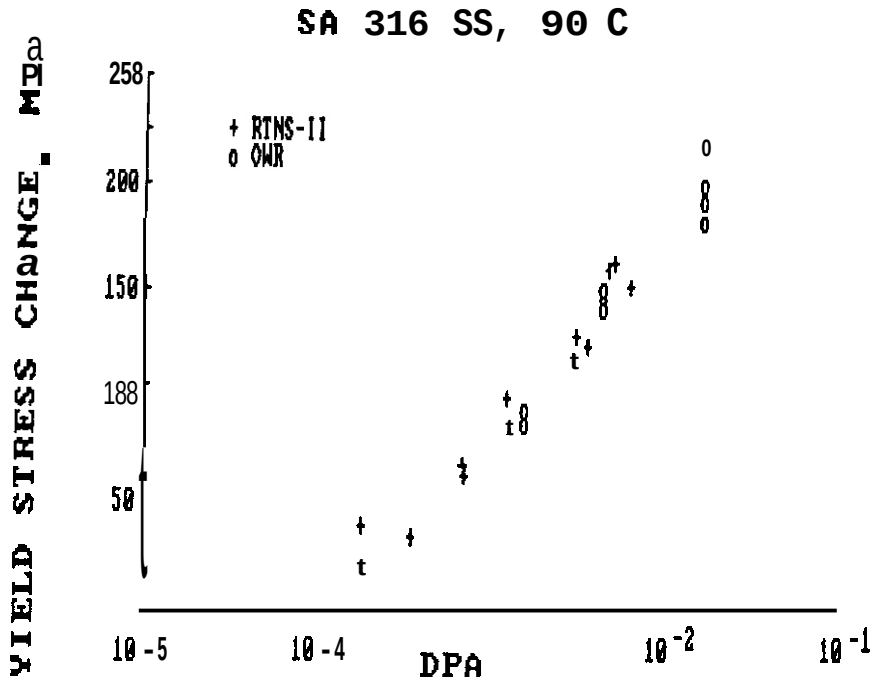

FIGURE 4. Change in 0.2% Offset Yield Stress as a Function of dpa for Solution Annealed 316 Stainless Steel Irradiated in RTNS-II and OWR at 90°C.

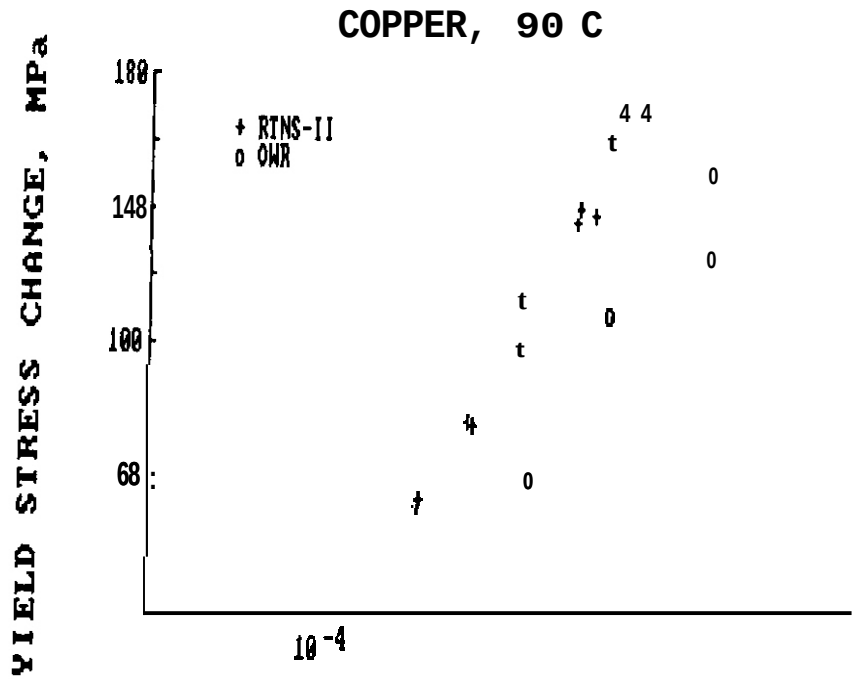

FIGURE 5. Change in 0.2% Offset Yield Stress as a Function of dpa for Annealed Copper Irradiated in RTNS-II and OWR at 90°C.

MICROSTRUCTURAL EXAMINATION OF Fe-Cr BINARY FERRITIC ALLOYS FOLLOWING IRRADIATION TO 15 DPA IN FFTF

D. S. Gelles (Hanford Engineering Development Laboratory)

1.0 Objective

The objective of this work is to determine the effect of neutron irradiation on microstructural development in simple ferritic alloys. The present experiment also allows comparisons due to spectrum differences between EBR-II and FFTF.

2.0 Summary

Microstructural examinations are reported for six Fe-Cr binary alloys (from 3 Cr to 18 Cr) following irradiation in FFTF at 430°C to 15 dpa. All specimens contained radiation damage such as dislocation loops and voids. Swelling was highest, 0.26 percent, in the Fe-9Cr alloy with a corresponding dislocation network comprising equal parts of a <100> and α/2 <111> Burgers vectors. Less swelling was found in other alloys with corresponding dislocation structures composed mainly of a <100> loops. An example of a deformation slip band containing elongated voids was found which indicates that channel fracture may occur in ferritic alloys that contain uniform void swelling.

3.0 Program

Title: Irradiation Effects Analysis (AKJ)
Principal Investigator: D. G. Doran
Affiliation: Hanford Engineering Development Laboratory

4.0 Relevant Program Plan TaskISubtask

Subtask II.C.I Effects of Material Parameters on Microstructure
Subtask II.C. Effects of Damage Rate and Cascade Structure on Microstructure

5.0 Accomplishments and Status

5.1 Introduction

Microstructural evolution in iron and ferritic alloys as a result of irradiation has been a topic for investigation for almost 25 years. Early efforts were concerned with the nature of point defect clusters[1-2] and it was found that although α/2 <111> clusters were expected, a <100> clusters could form as well]. Most of the early theoretical efforts attempted to explain the presence of α <100> loops in iron[3-4] (whereas α <100> loops were not found in other body centered cubic (bcc) metals]. Then voids were identified,[5-7] although swelling was low for the irradiation conditions examined. More recent efforts have verified that iron and ferritic steels are relatively low swelling materials.[8-10] Several explanations have been given for this[11-12] but the most reasonable explanation presentlv available attributes the low swelling to the bcc structure which has inherently lower relaxation volumes for vacancies and interstitials due to lower nearest neighbor packing.[12] This results in a significantly lower bias for interstitials at dislocations and lower swelling rates in bcc as compared to fcc structures.

In part, the low swelling of ferritic alloys has led to their consideration for application as structural materials in nuclear reactors, including the first wall of a fusion reactor.[13] Therefore,

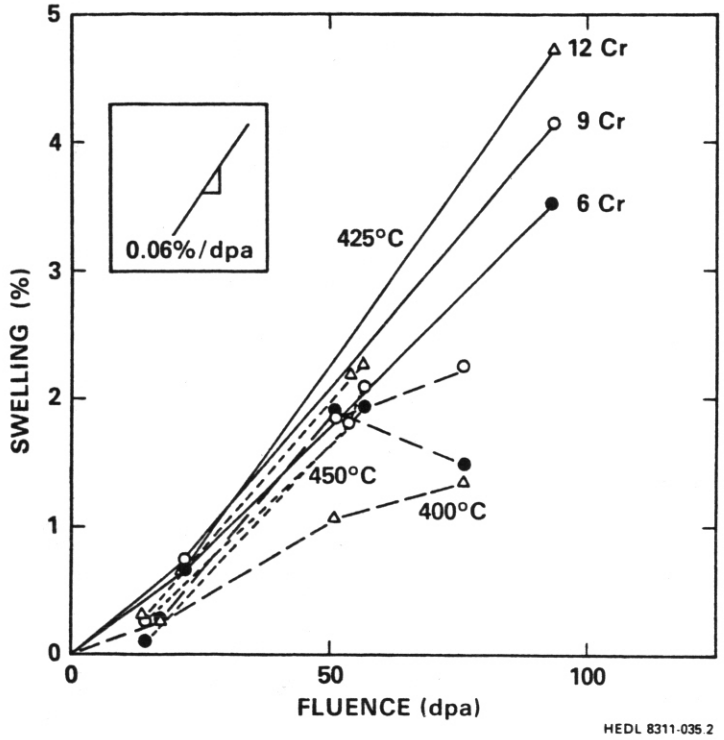

FIGURE 1. Swelling as Measured by Density vs Fluence for a Series of Fe-Cr Binary Alloys. The maximum steady-state swelling rate of 0.06%/dpa is indicated. Note that a small swelling incubation parameter applies and that the peak swelling is on the order of 5%.

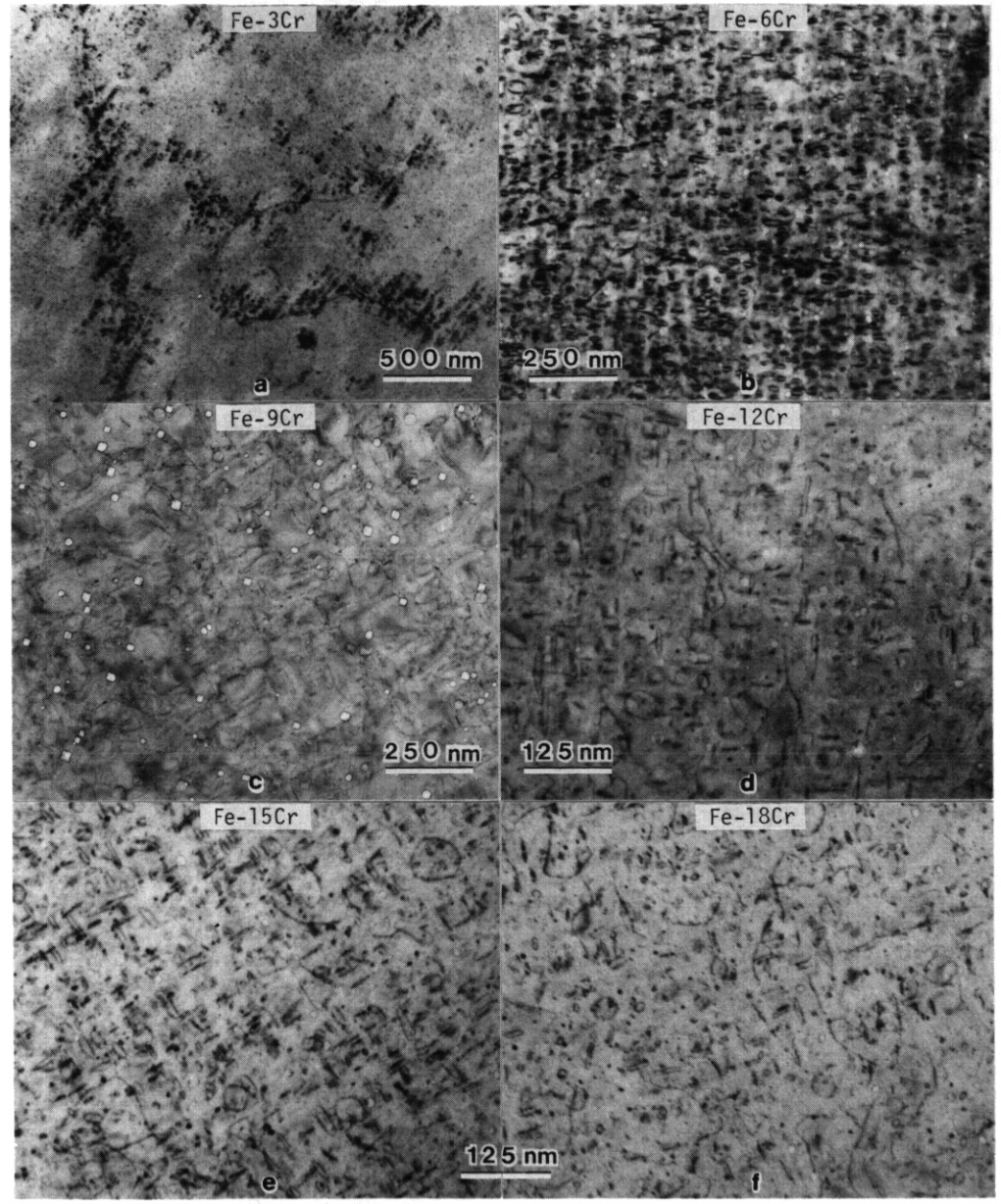

FIGURE 2. Examples of Alloy Microstructures Following Irradiation at 430°C to 15 dpa. Note changes in magnification.

microstructural evolution in general and void swelling in particular for ferritic alloys are of interest to the Damage Analysis and Fundamental Studies effort of the Fusion Reactor Materials Program. The present report describes the latest in a series of experiments by the author intended to examine microstructural evolution in Fe-Cr binary alloys due to neutron damage. Earlier reports gave results following irradiation in ERR-M[10,14] and included microstructural examinations following irradiation to doses as high as 20 dpa and density change measurements following irradiation to doses as high as 105 dpa. The microstructural examinations verified that swelling occurred in neutron irradiated ferritic alloys but was low, that dislocation evolution was complex including both a12 <111> and a <100> Burgers vectors present in the same specimen and that precipitation could develop in alloys with greater than 10 percent chromium, the precipitate being a', chromium-rich regions with bcc crystal structure. Further details can be found in Reference 14.

The density change results[10] are summarized in Figure 1. Peak swelling found was 4.72 percent for a specimen of Fe-12Cr irradiated at 425°C to 18.7 x 10^{22} n/cm^2 or 90 dpa. Similar results were obtained for Fe-6 and Fe-9Cr specimens whereas other compositions were significantly lower. However, for specimens irradiated to approximately 50 dpa, the swelling values at 400 and 450°C closely match anticipated results for 425°C. Therefore, it appears that a peak swelling rate on the order of 0.06%/dpa applies for most conditions of Fe-6 to 12 percent chromium over the temperature range 400 to 450°C. This is a factor of three lower than the theoretical prediction of 0.2%/dpa,[12] but a re-estimate based on more representative sink densities lowered that prediction to 0.04%/dpa to 0.06%/dpa.[15]

5.2 Experimental Details

The alloy series studied constituted Fe-Cr binary alloys with chromium varying from 3 to 18 percent in 3 percent increments. Details of alloy fabrication and composition have been published previously.[10,14] Disk specimens 0.3 cm in diameter by 0.02 cm thick were engraved with four digit identifying codes and loaded into four identical TEM disk packets so that each alloy was represented by a multiplicity of 10. The packets were inserted into MOTA-1B in weeper position 2F designed to operate at approximately 425°C. The first of these packets identified as FT was removed after Run 1B having received 15 dpa exposure at 431°C ± 5°C. Specimens were Identified and prepared for TEM examination using standard techniques. Examinations were performed on a JEOL JEM-1200 EX STEM microscope using a double tilting side-entry goniometer stage. Table 1 is provided to aid in the Burgers vector analysis as described in the text.

The present studies are intended to expand the earlier microstructural observations[14], to provide comparison of spectral effects (by comparing FFTF and EBR-II damage behavior) and to give a basis for higher fluence microstructural examinations.

5.3 Results

All specimens examined showed microstructural features typical of radiation damage in ferritic alloys. Voids and dislocation loops or networks were found in all specimens. However, in the Fe-3Cr alloy specimen, loops and voids were non-uniformly distributed whereas in the other alloys, the distributions were much more uniform. The non-uniformities in Fe-3Cr were a result of loop and void development in the vicinity of pre-existing dislocations. Also, precipitate development was found in Fe-3Cr, Fe-12Cr, Fe-15Cr and Fe-18Cr specimens, the former believed to be due to impurities in the alloy[9] and the latter three to α' formation.

Examples of the irradiated microstructures are given in Figure 2. Figure 2a shows the dislocation structure of Fe-3Cr at low magnification. Dislocation loops appear in non-uniformly distributed bands which in two cases can be identified with long dislocations. [The imaging condition used, g = 01$\bar{1}$, should show 213 of the possible a <100> dislocations and 112 of the possible α/2 <111> dislocations.] Individual loops appear to be oriented in rows parallel to (01$\bar{1}$). The fine background which can be seen is due to precipitation and a few examples of small voids can be identified. Figures 2b and c show alloys Fe-6Cr and Fe-9Cr at intermediate magnification. In both cases, voids are well developed, but the alloys have different dislocation structures. The Fe-6Cr specimen contains individual dislocation loops predominantly of a <100> type whereas the Fe-9Cr dislocation structure has evolved into a dislocation network. Figure 2b of Fe-6Cr is in 200 contrast near an (010) foil orientation so that 113 of the possible a <100> dislocations and all of the a12 <111> dislocations are visible. Figure 2c of Fe-9Cr is in a complex contrast condition near an 010 foil orientation. Figures 2d, e and f show alloys Fe-12Cr, Fe-15Cr and Fe-18Cr at higher magnification. In all three cases, the dislocations are imaged in 101 contrast near an 010 foil orientation so that 213 of the α <100> dislocations and 112 of the α/2 <111> dislocations can be seen. In each case, the dislocation structure contains both types of Burgers

TABLE 1

THE g · b IMAGING CRITERION FOR VARIOUS bcc
MAJOR IMAGING CONDITIONS AND BURGERS VECTOR POSSIBILITIES

	b						
g	α/2 [111]	α/2 [$\bar{1}$11]	α/2 [1$\bar{1}$1]	α/2 [11$\bar{1}$]	a [100]	a [010]	a [001]
200	1	1	1	1	2	0	0
020	1	1	1	1	0	2	0
002	1	1	1	1	0	0	2
01$\bar{1}$	0	0	1	1	0	1	1
110	1	0	0	1	1	1	0
$\bar{1}$10	0	1	1	0	1	1	0
10$\bar{1}$	0	1	0	1	1	0	1
11$\bar{2}$	0	1	1	2	1	1	2
1$\bar{2}$1	0	1	2	1	1	2	1
$\bar{2}$11	0	2	1	1	2	1	1
2$\bar{1}$1	1	1	2	0	2	1	1
21$\bar{1}$	1	1	0	2	2	1	1
1$\bar{1}$2	1	0	2	1	1	1	2
12$\bar{1}$	1	0	1	2	1	2	1

vectors, with both loops and network structure present. Therefore, the microstructural development as a function of chromium content can be described as follows. The microstructural evolution is most advanced in the Fe-9Cr specimen where a dislocation network has been attained. Fe-12 to Fe-18 are not quite as advanced; a dislocation network is beginning to form. The Fe-6Cr is less advanced and contains a uniform distribution of small loops, and the Fe-3Cr alloy is least developed with large regions where dislocation loops are not present. However, it is likely that in the Fe-3Cr specimen, this is due to impurities in the alloy which produce a high number density of small precipitate particles.

Figure 3 has been prepared to show the microstructure of the Fe-3Cr specimen in greater detail. The same region is shown in void contrast and in three different dislocation imaging conditions. The larger voids are found to be truncated cuboids with 100 faces and 111 facetted corners. Comparison of the void and the dislocation micrographs shows that voids form in the regions where dislocation loops are developed. However, the voids are not directly coupled to loops, nor does the nucleation site of the void appear to coincide with the loop nucleation site. Comparison of the loops in Figures 3b and c reveals that the change of imaging conditions between $\bar{2}$00 and 0 1$\bar{1}$ shows completely different populations of loops. This is because all loops are of α <100> type as can be shown from Table 1. (Some confusion exists due to weak images visible in Figure 3b. However, the habit plane of all loops is {100} as revealed by stereoscopic examination and therefore, these residual images are believed due to the anisotropic nature of the elastic constants for iron.) Note that all a <100> loops should be visible in Figure 3d with 172 contrast but the α [001] loops are in strongest contrast. Also note that the long dislocation running vertically is visible in all imaging conditions shown and is in strong contrast in Figure 3d. Therefore it is of α/2 [1$\bar{1}$1] type and must be largely screw in character. It was probably retained from the preirradiation structure.

Figure 4 provides examples of the irradiated Fe-6Cr microstructure in greater detail. The same area is shown in void contrast and three different dislocation contrast conditions for a foil near an (001)

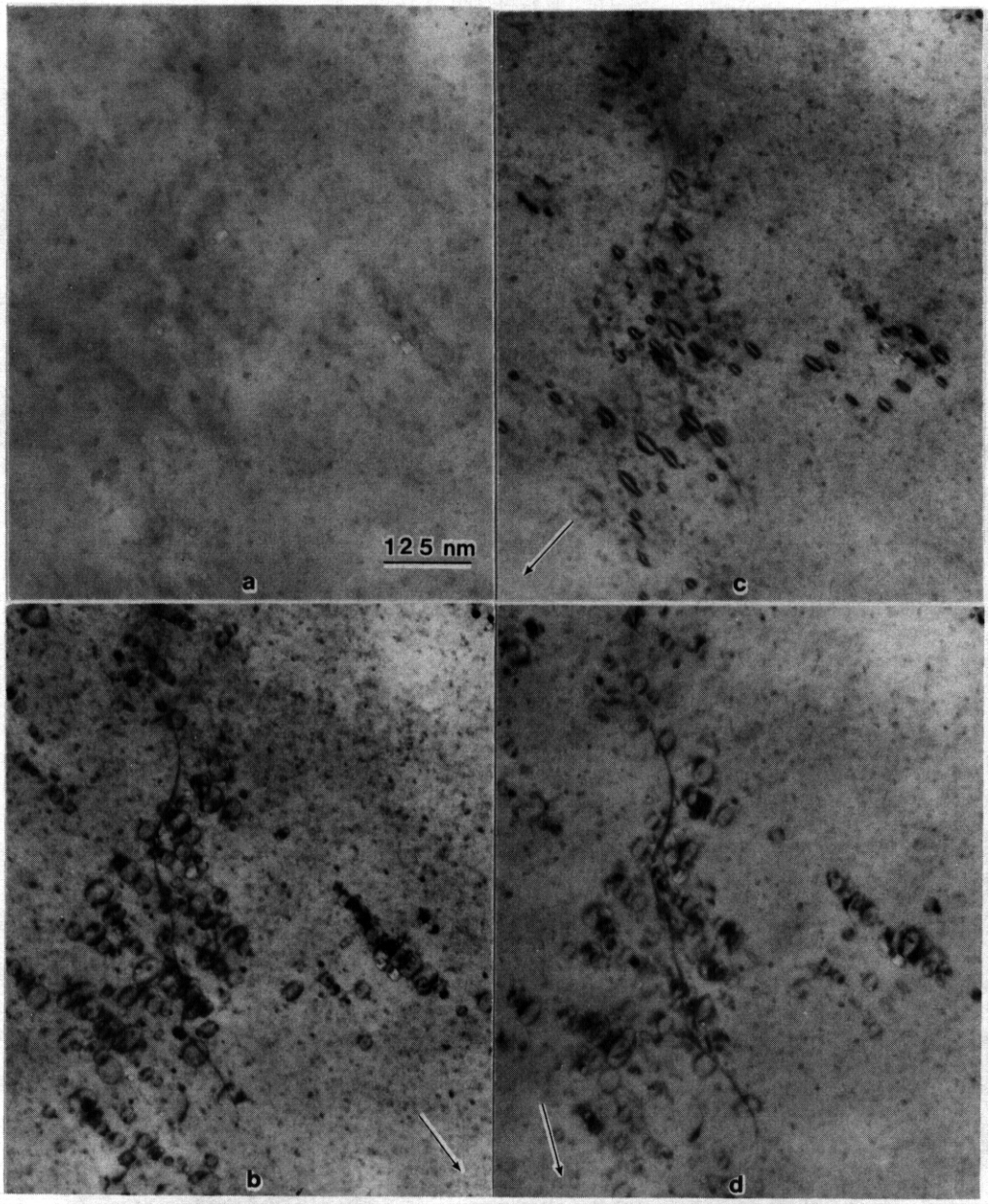

FIGURE 3. The Microstructure of Fe-3Cr Irradiated at 430°C to 15 dpa Shown in Various Imaging Conditions: a) Void Contrast; b) $\bar{2}00$ Contrast; c) $01\bar{1}$ Contrast; and d) $1\bar{1}2$ Contrast, Foil Thickness 194 nm. Arrows define operating g vectors.

Therefore, the void shape has been altered in changing the composition from 3Cr to 6Cr. The dislocation structure consists primarily of small unfaulted loops on {001} planes. Comparison of Figures 4b (showing a [100] loops in strong contrast) and 4d (showing a [010] loops in strong contrast) does reveal in both cases larger weak dislocation images which can be seen more clearly in Figure 4c using $\bar{1}10$ contrast. These weaker images must be of a12 <111> type and therefore both types of dislocations are present. Of particular note is the α/2 <111> loop marked by the arrow in Figure 4c. This indicates that the a12 <111> dislocation structure probably grew from loops which developed at the same time as did the a <001> loops. However, apparently α/2 <111> dislocations climb more rapidly.

Figure 5 provides an example for the Fe-9Cr alloy irradiated at 430°C to 15 dpa. The imaging conditions are similar to those for Figure 3, with a foil orientation near (011). Figure 5a shows the void structure in weak $01\bar{1}$ dislocation contrast. The voids are found to be of truncated octahedral shape (with {111} faces and truncated (100) corners). As very few small voids can be identified it is likely that void nucleation has been completed. Dislocation structure is shown in Figures 5b, c and d. Figure 5b is shown in 200 dislocation contrast so that a [100] dislocations are in strong contrast and all possible a12 <111> dislocations are shown in weaker contrast. In general, the strong vertical images are

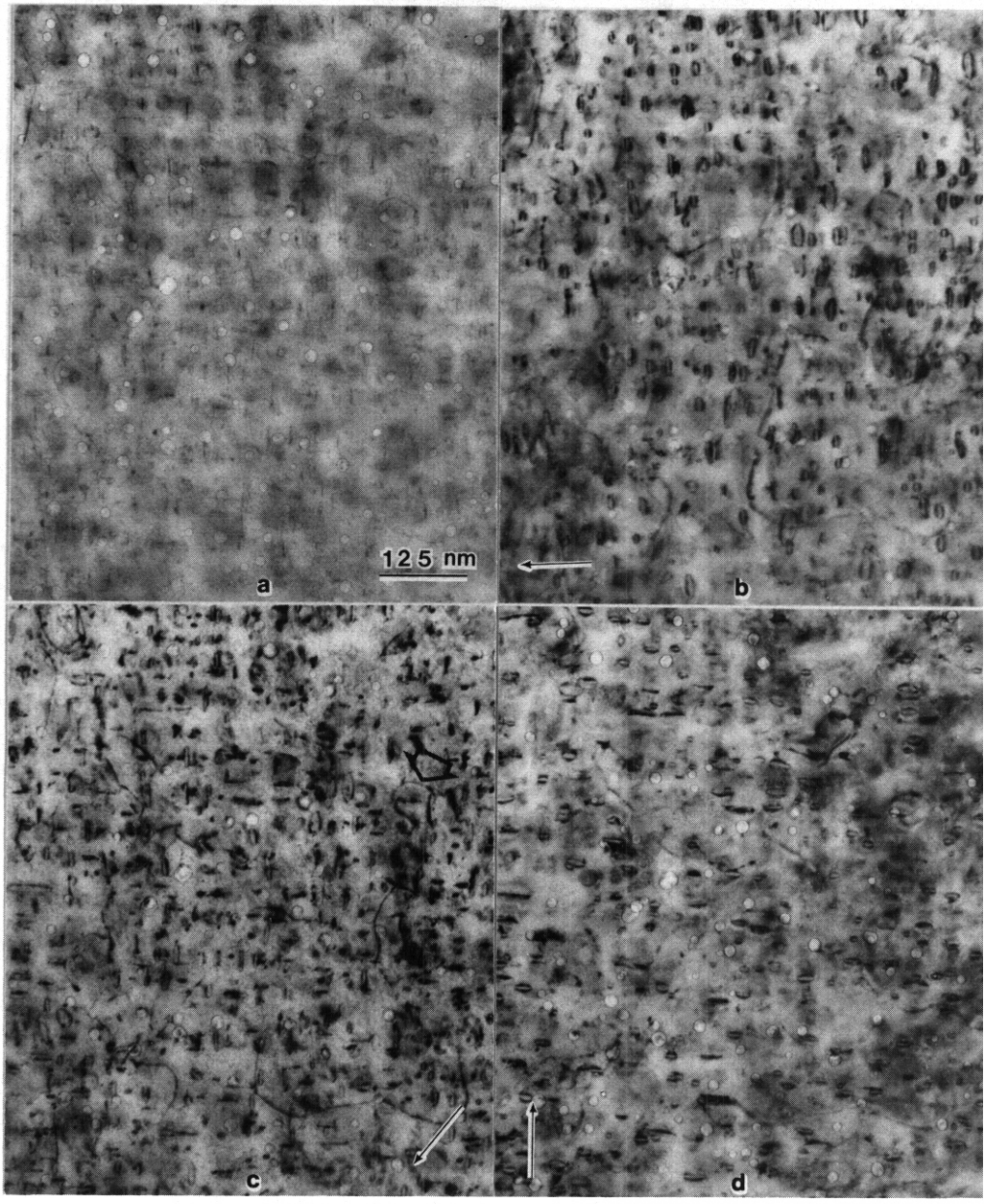

FIGURE 4. The Microstructure of Fe-6Cr Irradiated at 430°C to 15 dpa Shown in Various Imaging Conditions: a) Void Contrast; b) 200 Contrast; c) $\bar{1}10$ Contrast; and d) 020 Contrast, Foil Thickness 100 nm.

α [100] dislocations and therefore most α [100] dislocation loops have grown to either intersect other loops or to reach the foil surfaces. Dislocation climb has apparently occurred more rapidly in-the Fe-9Cr condition. Comparison of Figures 5b and c should reveal a [100], α/2 [111], and a12 [111] dislocations only in Figure 5b and α [010] and α [001] only in Figure 5c whereas dislocations which appear in both figures must be either α/2 [$1\bar{1}1$] or a12 [$11\bar{1}$] types. The loops showing in Figure 5c are therefore of α [010] and α [001] type and it is apparent that several have grown quite large, possibly by coalescence. However, several examples exist where a dislocation network including a <100> components has formed. Several examples of α/2 [$1\bar{1}1$] and α/2 [$11\bar{1}$] dislocations can also be identified as part of the network. Therefore, the dislocation network contains both a <100> and α/2 <111> components. Figure 5d allows identification of α [001] and α/2 [$11\bar{1}$] in strong contrast and a [100] and α/2 [111] in weaker contrast in comparison with Figure 5c where α [100] and α/2 [111] are not visible.

Figure 6 provides an example for the Fe-12Cr alloy which gives similar geometries to those shown in Figure 4 for Fe-6Cr. The void structure is shown in Figure 6a which indicates a range of void shapes from truncated octahedra with 111 faces and truncated 100 corners to more equiaxed shapes with 111 and 100 faces in equal proportion. Also of note are background features indicative of α' precipitation. The dislocation structures are shown in Figures 6b, c and d. Comparison of Figures 6b and 6d show the two

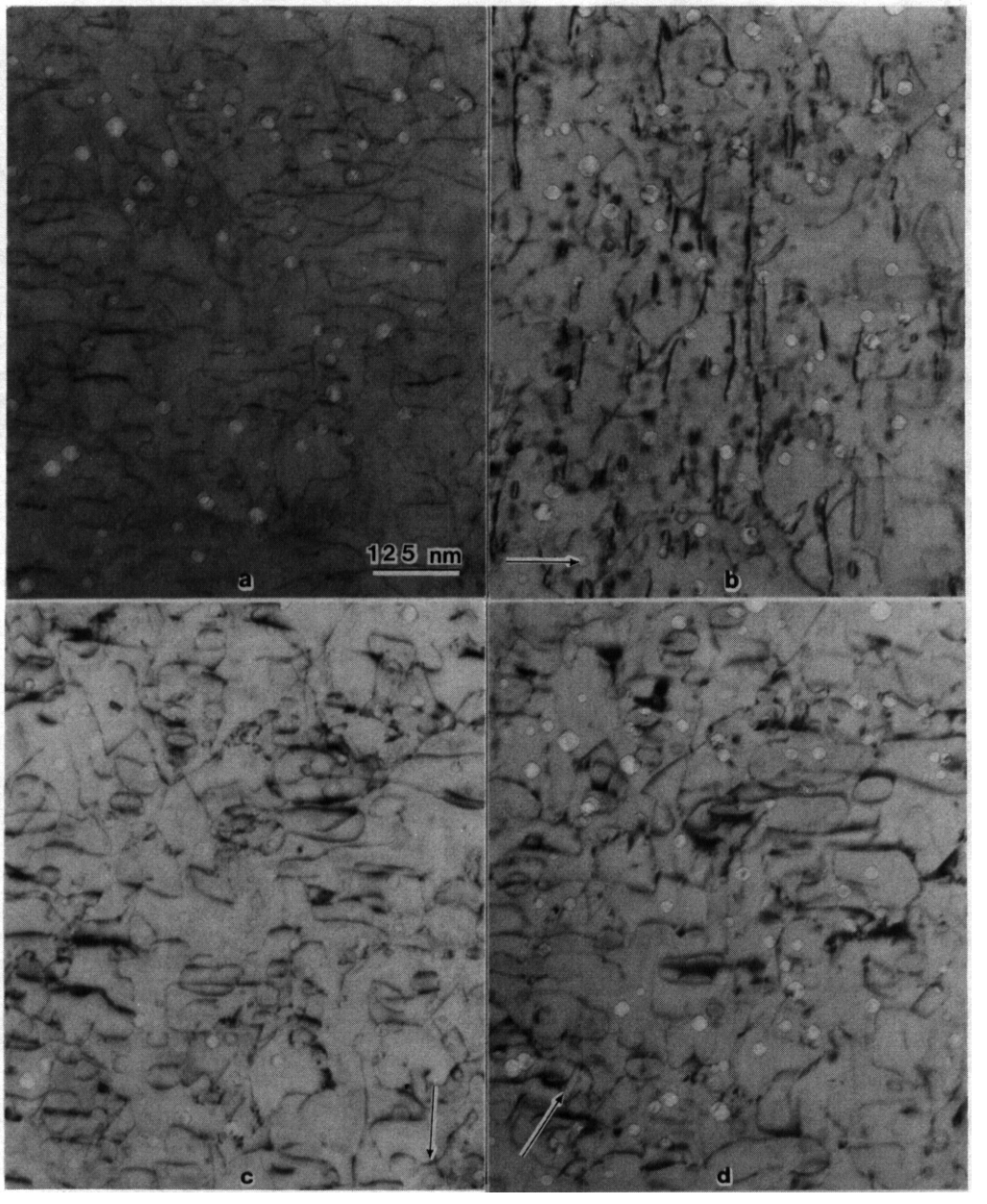

FIGURE 5. The Microstructure of Fe-9Cr Irradiated at 430°C to 15 dpa Shown in Various Imaging Conditions; a) Void Contrast; b) 200 Contrast; c) 011 Contrast; and d) 112 Contrast, Foil Thickness, 116 nm.

sets of a [100] and a [010] loops oriented orthogonally. Weakly imaged are the α/2 <$\bar{1}$11> type dislocations. Figure 6c shows the α/2 [111] and a12 [111] dislocations in stronger contrast and because the α/2 <11$\bar{1}$> dislocations are longer, again indicates that α/2 <111> dislocation climb is more rapid than a <100> climb. Therefore, except for observed precipitation this structure appears to be very similar to that of Fe-6Cr as shown in Figure 4.

Figure 7 shows the irradiated Fe-15Cr microstructure under conditions similar to those of Figure 6. The foil is near an (001) orientation and as shown in Figure la, voids appear as equiaxed highly truncated octahedra with 100 and 111 faces. The dislocation structure is predominantly a <100> loops but several examples of a12 <111> loops and some network structure can be identified, most easily found in Figure 7c. Figure 7 also reveals small dark images, most noticeable in Figure 7c, but also present in Figures la, b and d. Similar features can be found in Figure 6. The cause of such features is not yet understood. They appear surprisingly strongly in the weak dislocation contrast conditions of Figure la and different features show in Figures 7c and 7d. Therefore, these features may be small dislocation loops of a Burgers vector different than α <100> or α/2 <111> but more likely they are images which arise from a' precipitates. The α' precipitates are of a similar size.

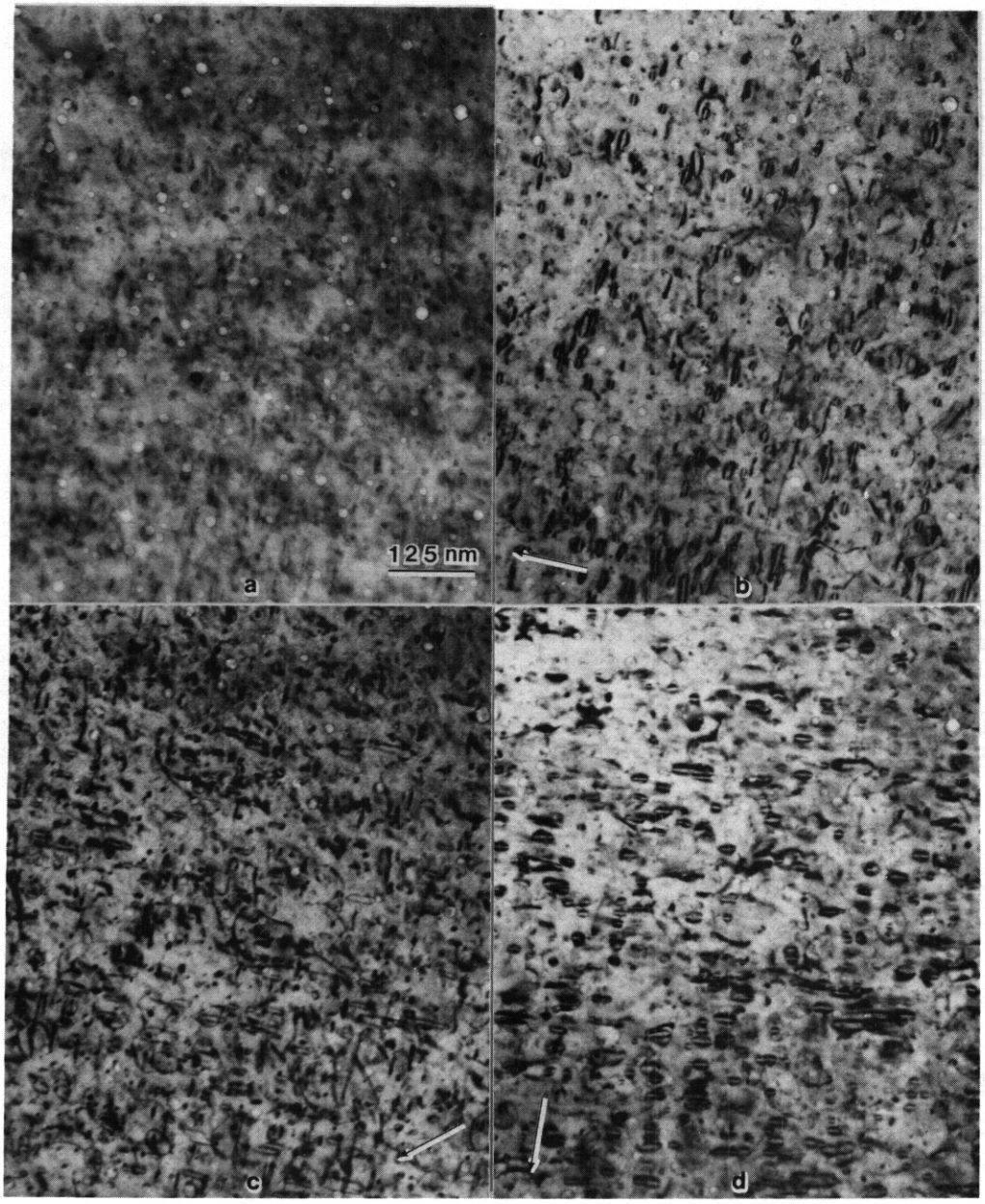

FIGURE 6. The Microstructure of Fe-12Cr Irradiated at 430°C to 15 dpa Shown in Various Imaging Conditions: a) Void Contrast; b) 200 Contrast; c) $\bar{1}10$ Contrast; and d) 020 Contrast, Foil Thickness 116 nm.

Figure 8 provides examples of the microstructure found in irradiated Fe-18Cr. The imaging conditions are similar to those shown in Figure 6. Examination of Figure 8 reveals void and dislocation structures similar to those found in Figures 6 and 7 for Fe-12Cr and Fe-15Cr specimens. The major differences arise from the higher density of large $\alpha/2$ <111> dislocations.

In the course of specimen preparation, thin foils are occasionally damaged. This often results in tearing, cracking and extensive buckling of the foil. Evidence of such damage was observed in a specimen of irradiated Fe-6Cr. However, it was found that the damage was restricted to a narrow slip band and that general buckling was not observed. Figure 9 is provided to show this example. A region is shown in 110 weak dislocation contrast so that all voids, 2/3 of the α <100> and 1/2 of the $\alpha/2$ <111> dislocations can be identified. Diagonally across this micrograph, a slip band appears in absorption contrast so that voids can be seen. The voids are found to have been deformed into highly extended geometries. This micrograph reproduces features typically found in irradiated austenitic stainless steels which are found to fail by channel fracture.[16] Such an observation in irradiated Fe-6Cr suggests that channel fracture may also be observed in ferritic steels which have been irradiated.

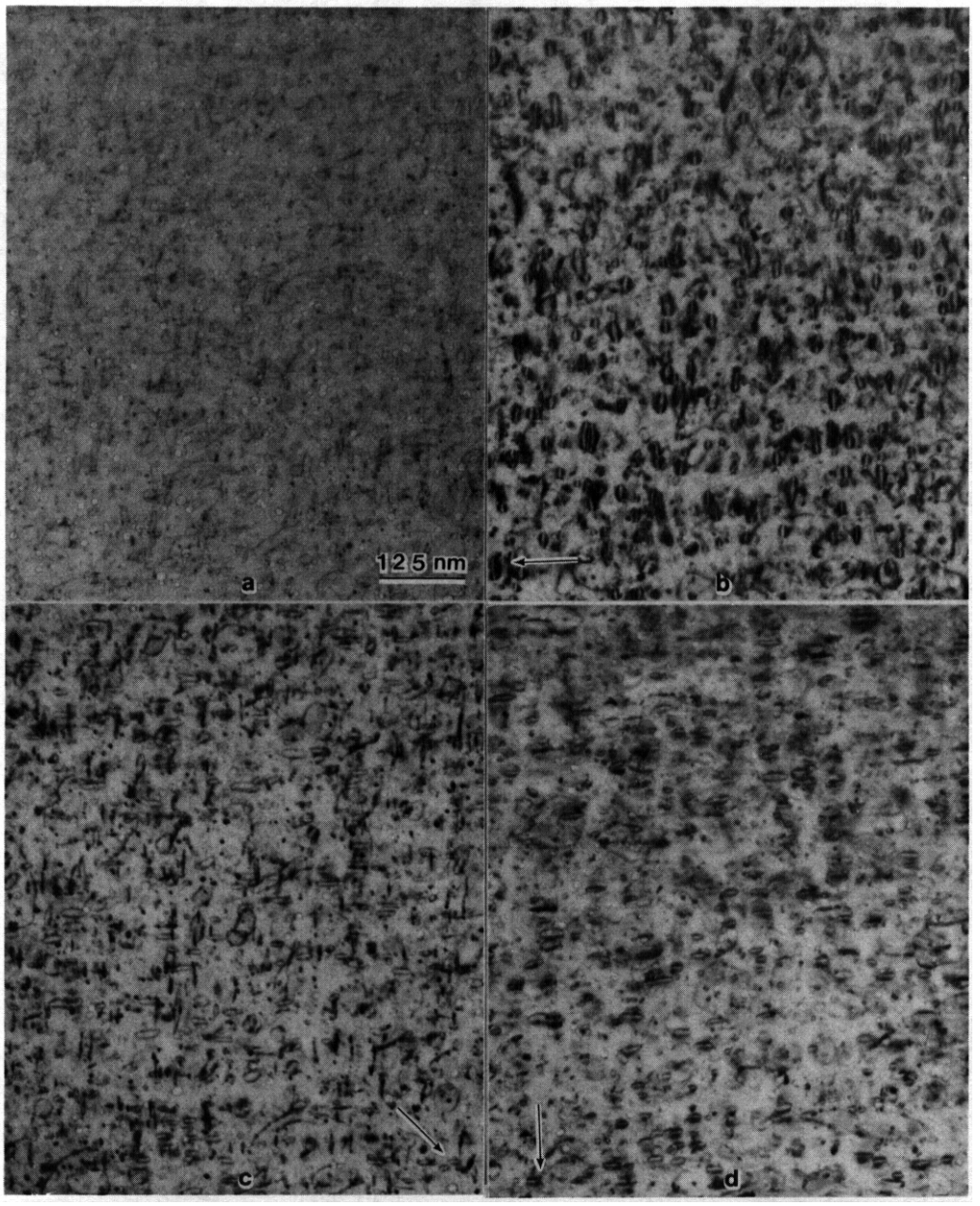

FIGURE 7. The Microstructure of Fe-15Cr Irradiated at 430°C to 15 dpa Shown in Various Imaging Conditions: a) Void Contrast; b) 200 Contrast; c) 110 Contrast; and d) 020 Contrast, Foil Thickness 174 nm.

The micrograph series presented in Figures 3 through 8 were used to provide quantitative void and dislocation information as a function of chromium content. After the foil thickness was determined for the area of interest, voids were measured to provide void volume ($\Delta V/V$), mean diameter (d) and number density. Analysis for α <100> loops was based on one 200 imaging condition and the results were tripled in order to account for the other orientations. The 200 imaging condition was also used to determine the α/2 <111> dislocation line length per unit volume (weak images) and where relevant, the *a* <100> dislocation line length per unit volume (strong images) excluding loops, the measurement tripled. The results are given in Table 2. Where both *a* <100> loops and dislocation tangles were present, the value for the a <100> line length includes both measurements.

From Table 2, it can be shown that swelling is found to be greatest in the Fe-9Cr alloy, less in the Fe-6Cr and Fe-12Cr alloys and least in the Fe-18Cr, Fe-15Cr and Fe-3Cr alloys, in that order. The higher swelling in the Fe-9Cr alloy of 0.26 percent arises from the growth or larger voids than in the Fe-6Cr or Fe-12Cr alloys. The void number density is in fact highest in the Fe-15Cr and Fe-18Cr alloys. The swelling as a function of chromium content is shown in Fiqure 10. The dislocation measurements show that the highest density for α <100> loops occurred at Fe-6Cr and Fe-12Cr, but the greatest swelling occurred in Fe-9Cr when the *a* <100> dislocation line length was lower and about equal to the a12 <111> dislocation line length.

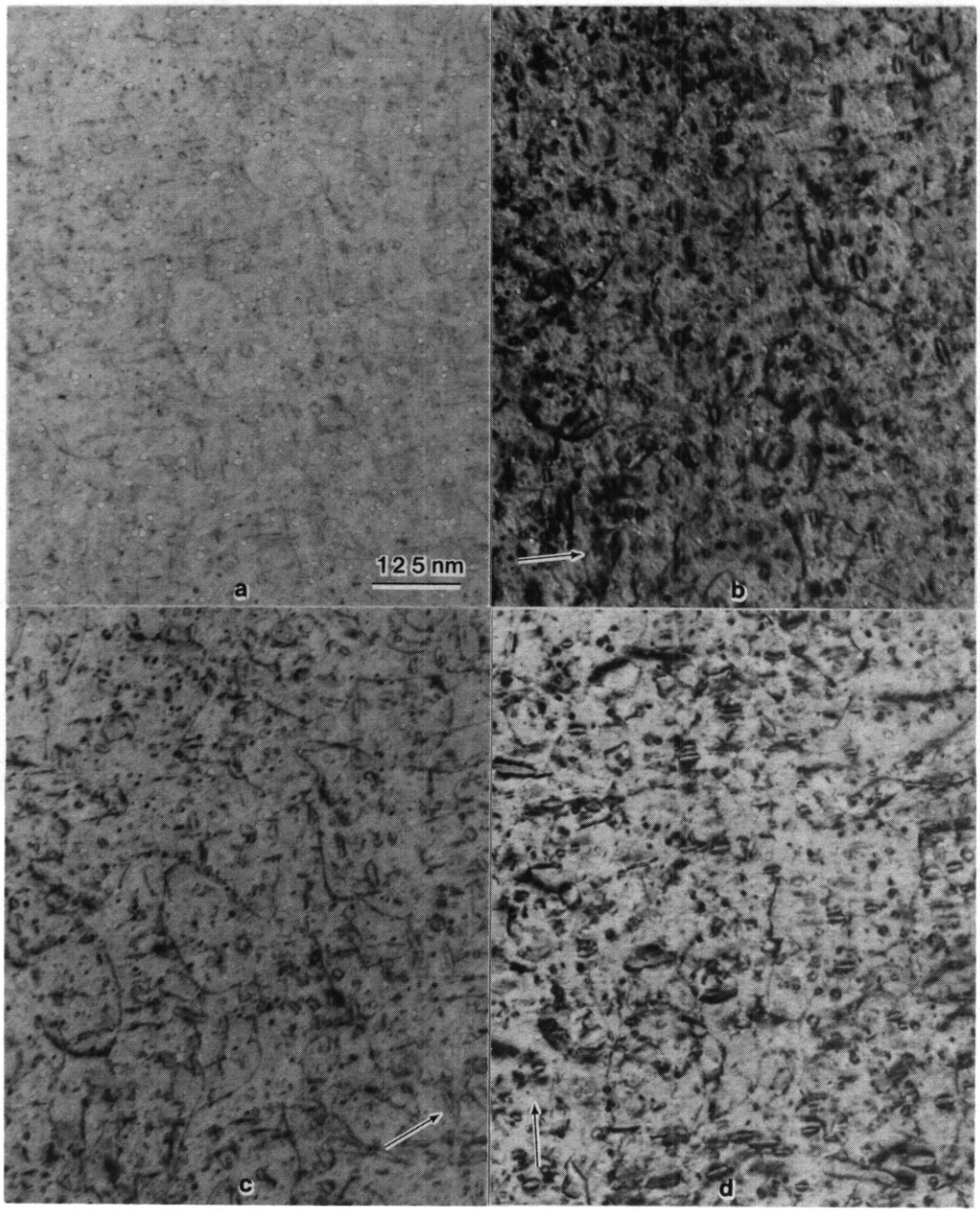

FIGURE 8. The Microstructure of Fe-18Cr Irradiated at 430°C to 15 dpa Shown in Various Imaging Conditions: a) Void Contrast; b) 200 Contrast; c) $\bar{1}10$ Contrast; and d) 021 Contrast, Foil Thickness 200 nm.

5.4 Discussion

5.4.1 Comparison with Previous Results

Two similar studies of neutron damage in iron-chromium alloys can be compared with the present work.[14,17] The levels of swelling given in Table 2 compare favorably with those on the same alloys irradiated in EBR-II.[14] This can be shown by examining Figure 1 which presents that data base. Swelling on the order of 0.25 percent or less at a fluence of 15 dpa exactly corresponds to previous values obtained following irradiation at 450°C to 14 dpa. However, the swelling as a function of composition is somewhat different and the void density is higher. Swelling as a function of chrmium content is more sharply peaked at 9Cr than had been found previously with the same alloys. The most plausible explanation relates to the difference in dislocation evolution found as a function of chranium content. This difference represents the incubation dose determining factor. Area to area variations in incubation dose might explain the swelling differences. This explanation suggests that other areas in the Fe-9Cr specimen would be found to contain less swelling. The intermediate swelling at Fe-15Cr and

FIGURF 9. A Deformation Rand in 110 Contrast in Fe-Cr Irradiated at 430°C to 15 dpa and Then Deformed During Handling.

Fe-18Cr is in better agreement with results by Little and Stow. This is shown in Figure 11 where the present results are compared with results from EBR-II[14] and DFR[17]. Therefore, it can be anticipated that lower irradiation temperatures will produce higher swelling in high chromium alloys and that higher chromium alloys have somewhat lower peak swelling temperatures. This difference is probably due to α' precipitation.

The major difference between the present results and previous results is microstructural scale. The present results give void number densities at a factor of 4 to 6 higher and dislocation densities about a factor of 3 higher than previous results for the same alloys irradiated in ERR-11. Void number densities were still lower in the Dounreay Fast Reactor (DFR) experiments.[17] The difference can be partly explained based on improved image resolution between the present work and previous results on the same specimens. However, it is more likely that the differences arise from different reactor experimental conditions such as differences in displacement rate or irradiation temperature. Further work is needed to resolve this point.

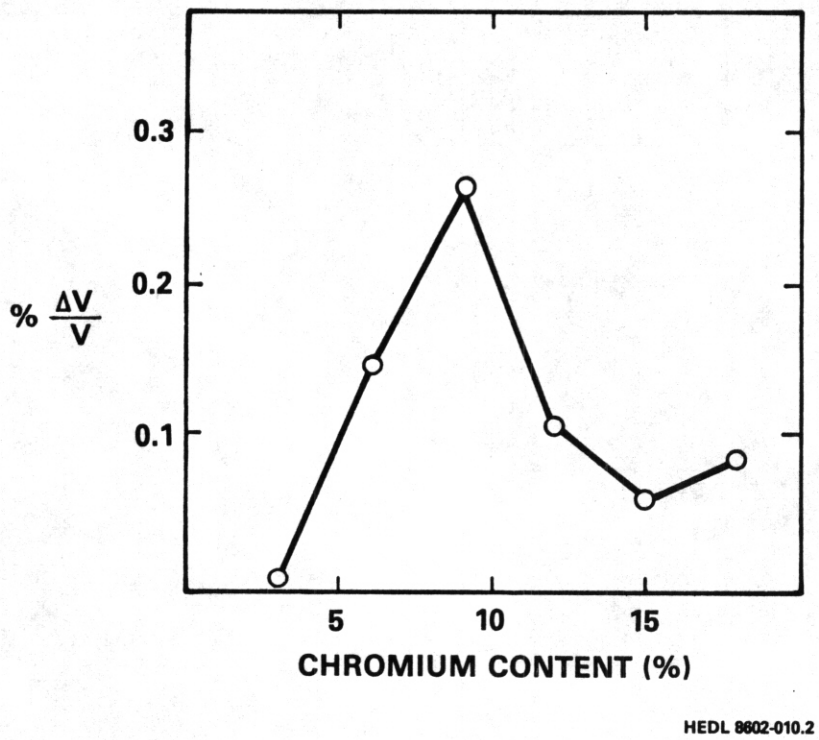

FIGURE 10. Swelling in Fe-Cr Binary Alloys Irradiated at 430°C to 15 dpa as a Function of Chromium Content.

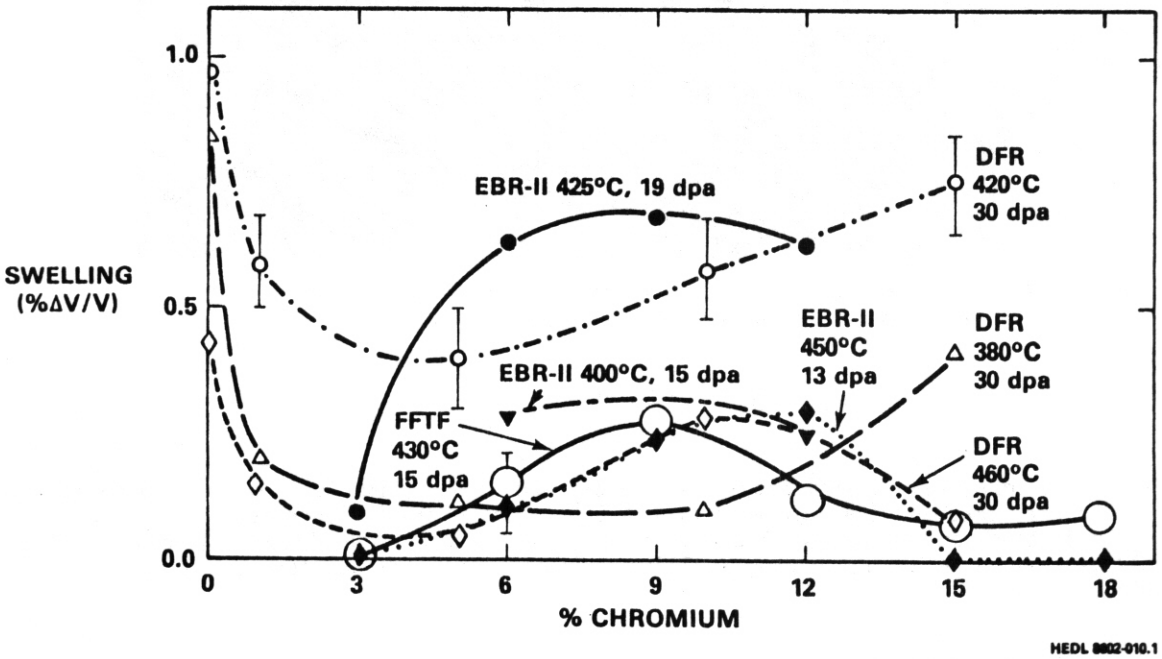

FIGURE 11. Comparison of Swelling as a Function of Chromium Content in Various Fast Reactors.[14,17]

5.4.2 Swelling Incubation

The present results indicate steady state swelling rates considerably below maximum rates found previously (0.264% in 15 dpa or 0.018%/dpa as compared to 0.06%/dpa). Therefore swelling incubation parameters greater than zero probably apply. The present microstructural results can be interpreted to suggest that swelling will only approach steady state in Fe-Cr alloys after a dislocation network is obtained. Specimens with the greatest swelling have the most advanced dislocation network development. Other examinations by the author are in agreement with such a model.

5.5 Conclusions

Fe-Cr binary alloys covering the composition range 3 to 18 percent chromium have been examined using transmission electron microscopy following irradiation in FFTF to 15 dpa at 430°C. Radiation damage in the form of voids and dislocation loops was found in each condition. Peak swelling occurred in a specimen of Fe-9Cr which corresponded with a network dislocation structure of equal parts a <100> and α/2 <111> Burgers vectors. In comparison Fe-6Cr and Fe-12Cr had less swelling and Fe-15Cr and Fe-18Cr even less, in all cases the microstructures consisting of uniformly distributed voids and a <100> dislocation loops with some larger α/2 <111> loop and dislocation lines present. The Fe-3Cr showed the least microstructural development due to non-uniform nucleation of loops and voids near pre-existing dislocations. An example of slip band deformation was identified in a specimen of Fe-6Cr which appears to indicate that channel fracture may occur in ferritic alloys which contain void swelling.

5.6 Future Work

This work will be continued by performing examinations of the same alloys irradiated in FFTF to 40 dpa.

6.0 References

1. B. L. Eyre, "Direct Observation of Neutron Irradiation Damage in a-Iron," Phil. Mag. 7 p. 2107, 1962.
2. E. C. Masters, "Dislocation Loops in Irradiated Iron," Phil. Mag. 11, p. 881, 1965.
3. B. L. Eyre and R. Bullough, "On the Formation of Interstitial Loops in B.C.C. Metals, Phil. Mag. 12, p. 31, 1965.
4. R. Rullough and R. C. Perrin, "The Morphology of Interstitial Aggregates in Iron, Proc. Royal Soc. A305, p. 541, 1968.
5. G. L. Kulcinski, B. Mastel and J. L. Rrimhall, "Formation of Voids in Iron During High Temperature Irradiation." Rad. Eff. 2, p. 57, 1969.
6. K. Farrell and J. Houston, "Non-Randomly Distributed Irradiation Voids in Iron." J. Nucl. Matl. 35, p. 352, 1970.
7. Y. Adda, "Report on the CEA Program of Investigations of Radiation-Induced Cavities in Metals: Presentation of Some Results," Radiation-Induced Voids in Metals, Eds. J. W. Corbett and L. C. Ianniello, CONF-710601, p. 31, 1972.
8. E. A. Little and D. A. Stow. 'Void Swelling in Irons and Ferritic Steels, Part II," J. Nucl. Matl. 87, p. 25, 1979.
9. D. S. Gelles, "Swelling in Several Commercial Alloys Irradiated to Very High Neutron Fluence," J. Nucl. Matl. 122 & 123, p. 207, 1984.
10. D. S. Gelles and R. L. Meinecke, "Swelling in Simple Ferritic Alloy Irradiated to High Fluence," Alloy Development for Irradiation Performance Progress Report for Period Ending September 1983, DOE/ER-0045/11, p. 103, 1984.
11. E. A. Little, R. Bullough and M. H. Wood, "On the Swelling Resistance of Ferritic Steel," Proc. R. Soc. Lond. A372, p. 565, 1980.

12. J. J. Sniegowski and W. G. Wolfer, "On the Physical Basis for the Swelling Resistance of Ferritic Steels," Proc. of Topical Conf. on Ferritic Alloys for Use in Nuclear Energy Technologies, Eds. J. W. Davis and D. J. Michel (AIME Warrendale, PA, 1984).

13. D. S. Gelles, "12Cr-1Mo Steel for Fission and Fusion Applications," Ferritic Steels for High-Temperature Applications, Ed. A. K. Khare (ASM, Metals Park, OH), p. 197, 1983.

14. D. S. Gelles, "Microstructural Examination of Neutron-Irradiated Simple Ferritic Alloys." J. Nucl. Matl. 108 & 109, p. 515, 1982.

15. L. L. Horton and J. Bentley, "Swelling Behavior of a Simple Ferritic Alloy," in Proceedings of: Topical Conference on Ferritic Alloys for Use in Nuclear Energy Technologies, Eds. J. W. Davis and D. J. Michel (AIME, New York, NY, 1984), p. 569.

16. R. L. Fish, J. L. Straalsund, C. W. Hunter and J. J. Holmes, "Swellina and Tensile Prooertv Evaluations of High-Fluence EBR-II Thimbles," Effects of Radiation on Substructure and Mechanicai Properties of Metals and Alloys, Ed. J. Moteff, STP 529 (ASTM, Philadelphia, PA), p. 149, 1973.

17. E. A. Little and D. A. Stow, "Effects of Chromium Additions on Irradiation-Induced Void Swelling in a-Iron," Met. Sci., p. 89, 1980.

TARLE 2

SUMMARY OF QUANTITATIVE MEASUREMENTS OF VOID AND DISLOCATION STRUCTURES IN FE-CR BINARY ALLDYS IRRADIATED IN FFTF TO 15 DPA AT 430°C

	SWELLING			DISLOCATIONS			
				a <100> Loops - Dislocations			α/2 <111> Dislocations
Alloy	ΔV/V (%)	d (nm)	Density (#/cm^3)	d (nm)	Number Density (#/cm^3)	Line Length (cm/cm^3)	Line Length (cm/cm^3)
Fe-3Cr	0.007	8.6	2.0×10^{14}	19.6	1.6×10^{15}*	9.9×10^{9}	1.3×10^{9}*
Fe-6Cr	0.147	12.2	1.7×10^{15}	18.4	6.2×10^{15}	3.6×10^{10}	8.7×10^{9}
Fe-9Cr	0.254	16.9	1.2×10^{15}	N.M.	N.M.	9.6 x 109	1.0×10^{10}
Fe-12Cr	0.106	10.8	1.8×10^{15}	18.9	4.9×10^{15}	4.2×10^{10}	5.0×10^{9}
Fe-15Cr	0.060	8.7	2.3×10^{15}	19.2	3.1×10^{15}	1.9×10^{10}	3.2×10^{9}
Fe-18Cr	0.087	8.9	3.1×10^{15}	16.1	1.9×10^{15}	2.0×10^{10}	7.9×10^{9}

*Nan-uniformly distributed

N.M. - Not Measured

NUCLEATION OF GRAIN BOUNDARY CAVITIES UNDER THE COMBINED INFLUENCE OF HELIUM AND APPLIED STRESS

J. N. Al-Hajji (University of Kuwait) and N. M. Ghoniem (University of California, Los Angeles)

1.0 Objective

The objective of this aspect of the program is to develop theoretical understanding of the speed and magnitude of grain boundary cavity nucleation under fusion conditions. The influence of the combination of stress and high helium production on nucleation kinetics is theoretically studied. This mechanistic understanding may provide a basis for tailoring materials to mitigate helium embrittlement at high temperatures.

2.0 Summary

Modeling cavity nucleation at grain boundaries in structural alloys under the combined influence of helium and stress is the primary objective of this paper. The role of stress in cavity nucleation is analyzed by using classical nucleation theory, taking into account grain boundary sliding to describe stress concentration buildup and relaxation at particles and triple-point junctions. Helium clustering in the matrix is modeled using rate theory. The helium flux to grain boundaries is determined by the application of sink strength theory which takes into account the various competing clustering mechanisms in the matrix. Helium clustering on grain boundaries is also modeled. The work confirms theoretical observations that irradiation results in grain boundary bubble densities which are orders of magnitude larger than cavity populations observed in conventional creep experiments. It is shown that even if the total injected helium is as little as one part per million, it can result in grain boundary hubhle densities on the order of 10^9 cm^{-2}. Such cavity population exceeds typical grain boundary cavity densities associated with creep experiments. Grain boundary bubble densities are shown to reach steady state for injected helium amounts on the order of 10 parts per million.

3.0 Program

Title: Radiation Effects on Structural Materials
Principal Investigator: N. M. Ghoniem
Affiliation: University of California at Los Angeles (This work was performed as a part of Dr. Ai-Hajji's Ph.D. dissertation at UCLA.)

4.0 Relevant DAFS Program Plan Task/Subtask

Suhtask C Correlation Methodology

5.0 Accomplishments and Status

5.1 Introduction

Over the past decade, a numher of theoretical and experimental investigations have addressed the question of cavity nucleation at grain boundaries [1-10]. For example, Raj and Ashhy C41 developed a kinetic model of classical heterogeneous nucleation by vacancy clustering at interfaces hetween precipitate particles and grain boundaries. Their work revealed that cavity nucleation is in fact stress controlled. However, under irradiation at high temperatures, it has heen observed [10-15] that the population of voids at grain boundaries is typically 4 to 5 orders of magnitude higher than unirradiated creep-tested specimens. This has been attributed to the presence of helium at such boundaries. The distinction between cavity nucleation by helium versus stress has to be made.

In the present paper, theoretical investigation of cavity nucleation at the grain hounrlary under the influence of stress and helium is given. The stress-controlled mode of cavity nucleation is analyzed by using classical nucleation theory, taking into account the role of sliding in generating highly localized stress concentrations at boundary irregularities and triple-point junctions. The heliurn-controlled mode of cavity nucleation is modeled by using rate theory to describe the clustering of helium atoms at grain houndaries into stable nuclei.

5.2 Stress-Controlled Nucleation of Cavities

At elevated temperatures of $\sim 0.6\ T_m$ and medium applied stresses of $\sim 10^{-3}$ G (G is the shear modulus), grain houndary cavities are nucleated hy diffusional transfer of atoms from grain boundary precipitate surfaces into the grain houndary. This results in the formation of a vacancy cluster which is large enough to overcom? the shrinkage tendency under the action of surface energy forces. The local tensile traction plays a considerable role in aiding cavity emhryos to grow through a size range where growth is energetically unstable.

Classical nucleation theory indicates that the nucleation rate C (the product of the number of nuclei at the critical size, the probability that a vacancy will he added to a critical nucleus, and the Zeldovich factor which takes into account thermal fluctuations hetween the subcritical and supercritical regimes) is given hy [16]

$$\dot{C} = C_{max}\left(\frac{\pi}{12 F_v \gamma_s^3 kT}\right)^{1/2} \sigma_L^2 D_b \Delta \exp\left(-\frac{\Delta G_c}{kT}\right) , \tag{1}$$

where C_{max} is the maximum number of available nucleation sites per unit area of grain houndary, F_v is the volumetric shape factor, γ_s is the cavity surface energy, k is Boltzmann's constant, T is the temperature, Δ is the boundary thickness, σ_L is the local stress, D_b is the grain boundary diffusivity, ΔG_c is the change in the free energy due to the introduction of cavities on a stressed boundary and it is given by

$$\Delta G_c = 4\gamma_s^3 F_v/\sigma_L^2 , \tag{2a}$$

or

$$\Delta G_c = v_c^3 F_v \sigma_L/2 , \tag{2b}$$

where $r_c = 2\gamma_s/\sigma_L$. Equation (1) does not account for the fact that once a cavity is nucleated, its site is no longer available for any additional nucleation. An additional probabilistic factor needs to he included to account for the decreasing number of available nucleation sites. This is given hy

$$P_s = \frac{C_{max} - C}{C_{max}} . \tag{3}$$

Including Eq. (3) into Eq. (1) gives

$$\dot{C} = (C_{max} - C)\left[\left(\frac{\pi}{12F_v\gamma_s^3 kT}\right)^{1/2} \sigma_L^2 D_b \Delta \exp\left(-\frac{\Delta G_c}{kT}\right)\right] . \tag{4}$$

If we denote all terms within the large brackets by A(t), then we can rewrite Eq. (4) as

$$\frac{dC}{dt} = (C_{max} - C)A(t) . \tag{5}$$

The term A(t) is strongly time dependent since the local stress is a complex function of time as it is influenced by the diffusional flow of matter. Equation (5) is subject to the initial condition that at t = 0, C = 0.

Solving Eq. (5) results in

$$C = C_{max}[1 - e^{-\int A(t)dt}] \quad . \tag{6}$$

Cavity nucleation calculations are carried out using the complex time dependence of the local stress.

Inspecting Eq. (4), we notice two values which have been the center of controversy, σ_L and F_v. Typical stresses necessary for nucleation are found to be about 30 times greater than applied stresses [17]. However, such high stress concentrations may be reached due to the instantaneous stress relaxation by diffusional flow of matter [1]. It has also been argued [1,4] that cavities assume thin, crack-type shapes. Such shapes help cavities reach equilibrium without the need for the existance of stress concentrations.

Examining the behavior of ΔG_c for a shape factor of 0.01 and a typical surface energy of 2 J/m^2 shows that even in the presence of a relatively high local stress, the barrier to nucleation is high (22.13 eV for an applied stress of 300 MPa). This corresponds to a diminishing value for the nucleation rate. If we examine Eqs. (2a) and (2b) they show that there are two possible ways to reduce the energy barrier to nucleation: (1) the cavities must be extremely thin (reducing F_v), and/or (2) the local stress has to reach extremely high values. It can be shown that if the local stress is 100 MPa, the shape factor should he in the neighborhood of 10^{-4}; otherwise nucleation will be impossible. Such extreme values of F_v have been suggested hy Reidel [1] and Raj and Ashby [4]. The other possibility is that stress concentrations have to be present at inclusions and triple points in order for cavity nucleation to proceed [8,10,18]. The critical free energy for cavity formation varies significantly as a function of the local stress ($\Delta G_c \sim \sigma_L^{-2}$). It is concluded that a stress concentration mechanism has to be present in order to make nucleation possinle (typical engineering stresses under creep are ~ 100 to 200 MPa). The shape factor value of about 0.01 has heen adopted as reasonahle hy many investigators [4,19]. However, other investigators [20] asserted that F_v has a value of ~ 0.3 according to their experimental observations. This shows an uncertainty in the actual value of F_v. The next section deals with stress concentration evolution at preferred sites at the grain boundaries. This will then he followed by nucleation calculations which incorporate stress concentration factors for various possihle shape factors.

5.2.1 Stress Concentration at Particles and Triple-Point Junctions

At high temperatures, the shearing resistance of grain boundaries is apparently less than the shearing resistance of individual grains themselves (e.g., Ref. 21). However, if particles are present at sliding grain boundaries, stress concentrations approaching the ideal cohesive strength limit will be present at particle faces. This has been shown by Lau [22] and also by [1]. This can be readily seen by a simple force balance of a particle on a sliding boundary. Let us denote the particle spacing as L and its diameter as P located on a boundary. A shear stress τ will then give a localized particle facial stress of $\sigma_P = 2(L/P)^2$. Such a particle stress is quite substantial and can explain the fact that obstacles at sliding boundaries are preferential sites for cavity nucleation. Reidel's calculations [1] show that in the absence of any diffusional flow, the average stress on the particle is on the order of $\sigma_P \simeq \tau(L/P)^2$.

C. W. Lau [22] made calculations of the stress-concentration factors associated with grain houndary inclusions and triple-point junctions in a power-law creeping material using the finite element technique. His work shows that a singularity develops at the triple-point junction (Fig. 1) which is of the form

$$\sigma_{\theta\theta} = K_{TPJ}/x^{\lambda_{TPJ}} \quad . \tag{7}$$

For a creep exponent of m = 1, it is shown [22] that

$$\sigma_{\theta\theta}/\sigma_\infty = 0.3(d/x)^{0.449} \quad . \tag{8}$$

Lau's Solution [22] of the stress distribution around triple-point junctions shows resemblance to the solution of the tensile-stress concentration of a single-mode-I1 penny-shaped crack loaded by the shear stress $\sigma_\infty/2$. The penny-shaped-crack problem has been adopted by Evans, Rice and Hirth [5] to study the time-dependent behavior of the stress singularity at triple-point junctions.

5.2.2 Stress Buildup and Relaxation at Particles

The simplest description of stress loading and unloading is provided by a phenomenological visco-elastic model which yields an expression given by [23,24]

$$\sigma_p(t) = (\tau_o - \tau^*) \exp(-t/\tau_L) + (\tau^* - \tau_\infty) \exp(-t/\tau_R) + \tau_\infty \quad , \tag{9}$$

where τ_L and τ_R represent the loading and relaxation times, respectively. For all practical purposes

$$\tau_\infty = \tau o = \sigma applied/2 \ , \tag{10}$$

and

$$\tau^* = \tau_o/f \quad , \tag{11}$$

where

$$f = (P/L)^2 \quad . \tag{12}$$

f is the fractional area of the boundary occupied by particles; τ_R, which is volume/grain boundary diffusion controlled, *is* the shortest relaxation time for smoothing out the singularity.

The characteristic time for stress loading at particles is given as [6]

$$\tau_{BR} = \tau_L = \frac{\eta L}{\pi G \Delta} \beta(P/L) \quad , \tag{13}$$

where η is the boundary viscosity which is given hy Ashby [25] as

$$\eta = \frac{kT}{8\Delta D_b} \quad , \tag{14}$$

and

$$\beta(P/L) = \cosh^{-1}\{1/[\cos(\pi/2)](1-P/L)\} \quad , \tag{15}$$

β accounts for the interactions of inter-particle planar segments on the grain boundary.

The characteristic time for boundary diffusional relaxation of the stress concentration at particles is given in the literature by Koeller and Raj [26]. For very rigid particles the relaxation time is given **by:**

$$\tau_{R,BDIFF} \simeq \frac{L^3 kT}{G \Delta D_b \Omega} \tag{16}$$

Now if we use the usual criteria for a changeover from boundary to volume diffusion ($D_b \Delta + LD_v$) [27], we ohtain

$$\tau_{R,VDIFF} \simeq \frac{L^2 kT}{G D_v \Omega} \quad . \tag{17}$$

5.2.3 Stress Loading and Relaxation at Grain Boundary Particles and Triple-Point Junctions

When a stress is suddenly applied to polycrystaline solids at elevated temperature, instantaneous homogeneous elastic deformation sets in. The resolved shear stress at the grain boundary interfaces are relaxed by sliding, which results in stress concentrations at grain boundary irregularities such as interface particles. However, diffusional transfer of matter from these sites leads to relaxation of the high localized stress. This results in a gradual buildup of a stress concentration at irregularities of a larger spatial scale (i.e., a gradual buildup of stress concentration at triple-point junctions). The Evans, Rice and Hirth solution [5] of the timedependent behavior of the stress singularity at triple-point junctions yields

$$\sigma(0,t) = \frac{1}{9}\,\sigma_\infty(\tau_R^{TPJ}/t)^{1/6} \quad , \tag{18}$$

where

$$\tau_R^{TPJ} = \frac{(1-\nu)kTd^3}{G\,D_b\,\Delta\Omega} \tag{19}$$

is a characteristic stress relaxation time constant. Equation (18) describes the stress relaxation in the vicinity of triple-point junctions. However, this expression does not take into account any loading time. Following Yoo and Trinkaus [23], a characteristic exponential loading time can he introduced into the Evans et al. model to describe the overall time hehavior of the stress at triple-point junctions. The following expression results for the normal stress at the intersection

$$\sigma_{TPJ} = \sigma_\infty\left\{1 + \left[1 - \exp\left(-\frac{t}{\tau_L^{TPJ}}\right)\right]\frac{1}{9}\left(\frac{\tau_R^{TPJ}}{t}\right)^{1/6}\right\} \quad . \tag{20}$$

In this expression, τ_L^{TPJ} represents a characteristic loading time of stress at triple-point junctions and is determined by the overall intrinsic viscosity of the boundary, including the effect of particles at the boundary [24]

$$\tau_L^{TPJ} = \frac{d}{50G}\,\frac{kT}{\Omega}\,\frac{P^4}{L^2}\,\frac{1}{\Delta\,D_b}$$

5.3 Theory of Helium Transport and Clustering at Grain Boundaries

When helium atoms are introduced into a solid, either by implantation or by nuclear reactions, they tend to be insoluble. Like other noble gases, the closed electronic structure of helium results in segregation. Because of this insolubility, there is a great tendency for helium atoms to he trapped on vacancies, impurity atoms, or other helium atoms [28-40]. The transport of helium to grain boundaries is primarily by migration of single gas atoms through the matrix [40] which is naturally influenced by competing clustering processes. Helium atoms, which migrate predominantly by an interstitial mechanism, can be trapped at precipitate interfaces, vacancies, or in helium-vacancy clusters (HVCs). A rate theory model has heen developed to study helium migration from the matrix to the grain boundary. While details of the model have been published elsewhere [41], a brief summary will be presented here for the sake of self-consistency.

In this matrix transport/clustering model [41], appropriate rate equations were given for the following species: (1) unoccupied vacancies, (2) self-interstitial atoms, (3) interstitial helium atoms, (4) substitutional helium atoms, (5) di-interstitial helium atom clusters, (6) di-helium single-vacancy clusters, (7) buhble nuclei containing three helium atoms, and (8) large bubbles containing m helium atoms. Equations for the average bubble size, the average number of helium atoms in a bubble, and the amount of helium absorbed on grain boundaries were also developed. It is also assumed that one helium buhble is associated with each precipitate. Therefore, an equation describing the average precipitate bubble radius and another equation for the average number of helium atoms in a bubble were included. A key equation was developed to account for single interstitial helium atoms escaping the competing matrix processes until trapped at the grain boundary. This was adopted as the sole source of helium at the grain boundary. Localized helium sources such as boron were not included, but an additional equation can easily he included to account for such grain boundary helium sources.

Helium production at the grain houndary is primarily due to single interstitial helium atoms escaping the interior grain traps. Bubble mobility has been considered and was shown to have a negligible effect on helium transport to grain houndaries [24]. Bubble mobility has been considered and was shown to have a negligihle effect on helium transport to grain boundaries [24]. Since interior grain traps change with irradiation, the production of helium at the grain houndary is time dependent. Vacancies at grain boundaries are assumed to be readily available to trap helium interstitials. When this is formed on the grain boundary, it can accept newly arrived gas atoms to form higher order clusters on the grain boundary. Once a tri-helium cluster is' formed-with some-vacancies (number need not be determined), a bubble embryo is formed on the grain boundaries.

In this section, four equations are developed for the following species: (1) single helium atoms C_g^{gb}, (2) di-helium atomic clusters (also a bubble nucleus) containing two helium atoms C_{2g}^{gb}, and (3) large bubbles containing m helium atoms C_b^{gb}. An equation that describes the average number of helium atoms in a buhble is also presented.

1. Single Helium Atoms Concentration

$$\frac{dC_g^{gb}}{dt} = Q_{gb} - 2R_{g,g}^{gb}\, C_g^{gb^2} - R_{g,2g}^{gb}\, C_g^{gb}\, C_{2g}^{gb} - R_{g,b}^{gb}\, C_g^{gb}\, C_b^{gb} - bKC_g^{gb} - R_{g,bppt}^{gb}\, C_g^{gb}\, C_{bppt}^{gb} \quad . \tag{22}$$

2. Di-Helium Cluster Concentration

$$\frac{dC_{2g}^{gb}}{dt} = R_{g,g}^{gb}\, C_g^{gb^2} - 2bKC_{2g}^{gb} - R_{g,2g}^{gb}\, C_g^{gb}\, C_{2g}^{gb} \quad . \tag{23}$$

3. Grain Boundary Buhble Concentration

$$\frac{dC_b^{gb}}{dt} = \frac{3}{m_b^{gb}}\, R_{g,2g}^{gb}\, C_g^{gb}\, C_{2g}^{gb} \quad . \tag{24}$$

4. Average Number of Gas Atoms in a Bubble

$$\frac{dm_b^{gb}}{dt} = R_{g,b}^{gb}\, K_g^{gb} - bKm_b^{gb} \quad . \tag{25}$$

We now introduce a hasic frequency to describe the clustering rates at the grain boundary. α can he defined as:

$$\alpha = 48\, \nu_a^{gb} \exp\left(- \frac{He}{kT}\right. \tag{26}$$

The combinatorial factor for bubbles at the grain boundary is described in the same way as in the matrix [41]; that is,

$$\varepsilon = \frac{4\pi}{48} \left(\frac{R}{a}\right) \quad . \tag{27}$$

With the reaction frequency α and the combinatorial number ε, the gas reaction rates at grain boundaries are given by

$$R^{gb}_{9.9} = 2\alpha \quad , \tag{28}$$

$$R^{gb}_{g,2g} = 2\alpha \quad , \tag{29}$$

$$R^{gb}_{g,b} = \varepsilon_{GB}\alpha \quad . \tag{30}$$

Now the previous set of equations can be re-written in the following form:

$$\frac{dC^{gb}_g}{dt} = Q_{gb} - 4\alpha C^{gb^2}_g - 4\alpha C^{gb}_g C^{gb}_{2g} - \varepsilon_{GB}\,\alpha C^{gb}_g C^{gb}_b - \varepsilon^{ppt}_{GB}\,\alpha C^{gb}_g C^{gb}_{bppt} - bKC^{gb}_g \quad , \tag{31}$$

$$\frac{dC^{gb}_{2g}}{dt} = 2\alpha C^{gb^2}_g - 2\alpha C^{gb}_g C^{gb}_{2g} - 2bKC^{gb}_g \quad , \tag{32}$$

$$\frac{dC^{gb}_r}{dt} = \frac{6a}{m_b} C^{gb}_g C^{gb}_{79} \quad , \tag{33}$$

$$\frac{dm^{gb}_g}{dt} = \varepsilon_{GB}\,\alpha C^{gb}_g - bKm^{gb}_b \quad . \tag{34}$$

Equation (31) represents the rate of change of single-helium atom concentration at grain boundaries, C^{gb}_g. The source of helium Q_{gb}, which is supplied by helium transport through the matrix. is balanced by the formation of helium clusters, by absorption at newly formed bubbles, by precipitates. or by radiation re-solution back into the matrix. Equation (32) describes the rate of change of di-helium clusters while Eq. (33) is for the nucleation rate of helium-filled cavities at grain boundaries. The last equation [Eq. (34)] determines the rate of change of the average number of helium atoms in a cavity m^{gb}_g, due to the balance between the absorption rate, $\varepsilon_{GB}\alpha C^{gb}_g$, and radiation re-solution at the rate bKm^{gb}_b. Obviously this set of equations has to be solved self-consistently with the corresponding set representing matrix processes; the coupling rate being Q_{gb}. For details, the reader is referred to Ref. [41].

5.4 Results of Calculations for Stress-Controlled Cavity Nucleation

Figure 2 shows that the overall time dependence of stress evolution at triple-point junctions is much slower than that at particle interfaces. This is because the time dependence of the stress concentration at triple-point junctions is characterized by a wide spectrum of relaxation times, i.e., short relaxation times controlling the early stages and long ones controlling the later stages [5]. This is in contrast with stress relaxation times of particles in which diffusional matter flow needs only to occur over short distances in order to relieve the stress. This figure also shows that the duration of the stress pulse becomes quite short at higher temperatures. At lower temperatures, the triple-point-junction stress becomes quite persistent for a reasonably long time. This may explain observed triple-point cracking at temperatures below about 400°C [42], since persistent stress concentration at triple-point junctions leads to crack initiation. Stress pulses shown in Fig. 2 are used later in nucleation calculations.

It has been experimentally observed (e.g., [7]) that high temperature fracture occurs due to the nucleation and growth of cavities along grain boundaries which are most perpendicular to the applied stress. However, two experimental studies directed toward understanding cavity nucleation at high temperatures (Dyson, Loveday and Rcdgers [43], and Kikuchi, Shiozawa and Weertman [44]) showed the surprising result that most nucleated cavities have formed on grain boundaries which are parallel to the maximum principal stress axis. However, the experiment by Dyson et al. [43] also showed that preferential cavity growth occurred during subsequent tensile creep. Those cavities on parallel boundaries either remained constant in size or diminished, while those on boundaries which were orthogonal to the applied stress axis grew relatively quickly. This behavior of cavity growth can be misleading in the sense that it can be mistaken for preferential nucleation on orthogonal boundaries to the applied stress and subsequent fracture along these boundaries. In essence, inclined boundaries tend to host the majority of the cavity nuclei population, while orthogonal boundaries host a small fraction of the population. However, the cavity population on orthogonal houndaries tends to experience preferential growth during the course of the creep test until fracture. Chen and Argon [7] have experimentally observed a $(\sin a)^2$-type distribution for large cavities, where a is the angle between the boundary normal and the applied stress.

Stress concentrations at particles present on orthogonal boundaries, created by the difference in rigidity between the particles and the matrix [45], are not significant to produce reasonable nucleation rates. A localized grain boundary sliding has to be present on orthogonal boundaries which will result in a localized high stress concentration at particles. Grain boundaries are hardly ever flat. This has been asserted hy Rshhy [25]. When the boundary is stressed, a certain degree of sliding occurs until a particle is encountered which gives rise to a fairly high stress concentration. This process of localized sliding should occur in principle throughout the creep test in response to various deformation processes such as unpinning of grain boundaries, triple-point cracking, stress relaxation in neighboring sliding regions, triple-point migration, etc. [46].

In order to model nucleation at orthogonal boundaries which exhibit localized irregularities, it is assumed that a boundary exhibits localized sliding due to deviations from orthogonality by about 10 to 20 deg. Figure 3 shows that the nucleation rate is the highest along boundaries which are parallel to the applied stress and decreases sharply as houndaries tend toward orthogonality. At orthogonal flat boundaries, nucleation is essentially nonexistant. The nucleation pulse closely follows the stress pulse behavior; the nucleation pulse is terminated once the stress pulse has elapsed. At 600°C. the nucleation pulse lasts ~ 100 sec. If the nucleation rate is high, all possible nucleation sites will be filled up by cavities. If the nucleation rate is low, cavity nucleation will occur throughout the creep experiment following the course of stress concentration buildup and relaxation in response to localized sliding which should occur intermittently.

Figure 4 shows that nucleation is virtually impossible for large volumetric shape factors ($F_v > 0.02$). This is consistent with the idea that cavities possess a lenticular rather than a spherical shape during the course of nucleation. The figure also illustrates that the actual value of F_v may be constrained by the limit $0.01 < F_v < 0.001$, for consistency with experimental ohservations.

It is very important to examine the temperature dependence of the nucleation process (see Fig. 5). This figure shows that the nucleation rate is the highest at 700°C and decreases as the temperature decreases. The behavior actually translates into more extensive nucleation at higher temperatures. This is consistent with the experimental observations presented hy Argon et al. [6]. The figure also shows another important result: the duration of the nucleation pulse is sharply curtailed at high temperatures. The basic reason for this behavior is that stress relaxation is faster at high temperatures due to the more extensive atom motion. At lower temperatures, the duration of the stress pulse is long. However, the nucleation rate is too low to produce significant cavitation. The low cavitation at lower temperatures can he linked to the high thermal barrier to nucleation at lower temperatures.

Experimental observations by Chen and Argon [7] show that more extensive nucleation occurs near triple-point junctions. As was shown in the previous section, high stress concentration exists at triple-point junctions and prevails for a relatively long period of time. This stress results in an enhanced sliding rate past grain boundary irregularities and in high stress concentrations at neighboring particles. The relaxation of stress concentration at neighboring particles is part of the relaxation process of the triple-point stress concentration. The relaxation of the triple-point stress concentration is a very slow one which can be attributed simply to the large distance over which uniform atom plating has to occur. Figure 6 shows that the neighborhood of a triple-point junction suffers more extensive cavitation. This is also consistant with results presented in the literature [7]. If we examine Fig. 2 again, it shows that at a temperature which is too low to result in any significant nucleation (~ 400°C), the triple-point stress concentration prevails for an extensive period of time and can result in the opening of a crack at the triple point by decohesion. One can conclude that triple-point cracking can he due to decohesion at lower temperatures; hut at higher temperatures, cavitation near the triple point plays a major role in opening such a crack.

5.5 Results of Calculations of Helium-Controlled Cavity Nucleation

The rate of clustering of helium at grain boundaries is influenced mainly by the effective migration energy of single helium atoms. The effective migration energy of helium in the matrix has heen studied in detail hy Ghoniem et al. [40]. However, very little is known about its value at grain boundaries.

It is generally believed that helium atoms introduced at grain boundaries reside in a substitutional position since the supply of vacancies at grain boundaries is nearly inexhaustible. Figure 7 illustrates the sensitivity of the effective helium migration energy on the grain boundary bubble density. The irradiation conditions simulated in the figure are that of dual ion-beam irradiation which are conducted at 625°C on type 316 stainless steel. The displacement rate is 3×10^{-3} dpa/s and the helium to dpa ratio is 5. Increasing the effective migration energy results in enhanced nucleation. A migration energy of 1.5 to 2.0 eV results in a bubble density consistent with those observed experimentally [11-15].

Figure 8 is intended to simulate the grain boundary bubble nucleation experiment conducted by Lane and Goodhew [15]. It shows the bubble density as a function of implantation rate. The experiments were carried out at 600°C with a helium to dpa ratio of 1.6 × 10^4 (appm/dpa). The figure clearly demonstrates that the bubble density increases with an increasing implantation rate. The model successfully shows the correct trends as those observed experimentally. The figure also illustrates that increasing the grain boundary helium migration energy enhances the nucleation of bubbles.

Figure 9 simulates a recent grain boundary bubble nucleation experiment conducted by Batfalsky and Schroeder [12]. The helium to dpa ratio is 10^4 (appm/dpa). The helium implantation rate is 100 appm/hr at 750°C. The simulation shows that the effective migration energy is approximately the same as that for self-diffusion. A selfdiffusion energy of 1.9 eV has been reported by Smith and Gibbs [47]. The figure also shows that the helium clustering rate is extremely large in the beginning of irradiation and it slows down as the amount of helium arriving at the grain boundary balances that which leaves it by radiation resolution.

5.6 Conclusions

1. Classical nucleation theory can be used to study the timedependent nucleation of creep. On the other hand, rate theory can be successfully used to describe helium-controlled cavitation in the presence of irradiation.
2. Even if the total injected helium is as little as one appm, it can result in a grain boundary bubble density as high as 10^9 cm^{-2}. Such cavity population exceeds typical grain boundary precipitate densities which are actually an upper limit of stress-controlled cavity nucleation.
3. The effective migration energy of helium at grain boundaries is approximately that of selfdiffusion.
4. The models confirm experimental observations that the bubble density due to irradiation is orders of magnitude larger than the cavity population observed in creep experiments in the absence of irradiation.
5. Grain boundary sliding and obstacles at sliding boundaries (e.g., particles and ledges) are basic ingredients of stress-controlled creep cavity nucleation. In their absence this mode of cavity nucleation is virtually impossible. Helium-controlled grain houndary cavity nucleation, however, is insensitive to grain houndary sliding and stress evolution.
6. Stress-controlled cavity nucleation is most probable on those houndaries which are parallel to the maximum principal stress axis and least probable on orthogonal boundaries. Helium-controlled nucleation, however, is not affected by the boundary orientation to the applied stress.
7. Both stress- and helium-controlled cavity nucleations are quite fast and are not rate controlling in the determination of the lifetime of irradiated structural alloys at high temperature.
8. Stress-controlled cavity nucleation rate at triple-point junctions is higher than that for those regions which are far away from triple points. 'Helium-controlled nucleation is not affected hy the proximity to triple-point junctions.
9. Hioher helium implantation rates result in a hiqher grain boundary cavity density, even though the total amount of helium injected remains constant.
10. The grain boundary bubble density reaches a steady state at injected helium amounts on the order of 10 appm.

6.0 Acknowledgements

This work is partially supported by the U.S. Department of Energy, Grant No. DE-FG03-84ER52110 with UCLA. One of us (JNA) is grateful to Kuwait University for financial support during his graduate study at UCLA.

7.0 Nomenclature

Symbol	Description	Units
b	Re-solution parameter	
$\dot{C}$	Stress controlled nucleation rate	(m^{-2}/s)
C_b^{gb}	Grain boundary bubble concentration	(at./at.)
C_g^{gb}	Single-helium atom concentration (at grain boundary)	(at./at.)
C_{2g}^{gb}	Di-helium complex concentration (at grain boundary)	(at./at.)
C_{max}	Grain boundary precipitate density	(m^{-2})
D_b	Grain boundary self-diffusion coefficient	(m^2/s)
D_v	Vacancy self diffusion coefficient	(m^2/s)
d	Grain diameter	(m)
E_{He}^{gb}	Effective grain boundary helium migration energy	(eV)
F_v	Volumetric shape factor	
G	Shear modulus	(MPa)
k	Boltzmann's constant	(eV/°K)
K	Displacement damage rate	(at./at./s)
L	Inter-precipitate spacing	(m)
m_b^{gb}	Average number of gas atoms in a bubble	
P	Precipitate diameter	(m)
Q_{gb}	Grain boundary helium flux	(at./at./s)
$R_{g,b}^{gb}$	Reaction rate between single helium and bubbles	(1/s)
$R_{g,g}^{gb}$	Reaction rate between single helium atoms	(1/s)
$R_{g,2g}^{gb}$	Reaction rate between single and di-helium clusters	(1/s)
T	Temperature	(°K)
t	Time	(s)
x	Distance measured from singularity tip	(m)
α	Frequency factor	(1/s)
γ_s	Bubble surface energy	(J/m^2)
ΔG_c	Critical free energy for cavity formation	(eV)
δ	Re-solution frequency	(1/s)
Δ	Effective width of the grain boundary	(m)
ε_{GB}	Diffusion-controlled combinatorial factor for bubbles	(1/s)
η	Grain boundary viscosity	$(eV/m^3/s)$
λ_{TPJ}	Range exponent dependent on the creep exponent	
ν	Poisson's ratio	
ν_{gb}	Helium vibration frequency	(1/s)
σ_L	Local stress	(MPa)
σ_P	Accentuated stress at the particle face	(MPa)
σ_∞	Applied stress	(MPa)
τ_L	Characteristic loading time	(s)
τ_R	Characteristic relaxation time	(s)

8.0 References

[1] H. Reidel, Acta metall. 32, 313 (1984).
[2] A. S. Argon, Scripta metall. 17, 5 (1983).
[3] R. Raj, Acta metall. 26, 995 (1978).
[4] R. Raj and M. F. Ashby, Acta metall. 23, 653 (1975).
[5] A. G. Evans, J. R. Rice and J. P. Hirth, J. Am. Ceram. Soc. 63 (7-8), 368 (1980).
[6] A. S. Argon, I. W. Chen and C. W. Lau, in Creep-Fatigue-Environment Interactions (edited by R. M. Pelloux and N. S. Stoloff), p. 46. A.I.M.E., New York (1980).
[7] I. W. Chen and A. S. Argon, Acta metall. 29, 1321 (1981).
[8] W. Pavinich and R. Raj, Metall. Trans. A 8A, 1917 (1977).
[9] I. Servi and N. J. Grant, Trans. A.I.M.E. 191, 909 (1951).
[10] J. E. Harris, Trans. Metall. Soc. A.I.M.E. 233, 1509 (1965).
[11] A. F. Rowcliffe, G. J. C. Carpenter, H. F. Merrick and R. B. Nicholson, Effects of Radiation on Structural Metals, ASTM STP-426, pp. 161-199. A.S.T.M. (1967).
[12] P. Batfalsky and H. Schroeder, J. Nucl. Mater. 122&123, 1475 (1984).
[13] J. I. Bennetch and W. A. Jesser, J. Nucl. Mater. 103&104, 809 (1981).
[14] P. L. Lane, J. H. Evans and P. J. Goodhew, J. Nucl. Mater. 120, 342 (1984).
[15] P. L. Lane and P. J. Goodhew, Philos. Mag. (A) 48, 965 (1983).
[16] M. H. Yoo and H. Trinkaus, Metall. Trans. A 14A, 547 (1983).
[17] A. S. Argon, Recent Advances in Creep and Fracture of Engineering Materials and Structures (edited by B. Wilshire and D. R. J. Owen), pp. 1-52. Pineridge Press, Swansea (1982).
[18] F. W. Crossman and M. F. Ashby, ibid., Ref. [4], p. 425.
[19] H. Trinkaus and H. Ullmaier, Philos. Mag. 39, 563 (1979).
[20] A. L. Chang and M. L. Bleiberg, Ward Topical Report WARD-AD-3045-12, 259 (1980).
[21] C. Zener, p. 3. Presented Fracturing of Metals Seminar, American Society for Metals, Chicago (1948).
[22] C. W. Lau, Ph.D. Thesis, Massachusetts Institute of Technology (1981).
[23] H. Trinkaus, private communication.
[24] J. N. Alhajji, UCLA Report UCLA-ENG-8533, PPG-894, Los Angeles (1985).
[25] M. F. Ashby, Surface Sci. 31, 498 (1972).
[26] R. C. Koeller and R. Raj, ibid., Ref. [3], p. 1551.
[27] R. Raj and M. F. Ashby, Metall. Trans. A 2A, 1113 (1971).
[28] M. I. Baskes, C. L. Bisson and W. D. Wilson, J. Nucl. Mater. 83, 139 (1979).
[29] G. Carter, D. G. Armour, S. E. Donnelly, D. C. Ingram and R. P. Webb, p. 83. Presented at Harwell Consultants Symposium, Oxfordshire, England (October 1979).
[30] G. Farrell and W. A. Grant, Radiat. Eff. 3, 249 (1970).
[31] R. H. J. Fastenau, A. van Veen, P. Penning and L. M. Caspers, Phys. status solidi (A) 47, 577 (1978).
[32] J. E. Inglesfield and J. B. Pendry, Philos. Mag. 34 (2), 205 (1976).
[33] D. L. Johnson and J. R. Cost, in Defects and Defect Clusters in B.C.C. Metals and their Alloys, Proc. of National Bureau of Standards Conf., p. 279. Gathersburg, MD (August 1973).
[34] G. R. Odette, P. J. Maziasz and J. A. Spitznagel, ibid., Ref. [13], p 1289.
[35] D. B. Poker and J. M. Williams, Appl. Phys. Lett. 40, 851 (1982).
[36] J. Roth, S. T. Picraux, W. Eckstein, J. Bottiger and R. Behrisch, J. Nucl. Mater. 63, 120 (1976).
[37] W. Schilling, Yamada V Conf. on Point Defects Tokyo, Japan (Oct. 1981).
[38] F. A. Smidt, Jr. and A. G. Pieper, in Properties of Reactor Structural Alloys After Neutron or Particle Irradiation, Proc. of A.S.T.M. Conf. Gatlinburg, TN (June 1974), p. 352. ASTM-STP-570.
[39] W. D. Wilson and C. L. Bisson, Radiat. Eff. 22, 63 (1974).
[40] N. M. Ghoniem, S. Sharafat, J. M. Williams and L. K. Mansur, J. Nucl. Mater. 117, 96 (1983).
[41] N. M. Ghoniem, J. N. Alhajji and D. Kaletta, to be published J. Nucl. Mater. (1985).
[42] A. Evans, Acta metall. 28, 1155 (1980).
[43] B. F. Dyson, M. S. Loveday and M. J. Rodgers, Proc. R. Soc. London, Ser. A 349, 245 (1976).
[44] M. Kikuchi, K. Shiozawa and J. R. Weertman, Acta metall. 29, 1747 (1981).
[45] J. N. Goodier, J. Appl. Mech. 55, 39 (1933).
[46] N. J. Grant and A. W. Mullendore, Eds. Deformation and Fracture at Elevated Temperatures M.I.T. Press, Cambridge, MA (1965).
[47] A. F. Smith and G. B. Gibbs, Met. Sci. J. 2, 47 (1968).

9.0 Future Work

Work will continue to develop a comprehensive model for helium ernbrittlement and compare with experiments.

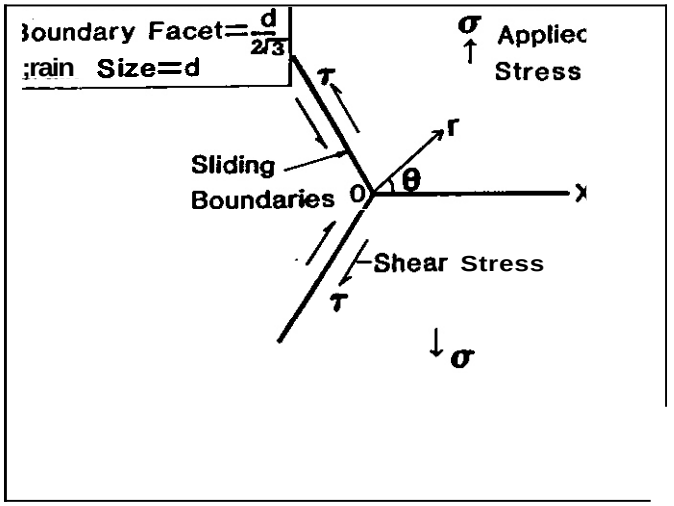

FIGURE 1. Idealization of a triple-point junction.

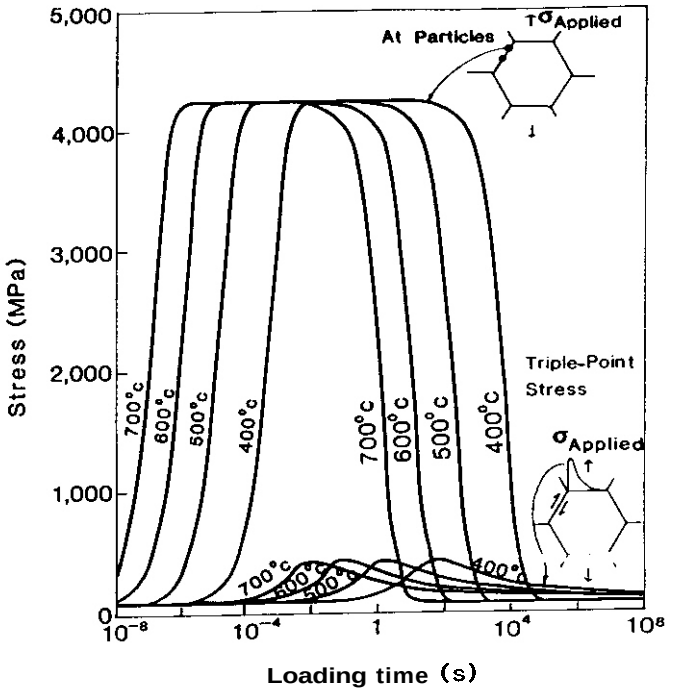

FIGURE 2. Stress loading and relaxation at particles and triple-point junctions for an applied stress of 100 MPa, a grain size of 50 μm, a particle size of 0.3 μm, and spacing of 0.21 μm.

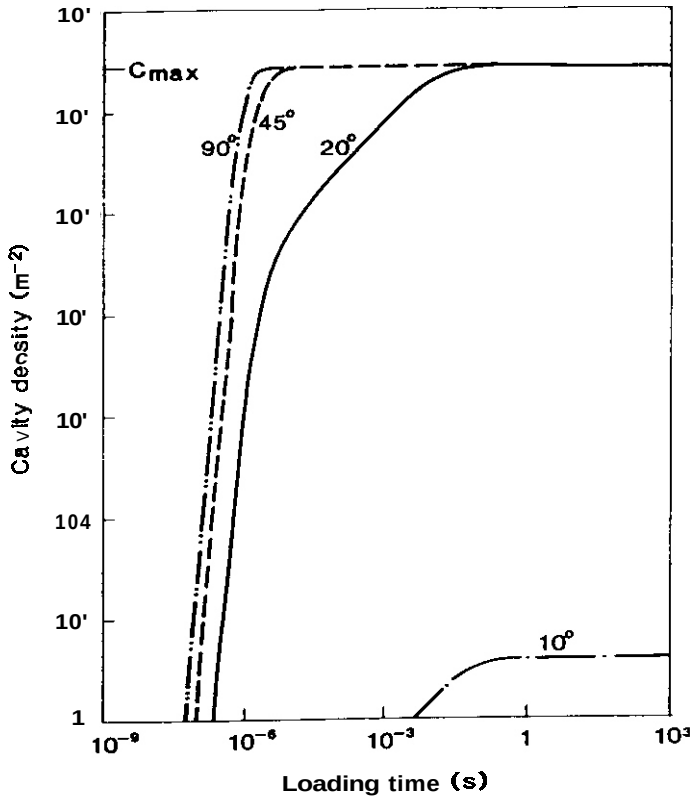

FIGURE 3. Density of cavity nuclei at boundaries of various inclinations at 600°C and F_V = 0.01 as a result of a single sliding pulse. The applied stress is 100 MPa.

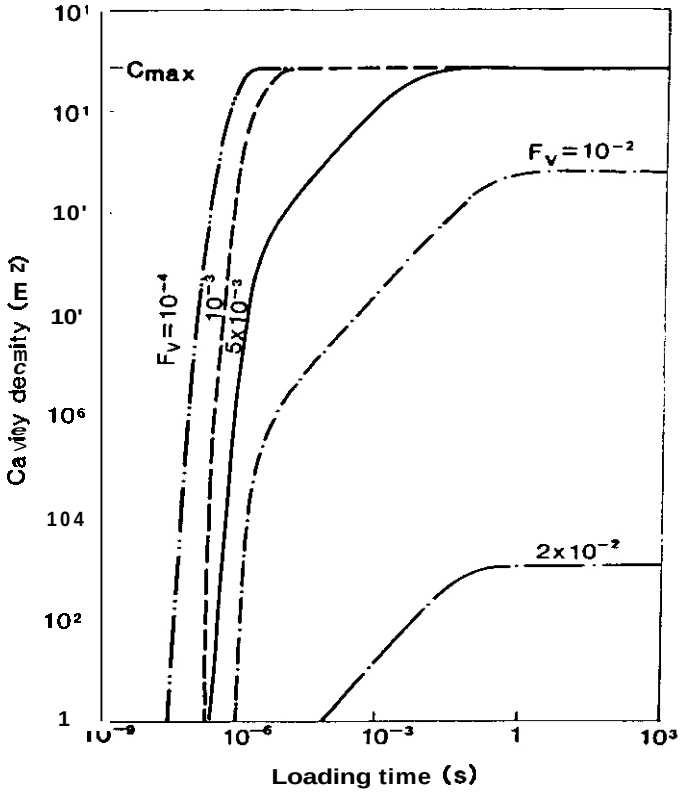

FIGURE 4. Density of cavity nuclei for various values of F_V at 600°C, a boundary inclination of 15 deg, and an applied stress of 100 MPa.

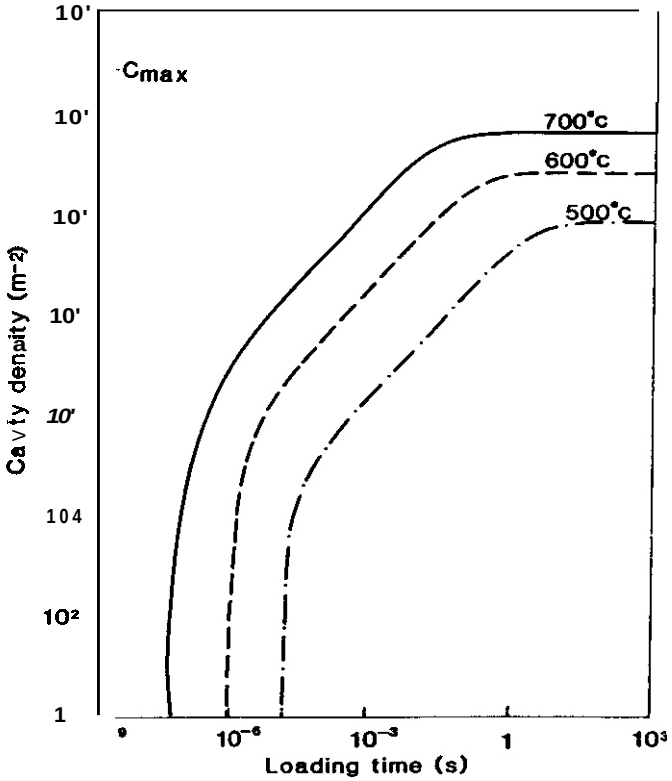

FIGURE 5. Density of cavity nuclei as a function of temperature for F_V = 0.01, a boundary inclination of 15 deg, and an applied stress of 100 MPa.

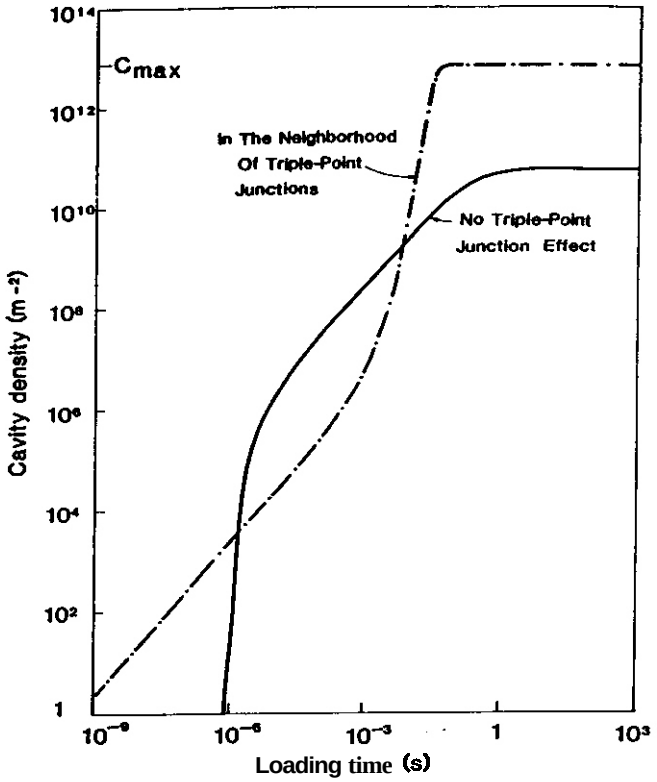

FIGURE 6. Density of cavity nuclei in the neighborhood of a triple-point junction and at a distance far from the triple point. The applied stress is 100 MPa at 600°C and F_V = 0.01.

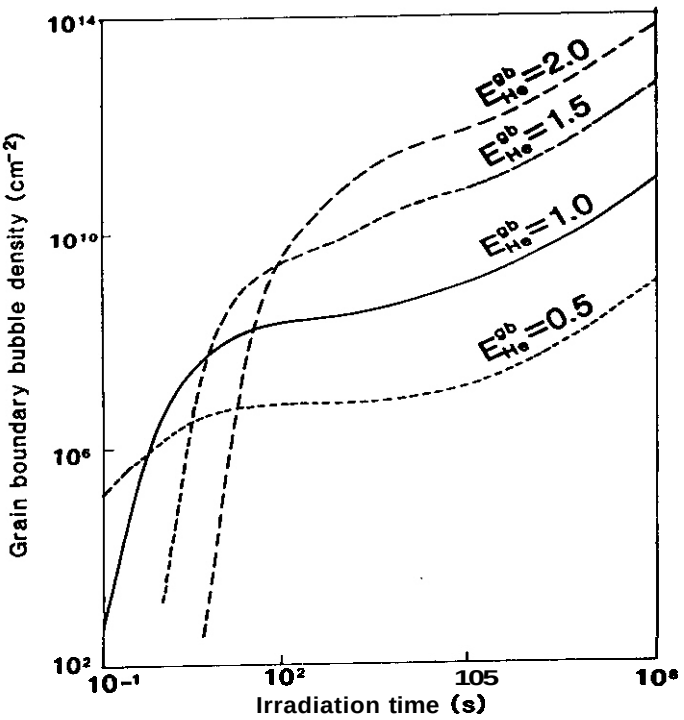

FIGURE 7. The effect of the grain boundary migration energy on the grain boundary bubble density.

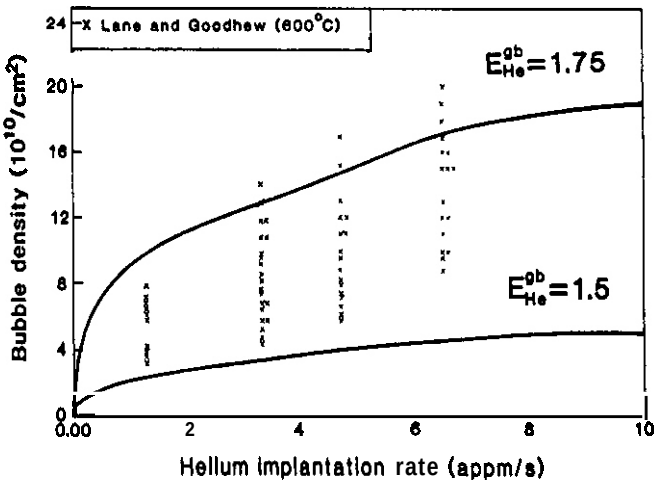

FIGURE 8. The influence of the He migration energy on the grain boundary bubble density. The total injected He is 5600 appm (data from Ref. [15]).

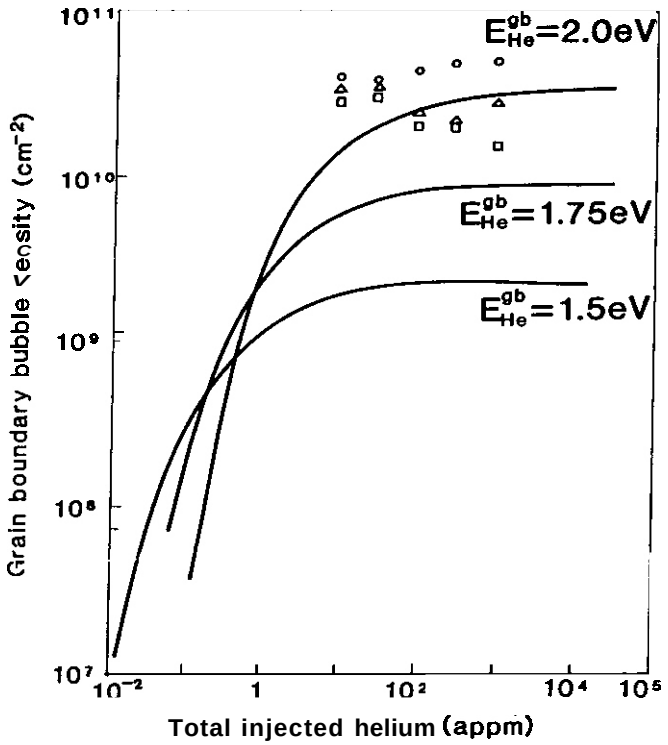

FIGURE 9. Grain boundary bubble density as a function of the He concentration (data from Ref. [12]).

NEUTRON-INDUCED SPINODAL-LIKE DECOMPDSITION OF Fe-Ni AND Fe-Ni-Cr ALLOYS

F. A. Garner and H. R. Brager (Hanford Engineering Development Laboratory)

1.0 Objective

The affect of this effort is to determine those factors which control the swelling, creep, and mechanical response of irradiated alloys.

2.0 *Summary*

Several new experiments continue to illuminate the nature of the spinodal-like decomposition that occurs during neutron irradiation of alloys in the Invar compositional range. The decomposition exhibits a strong cyrstallographic orientation characteristic of spinodal decomposition and occurs at temperatures as low as 420°C.

3.0 Program

Title: Irradiation Effects Analysis (AKJ)
Principal Investigator: D. G. Doran
Affiliation: Hanford Engineering Development Laboratory

4.0 Relevant DAFS Program Plan Task/Subtask

Subtask II.C.1 Effects of Material Parameters on Microstructure

5.0 Accomplishments and Status

5.1 Introduction

In earlier reports it was shown that Fe-Cr-Ni alloys in the Invar compositional regime tend to decompose in a spinodal-like manner when irradiated with either neutrons or charged particles.[1,2] This process has been identified as having pronounced consequences on void swelling[3] and mechanical properties.[4] Several questions regarding this process are still under investigation.

5.2 Temperature and Compositional Dependence of Decomposition Process

The observed increase at 450°C in yield strength of irradiated Fe-15Cr-XNi alloys with nickel content in the range X = 25 - 45 nickel[4] cannot confidently be ascribed to spinodal-like decomposition unless one demonstrates that such a process actually operates at 450°C. The lowest temperature at which compositional micro-oscillations have previously been observed is 550°C.[1] At lower temperatures the wave-length of such oscillations is thought to approach or fall below the resolution limit of the EDX technique used to study the process. In addition, void swelling occurs sooner at lower temperatures and imposes additional perturbations on the composition profiles. These arise due to the operation of the inverse-Kirkendall process, by which slower diffusing species are segregated at void surfaces. Thus to study the temperature dependence of spinodal-like decomposition it is imperative to acquire specimens which have been irradiated sufficiently to develop micro-oscillations but not enough to develop void nucleation. This concern is

particularly important when density change measurements are used to select specimens most likely to contain micro-oscillations. Spinodal-like behavior leads to densifications as large as 1%, but this effect is quickly camouflaged by the onset of swelling arising from the voids.

The optimum neutron exposure to maximize the development of micro-oscillations while minimizing swelling is first of all dependent on composition and second dependent on irradiation temperature, reflecting the two major sensitivities of swelling. The most optimum irradiation series conducted to date has recently been discharged from FFTF-MOTA. Fifteen annealed alloys in the near-Invar regime have been irradiated to 9 dpa at 420°C and to 14 dpa at 520°C and 600°C. The lower dose at 420°C is convenient since swelling is known to start in this Fe-Cr-Ni alloy series at $\geq$10 dpa in the range 420-500°C.[5]

Note from Table I that while swelling has occurred in some specimens many of these alloys exhibited densification. At 420°C, the densifications were as large as 0.7%, indicating that phase decomposition by micro-oscillations most likely is occurring. Note also that a densification of 1.14% occurred at 600°C in Fe-45Ni. This and the data for Fe-35Ni confirms our earlier conclusion that the presence of chromium is not necessary to develop micro-oscillations.[1,2] Comparison of the results at 35 and 45% nickel also supports the contention that the greatest consequences of this process lie nearer the 45% level, a conclusion drawn from mechanical property studies.[4]

Many of these specimens have been set aside for later examination by EDX and TEM.

TABLE I

OENSITY CHANGES OBSERVEO IN IRRADIATED NEAR-INVAR ALLOYS IN FFTF-MOTA

Alloy wt %	% Swelling 400°C, 9 dpa	520°C, 14 dpa	600°C, 14 dpa
Fe-30Ni-7Cr	0.52	0.63	--
Fe-35Ni	--	-0.55	-0.42
Fe-35Ni-5Cr	-0.48	-0.09	0.16
Fe-35Ni-7.5Cr	-0.16	0.16	-0.01
Fe-35Ni-11Cr	0.04	-0.07	-0.13
Fe-35Ni-15Cr	0.51	--	0.41
Fe-40Ni-5Cr	-0.70	-0.31	0.29
Fe-40Ni-7.5Cr	-0.27	0.11	0.11
Fe-40Ni-11Cr	-0.33	-0.29	-0.38
Fe-45Ni	0.19	-0.27	-1.14
Fe-45Ni-7.5Cr	0.12	--	0.12
Fe-45Ni-15Cr	0.39	--	0.04
Fe-50Ni-5Cr	-0.66	-0.14	-0.39
Fe-50Ni-11Cr	-0.11	-0.16	--
Fe-55Ni-7.5Cr	--	-0.28	-0.10

5.3 Nature of the Spinodal-Like Process

It has not yet been established whether this phenomenon is merely an irradiation-accelerated version of a naturally occurring but sluggish process or whether radiation-produced point defects are necessary for the continued maintenance of the compositional oscillations. The answer to this question is necessary in order to confidently predict whether this process can be used as the basis of a swelling resistant alloy.

In order to study this question, several experiments are in progress. First a specimen of Fe-35.5Ni-7.5Cr irradiated to 38 dpa at 593°C has been annealed for 24 hours at 600°C and will be examined by TEM and EDX after rethinning to avoid potential surface effects on microsegregation and its relaxation upon annealing.

This specimen has been examined a number of times earlier, including results to be shown in the next section. It has exhibited pronounced micro-oscillations in composition and a density increase of 0.9%. If the oscillations are still observed after the annealing, the specimen will be annealed again at higher temperatures. The object of this experiment is to demonstrate whether the radiation-induced oscillations are stable in the absence of radiation.

Another experiment involves the Fe-45Ni specimen at (600°C, 14 dpa, 1.1% densification) described in the previous section. A multiple thinning technique has been developed which allows four separate 1 mm diameter areas to be thinned in this single specimen. Using alternate density change measurements, annealing, thinning and TEM/EDX studies, the stability of these micro-oscillations in the absence of radiation will be determined.

5.4 Crystallographic Dependence of the Decomposition Process

One must first determine whether this process results in merely random fluctuations in composition or whether they are regular and periodic in nature. Second, if they are regular, do these oscillations exhibit the same dependence on crystallographic direction as predicted for spinodally decomposed fcc alloys, in which the longest oscillation wavelength is predicted to be along <100> directions.[6]

L. E. Rehn and P. R. Okamoto have recently suggested in a letter that a method exists which can be used to discriminate between random fluctuations and truly periodic behavior. Citing an article by M. Kac[7] they note that if random numbers are plotted at equidistant intervals, the average distance between peaks in the data will approach three of these intervals as the series of numbers grows larger. Therefore if one uses a different sampling interval, the period of oscillation should appear to change. While the impact of this suggestion is still being assessed with respect to questions of foil thickness, probe diameter, etc., the crystallographic dependence continues to be investigated. In previous studies the compositional traces were taken along unidentified crystallographic vectors, reflecting the difficultly associated with such determinations when using the single tilt stage normally used for EUX analysis.

In one recent study, however, the specimen was progressively rotated in the holder until a suitably thin area was positioned within several degrees of a (100) foil normal such that EUX measurements were feasible along a series of parallel <100> lines. This specimen was derived from the 593°C, 38 dpa irradiation of Fe-35-5Ni-7.5Cr previously reported in earlier studies. Using random direction traces the period was earlier reported to be on the order of 300-400 nm.[1]

Figure 1 shows that in a region where the foil thickness was on the order of 75 ± 20 nm that the period between minima in the nickel profile along a given <100> trace is ~100 nm. Figure 2 shows a comparable <100> trace in a thicker (120 ± 25 nm) portion of the same area, with the pericd between maxima appearing to be on the order of ~120 nm. In both traces the iron and chromium profiles are mirror images of that of nickel.

Although the data presented in Figures 1 and 2 confirm that the period along <100> directions is longer than that previously observed on random-direction traces, the trace procedure chosen does not guarantee that a given <100> trace will go through the maxima defined along perpendicular traces. Figure 3 presents the results of a time-consuming compositional mapping of a fairly large region of crystal volume, all contained in one grain. The area chosen is near that mapped in Figures 1 and 2, was near the foil edge and was roughly 100 nm thick. The mapping is done along <100> directions, one of which was conveniently parallel to the foil edge. Note that the three minima (defined as 530% Ni) are spaced at ~1000 nm (~1 μm) apart along a <100> direction. The large distances involved and the gradient in thickness perpendicular to the foil edge precluded the mapping of a larger area. The local maxima appear to be offset on other parallel <100> traces. No microstructural components such as voids or dislocations were found in this crystal volume.

5.5 Conclusions

It is apparent that the compositional micro-oscillations induced in Invar alloys during irradiation exhibit a strong dependence on crystallographic direction, with their longest period found to date to be along <100> directions. Based on density change information it also appears that these micro-oscillations persist to temperatures as low as 420°C. More work is required to determine the nature of these oscillations and the forces which lead to their formation.

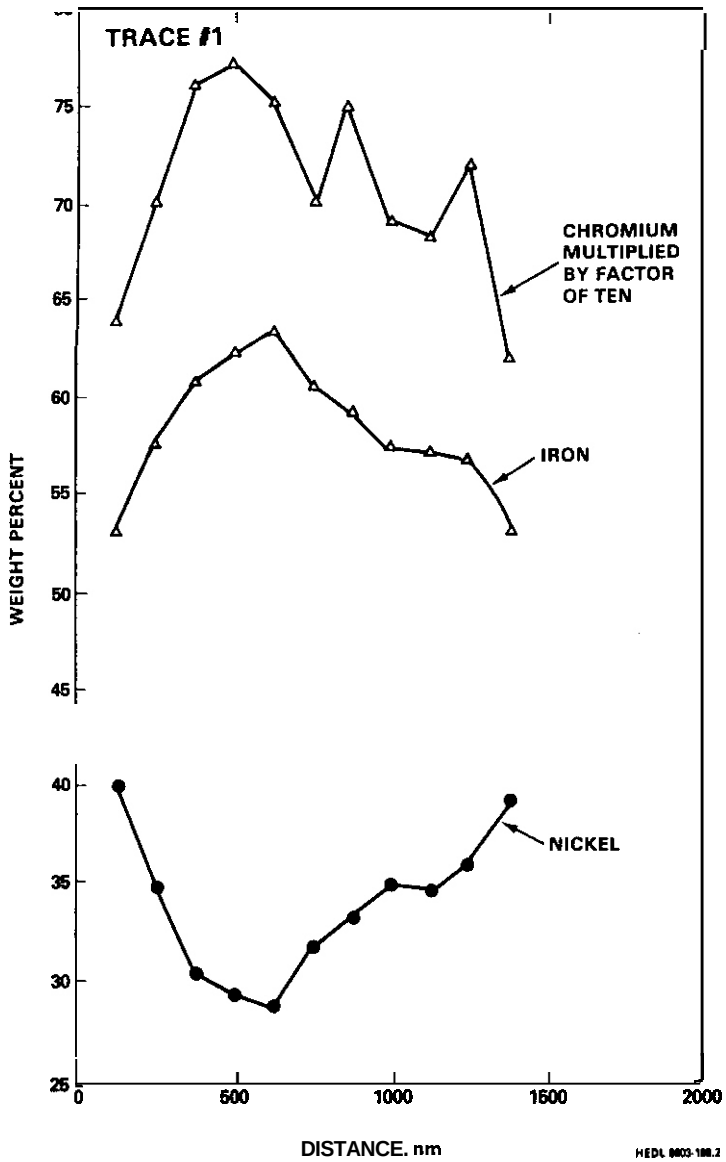

Figure 1. Compositional traces along <100> direction in Fe-35.5Ni-7.5Cr irradiated at 593°C to 38 dpa, in a region 175 nm thick.

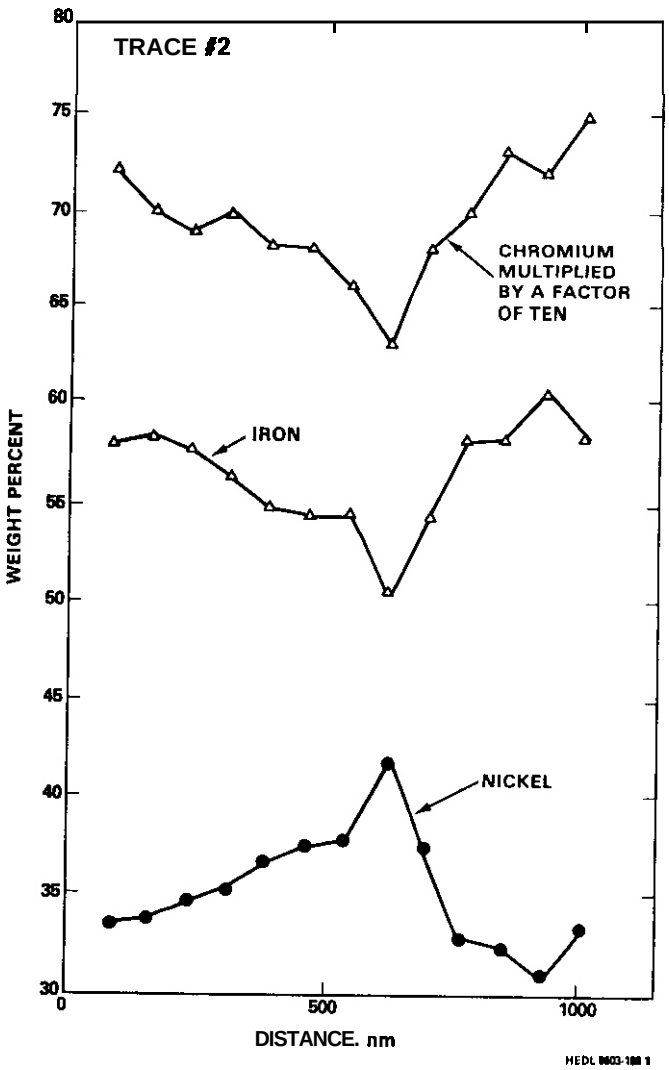

Figure 2. Trace similar to that of Figure 1 in a region ~100 nm thick.

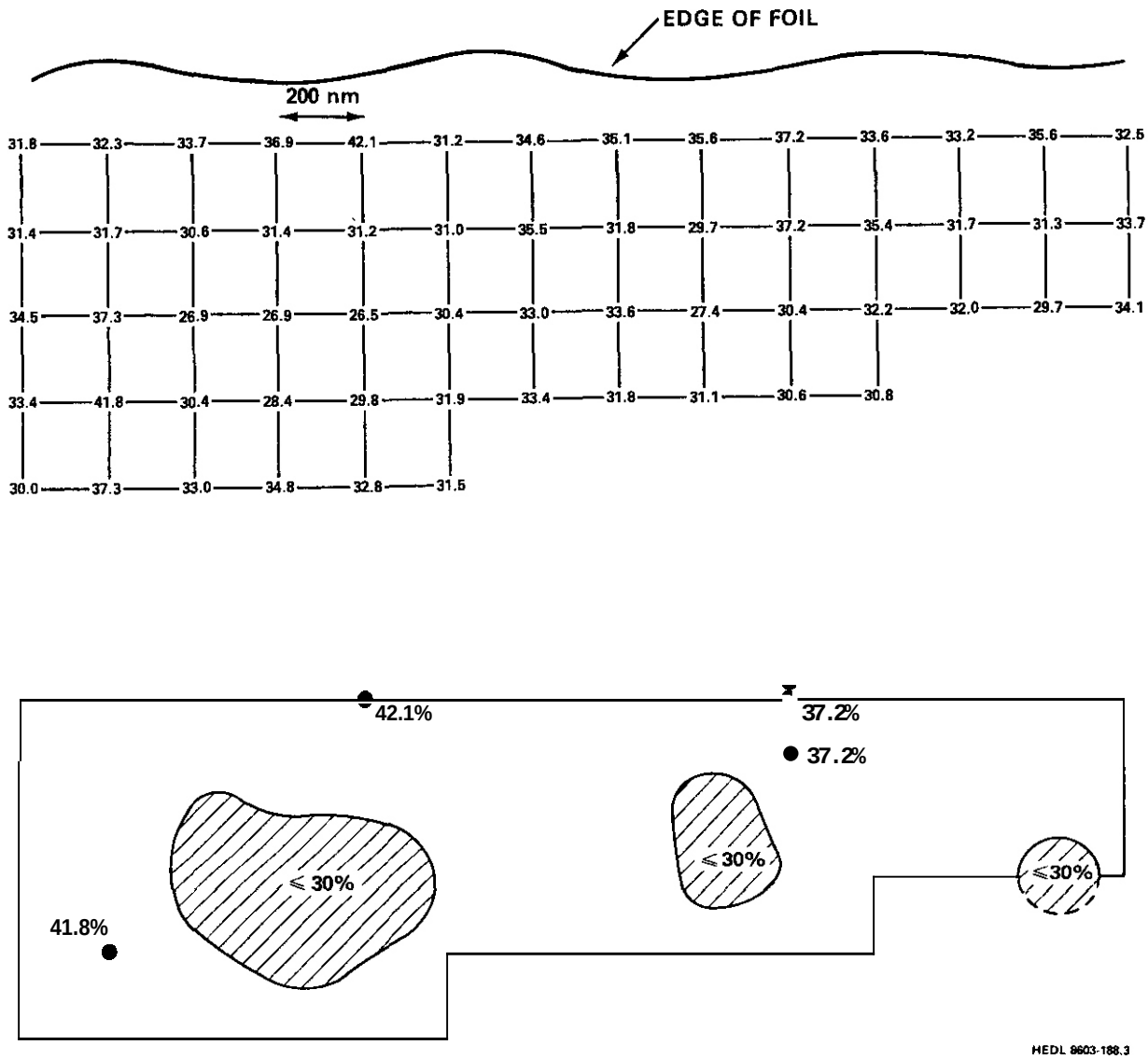

Figure 3. (a) Two-dimensional compositional map of Fe-35.5Ni-7.5Cr along <100> directions using a 200 nm sampling interval, (b) major features derived from the detailed map shown in (a).

6.0 References

1. H. R. Brager and F. A. Garner in Optimizing Materials for Nuclear Applications, TMS-AIME, Warrendale, PA (1985) pp. 141-166.

2. F. A. Garner, H. R. Brager, R. A. Dodd and T. Lauritzen, Nuclear Instruments and Methods in Physics Research, to be published shortly, also HEDL-SA-3280.

3. F. A. Garner, J. Nucl. Mater., 133/134 (1985) 113.

4. H. R. Brager, F. A. Garner and M. L. Hamilton, J. Nucl. Mater., 133/134 (1985) 594.

5. F. A. Garner, J. Nucl. Mater., 122/123 (1984) 459.

6. J. W. Cahn, Acta Metall., 11 (1963) 1275.

7. M. Kac, American Scientist, 71 (1983) 186.

7.0 Future Work

Post-annealing experiments will be performed on several alloys and examination of both neutron and ion bombarded specimens will continue.

8.0 Publications

None

THE INFLUENCE OF UNCERTAINTIES IN MATERIAL PROPERTIES, AND THE EFFECTS OF DIMENSIONAL SCALING ON THE PREDICTION OF FUSION STRUCTURE LIFETIMES

James P. Rlanchard and Nasr M. Ghoniem (University of California, Los Angeles)

1.0 Objectives

The objectives of this work are to investigate the effects of uncertainties in measurements of swelling and creep rates on predictions of the lifetime of mirror reactor blankets. Also, the work explores the effects of dimensional scaling of commercial size blankets on the lifetime for testing purposes.

2.0 Summary

The sensitivity of lifetime predictions for fusion reactor blanket structures is investigated by applying the Monte Carlo numerical technique. A structural computer code, STress Analysis Including Radiation Effects (STAIRE), developed for the analysis of mirror fusion blankets, is used as a deterministic model for the prediction of the lifetime of semicircular coolant tubes. Uncertainties in material variables are treated as prohahilistic inputs to the STAIRE code and output distributions are obtained.

Irradiation creep rates are shown to be sufficient for relaxation of swelling-induced stresses under most conditions. In absence of high stresses, the creep limit seems to he life-limiting, although this depends on the designdependent swelling limit In the case of the Mirror Advanced Reactor Study (MARS) blanket design, a lifetime of several hundred dpa is shown to be highly probable.

3.0 Program

Title: Radiation Effects on Structural Materials
Principal Investigator: N. M. Ghoniem
Affiliation: University of California, Los Angeles

4.0 Relevant OAFS Program Task/Subtask

Subtask III.B.2.3 Correlation methodology

5.0 Accomplishments and Status

5.1 Introduction

The lack of a large data base for material properties in a prototypical fusion environment complicates the process of component lifetime prediction. A considerable degree of uncertainty is associated with measurements aimed at assessing radiation effects on structural materials. If we consider structural swelling due to neutron displacement damage as an example, we realize the sizable degree of ambiguity in the swelling behavior due to the nature of the irradiation environment. Displacement damage rate, helium generation rate, and helium-to-dpa ratio are just a few of the parameters that influence swelling. Other uncertainties may result from heat-to-heat variations, compositional differences, sample conditions, etc. In view of such a wide range of conditions, a lifetime prediction of a fusion reactor component is best treated as a probabilistic quantity. This is especially true if various phenomena interact in a non-linear fashion.

A sensitivity analysis of a blanket's lifetime can be used to guide future materials testing. If the lifetime is particularly sensitive to a measurable property, such as the creep modulus or the swelling rate,

additional testing in that area can be quite valuahle to designers. Alternatively, testing of parameters for which uncertainty has little impact on blanket life can be deemphasized. The potential for equipment and manpower savings are obvious.

4 useful by-product of a detailed lifetime analysis is a set of scaling functions which contain the dependence of the blanket dimensions. Full-size fusion reactor blanket modules must eventually he tested before commercial fusion is achieved. To reach this goal, however, smaller size modules may have to he used in order to study interactive phenomena at a reasonable cost. An interesting question arises in this regard: Is it possible to preserve the "structural state" of a hlanket module when its size is scaled down? In other words: Can the failure of a structure he simulated by a scale model? The scaling functions can be utilized to address these questions.

We have recently developed the computer code STAIRE for the determination of blanket structural response in mirror fusion reactors [1]. The model has been applied to the analysis of the MARS [2] blanket modules. The significant features of this work are the inclusion of radiation swelling and creep, as well as thermal creep. With this in hand, it is possihle to perform a complete structural analysis of semicircular tubular fusion blankets, as described in the MARS design.

We aim to accomplish two objectives in this paper: (1) to establish the sensitivity of lifetime predictions to uncertainties in material properties and (2) to develop scaling functions for the study of the effects of geometrical dimensions on lifetime determination.

In the following section, we discuss stress and strain limits that determine the structural lifetime. In Sec. 3 we present simple analytical equations for the determination of component lifetime hased on swelling, stress or creep strain limits. This is followed by a brief description of the stress analysis model as applied to a mirror fusion reactor blanket. We then proceed to develop methodology for determining the sensitivity of lifetime predictions to material variables in Sec. 5 and scaling relationships in Sec. 6. Section 7 is devoted to the results of the analysis. Conclusions are given in Sec. 8.

5.7 Stress and Strain Limits

After performing a thorough stress analysis, the structure's life is determined by imposing limits on either the strain or stress. Strain limits account for impaired performance due to either large deflections or damage which causes fracture or rupture, while stress limits account for a number of failure modes. In this paper, limits of 10% swelling (excessive deformation) and 1% total creep strain (damage) are considered. The creep limit is based on guidelines in the ASME Code [3], despite the fact that the code does not treat irradiation creep explicitly. In this context, the limit is somewhat contrived hut it can still be meaningful if considered as a conservative limit. Since it has been argued that irradiation creep is nondamaging [4] and thermal creep rates in HT-9 are low for the temperature at which the MARS blanket operates [5], the actual damage limit could actually be much higher than 1%. Conservative limits are advisahle though, until more is known about material failure in a fusion environment.

Stress limits, such as those in the ASME Code, attempt to account for a number of possible failure mechanisms, including tensile instability and creep rupture. Again, the present analysis employs stress limits suggerted by the ASME Code, although these limits do not explicitly include radiation effects. As with the damage limit, the stress limit used in this paper is conservative, although for different reasons. In the ASME Code, thermal stresses (referred to as secondary stresses) have higher allowable levels because they are self-limiting. However, a key deficiency of the Code is the absence of any timedependent strain that would be analogous to void swelling. Failure due to stresses developed by such a phenomenon will likely be hounded hy the well understood primary ami secondary stresses considered in the Code, so the conservative primary stress limit has been used because of the uncertainty involved.

The values in Table 1 illustrate stress limits for the two structural materials HT-9 and 2-1/4 Cr-1Mo [5]. The limits are determined according to the ASME Boiler and Pressure Vessel Code guidelines for S_{mt}.

5.3 Lifetime Equations

This section presents material behavior equations that are used to model swelling and irradiation creep. In each case, these equations are the simplest available; therefore some potentially significant effects are ignored. The swelling equation, for instance, ignores temperature dependence of the incubation dose ami stress dependence of the swelling rate. Also, the irradiation creep rate is assumed to be independent of

Table 1
Stress Limits (MPa) for Ferritic/Martensitic Alloys (Without Irradiation)

Temperature (°C)	2 1/4 Cr-1Mo		HT-9	
	3 years	30 years	3 years	30 years
450	170	170	190	1R5
475	160	130	180	155
500	130	100	155	130
525	ion	80	130	105
550	80	60	105	80

5.3.1 Swelling Limit

If one assumes that the swelling rate in a material is independent of the stress state, the lifetime can he easily determined. In general, the swelling rate depends on the hydroctatic stress [6], hut this effect is assumed to he small. The volumetric swelling $\Delta V/V$ is given by an equation of the form:

$$S(T) = \Delta V/V = \dot{S}(T)(\delta - \delta_I) \quad , \tag{1}$$

where δ is the dose in displacements per atom (dpa), δ is the incuhation dose, and $\dot{S}(T)$ is the swelling rate at a given temperature T. The lifetime (in dpa) due to a swelling limit S_{lim} is then given hy:

$$\delta_L^S(T) = S_{lim}/\dot{S} + \delta_I \quad , \tag{2}$$

where S_{lim} is a predetermined engineering swelling limit, which is design dependent. For the MARS design [2], the average swelling is about 2/3 of the peak swelling, due to the predicted temperature variations in the swelling rate [7], so one must he careful to specify whether the peak or average swelling is life limiting.

5.3.2 Creep Limit

Commonly, irradiation creep is modeled according to [8]:

$$\dot{\epsilon}^c = C\,\sigma \quad , \tag{3}$$

where $\dot{\epsilon}^c$ is the creep strain rate (s^{-1}), C is the creep compliance ($MPa^{-1}\,s^{-1}$) and σ is the effective stress. Using modified beam theory, which applies to the MARS blanket, one finds the following equation for the local stress in the blanket pipes [1]:

$$\sigma = \begin{cases} \sigma_0 \exp(-\delta/\Delta) & \delta < \delta_I \\ \sigma_0 \exp(-\delta/\Delta) + \dot{\sigma}\Delta\{1 - \exp[-(\delta - \delta_I)/\Delta]\} & \delta > \delta_I \end{cases} \quad , \tag{4}$$

where σ_0 is the thermal stress, $\dot{\sigma}$ is the creep-free rate of stress increase (MPa/dpa), δ_I is the incuhation dose, and Δ is a relaxation parameter given by

$$\Delta = 1/CE \quad , \tag{5}$$

where E is Young's Modulus. Equation (4) features an exponential decay of the thermal stress and an exponential approach of the local stress to a steady-state value of $\dot{\sigma}\Delta$.

Integrating Eq. (3) with Eq. (4) and assuming that the lifetime is much greater than the incuhation dose (which seems to he valid for ferritic steels), one finds

$$\delta_L^c = \delta_I + \Delta + (E\epsilon^c_{lim} - \sigma_0)/\dot{\sigma} \quad , \tag{6}$$

where $\varepsilon^c_{\ell im}$ is a predetermined creep limit. Hence, for a given material, the creep life depends only upon σ_0 and σ, which are design dependent.

5.3.3 Stress Limit

The stress-limited life is easily obtained from Eq. (4). Assuming $\delta_L^\sigma > \delta_I$, one finds

$$\delta_L^\sigma = -\Delta \ln \left[\frac{\sigma_{\ell im} - \dot{\sigma}\Delta}{\sigma_0 - \dot{\sigma}\Delta \exp(\delta_I/\Delta)} \right] , \tag{7}$$

where $\sigma_{\ell im}$ is the stress limit. In deriving this equation, the quantity in brackets was assumed to be positive.

5.4 Model Description

The investigation in this paper is generic and can be applied to any irradiated structure once a stress analysis approach has been adopted. To give specific conclusions, however, we will apply the structural code STAIRE [1]. This computer code has been developed by a modification of beam and arch theory to include inelastic radiation strains. The method has been successfully applied to the MARS [2] blanket configuration. For the reader's benefit, we include in this section a brief description of the method and its application to the MARS study.

Figure 1 shows one pipe of the MARS blanket. In our model, we treat the pipe as an indeterminate beam of a hollow cross section. Recause the pipes are indeterminate, the stresses and deflections are coupled and must he simultaneously found by setting up three equations for the deflections at the end of the pipe in terms of the inelastic strains and the unknown end reactions. For example. the equation for the radial displacement at the end ΔR is:

$$\Delta R = - \int w' x ds + \int \bar{e}' \sin\theta ds + XM \int \frac{x ds}{EI} + XF \int \frac{xy ds}{EI} + XP \int \frac{y^2 ds}{EI} , \tag{8}$$

where

$$w' = \frac{1}{K_{II} I} \int_A \left(e^c + \frac{\Delta V}{3V} + \alpha T\right) \xi dA , \tag{9}$$

and

$$\bar{e}' = \frac{1}{A} \int_A \left(e^c + \frac{\Delta V}{3V} + \alpha T\right) dA . \tag{10}$$

The quantity w' is the change in curvature due to the inelastic strains and $\bar{e}'$ is the average inelastic strain over the cross-sectional area A. Combining Eq. (8) with equations for the axial end displacement and end rotation, the system can be solved for the end reactions XM. XF, and XP.

Once the reactions are known, the stresses in the pipe can he determined with the use of simple statics. The moment M and axial force F, at any angle θ, can be found in terms of the reactions. The axial stress is then given by:

$$\sigma = \frac{F}{A} + \xi(1 - K_I \xi^2)\left(\frac{M}{K_{II} I} - Ew'\right) - E\left(e^c + \frac{\Delta V}{3V} + \alpha T - \bar{e}'\right) , \tag{11}$$

where K_I and K_{II} are constants determined by the pipe dimensions. ξ is the distance from the neutral axis at a given cross section, I the moment of inertia, e^c is the creep strain, $\Delta V/3V$ is the swelling strain, α is the coefficient of thermal expansion. and E is Young's Modulus. For further details of the method, the reader should consult Ref. [1].

5.5 Uncertainty Analysis

5.5.1 Monte Carlo Technique

Because the irradiated behavior of many ferritic steels is essentially unknown, an investigation of the response of a first wall to changes in the material parameters is useful for addressing the relative importance of these unknowns. If the blanket life calculation is not sensitive to variations in a given

parameter. then precise knowledge of the value of that parameter is relatively unimportant and testing should he focused elsewhere. These types of evaluations can be made by considering material parameters as random input, with a probability distribution centered about some average value. Then the response is also random and its distribution about an average indicates its sensitivity to a particular input or groups of inputs.

There are two hasic methods for inserting random variables into a structural model. The first, which is termed linear statistical analysis [8], uses a truncated Taylor's series expansion to create a relationship between the input variahles and the random response. The drawback of this method is that it only yields limited information about the response function [8].

The second method is a Monte Carlo technique [8], which is ideal for use with an existing computer code. In essence, the method simulates an experiment by generating a random number to represent the uncertainty in each input parameter and then calculates the corresponding parameter according to an assumed distribution function. The structural response to these inputs is then calculated. After repeating this process many times, a response distribution is ohtained. This method is generally more favored than the Taylor's series approach because it yields the complete response function, regardless of the degree of non-linearity in the relationship between input and output. The Monte Carlo method will be used here for the above reasons and because it adapts very well to use with the STAIRE computer code.

5.5.7 Input Representation

In representing a random input or output, one assigns to it a probability density function $p(z)$, where $p(z)dz$ is defined as the probability that a variable exists between z and $(z + dz)$. In addition, one can also consider the cumulative probability distribution functions $P(z)$, which gives the probability that the variable will have a value less than or equal to z.

In this section, the variahles C, σ_I, and $\dot{S}$ will be treated as random. For comparison purposes, all three will be characterized by normal probability density functions.

To define these functions, an average and standard deviation must he supplied. For the three random input variables, the standard deviation is chosen to he 10% of the average values given in Table 2.

5.6 Scaling Relationships

For a given set of design limits and material parameters, the lifetime depends only on $\dot{\sigma}$ and σ_0, which are geometry dependent. As shown in Fig. 1, the MARS coolant pipes are semi-circular, with the baseline dimensions as given in Table 2. For simplicity, the temperature difference over the cross section, i.e., the difference hetween the shield-side and plasma-side temperatures, is assumed to be independent of E.

In order to allow maximum flexibility in using the lifetime equations generated in Sec. 3, relationships are developed for σ_0 and $\dot{\sigma}$ in terms of four key parameters. First, the stresses are given in terms of the temperature difference ΔT and the radial header translation d, which is the radial distance traveled by one end of the pipe relative to the other. If the pipes are rigidly attached to a fixed header, then no translation is allowed and d = 0. On the other hand, thermal expansion is better accomodated by a less rigid connection at the header. Allowing some radial header motion then, can relieve the stresses and increase the blanket life. In this model, d is positive inward so a negative value will reduce the stresses.

The second set of equations gives the stress parameters σ_0 and $\dot{\sigma}$ in terms of geometric quantities r, t, and R.

Using equations developed previously [1], the maximum thermal stress $\sigma_{0,MAX}$ (in MPa), is found to he

$$\sigma_{0,MAX} = 103.3 + 0.745\ \Delta T + 187.3\ d \quad , \tag{12}$$

$R = 64$ cm	$\alpha = 11.3 \times 10^{-6}\ °C^{-1}$
$r = 5$ cm	$C = 7.25 \times 10^{-7}\ MPa^{-1}\ dpa^{-1}$
$\tau = 0.25$ cm	$\dot{S} = 0.03\%/dpa$
$T_{in} - T_{ref} = 320°C$	$\delta_I = 90$ dpa
$T_{out} - T_{ref} = 470°C$	$\varepsilon^C_{lim} = 0.01$
$\Delta T = -30°C$	$\sigma_{lim} = 180$ MPa
$d = 0$	$S_{lim} = 10\%$ (average)
$E = 180$ GPa	--

assuming all parameters other than ΔT (in K) and d (in cm) are constant. Varying R, r, and t, and keeping ΔT and d constant, one also finds

$$\sigma_{0,MAX} = 2372\ w \left[\frac{0.355 + 1.2\left(\frac{u}{w}\right)^2}{1 + 1.2\left(\frac{u}{w}\right)^2} \right] , \tag{13}$$

where $u = t/r$ and $w = r/R$. According to Eq. (13), $\sigma_{0,MAX}$ depends only on the ratios of pipe dimensions, so if a scale model preserves these ratios and the temperatures, the initial stress will be preserved.

Because the swelling equation used previously [1] was a highly nonlinear function of temperature, equations for $\dot{\sigma}$ could not he derived analytically.. Using the STAIRE code to determine the increase in the local stress due to a constant swelling rate $\dot{S}$, values of $\dot{\sigma}$ for various values of w, u, and R were generated. These data points were fit to equations similar to Eqs. (12) and (13) with a least-squares fitting routine. The results (in MPa/%) are:

$$K = 65.6 - 3.97\ \Delta T \quad . \tag{14}$$

and

$$K = 103 + 332\ u + w\left[74.5\ t\ \frac{9.52 \times 10^{-3}}{u^3}\left(\frac{0.355 + 201\ u^2}{1 + 201\ u^2}\right)\right] , \tag{15}$$

where

$$\dot{\sigma} = K\dot{S} \quad . \tag{16}$$

5.7 Results

5.7.1 Lifetime Predictions

Given the lifetime criteria from Eqs. (2), (6), and (7), the lifetime is the lowest of δ^S_L, δ^C_L, and δ''_L. The following results will consider the stress limit along with either of the strain limits, so the effects of creep and swelling can be accounted for separafely. After choosing values for σ_0 (81 MPa) and K (185 MPa/%), the lifetime can be plotted in terms of $\dot{S}$, as seen in Fig. 2. The 15% peak swelling limit, which leads to a deflection at the pipe's center of approximately 4.4 cm, is the most conservative of the three limits, but the allowable swelling may be lower in other designs.

The importance of the stress limit depends on the relative creep and swelling rates. If the creep rate is lor, the stress will increase rapidly and the stress limit will quickly be reached. On the other hand, a relatively high creep rate will relax the stress leading to a steady-state stress below the limit, thus rendering the stress limit inconsequential. As shown in Fig. 2, a creep rate of $7.3 \times 10^{-7}\ MPa^{-1}\ dpa^{-1}$ leads to a creep-limited life for any value of $\dot{S}$ in the range expected for ferritic steels. However, a creep rate of $1.6 \times 10^{-7}\ MPa^{-1}\ dpa^{-1}$ does invoke the stress limit, leading to rather short lives for swelling rates above 0.03%/dpa.

To investigate the impact of the swelling/creep ratio, one can plot curves of constant life in swelling-creep space. Figure 3 shows a typical plot for $\delta_L = 420$ dpa. For a given material, the swelling/creep ratio ($\dot{S}$/C) can be represented by a straight line from the origin and the lifetime (and the relevant limit) is determined by the intersection with the constant-life curve. As seen, the ratio must be above 1790 MPa to invoke the stress limit. Using data gathered by Gelles and Puigh [9], the $\dot{S}$/C ratio of a typical

ferritic steel is approximately 500 MPa, so the stress limit will not likely be important for the MARS blanket. The design would have to be more highly constrained (thereby increasing K) before the steady-state stress exceeded the stress limit.

5.7.2 Monte Carlo Results

Recause the Monte Carlo method is a sampling process, its accuracy of representation improves as the number of samples or trial runs is increased. Unfortunately, the cost increases with the number of samples, so one must choose a count that is sufficiently accurate and yet affordable. Figure 4 shows the probability density function (pdf) for the blanket life, assuming that C, σ_T, and S are all variable. As seen, the result does not converge to a single function as the number of samples increases, so it is not apparent that even 1000 runs are sufficient for the analysis.

The cumulative distribution function (cdf), on the other hand, integrates out many of the variations inherent In the density function so less samples are necessary for the same accuracy. This is evident in Fig. 5, which shows the distribution function of the blanket life for the same three random inputs. Apparently, even 100 samples would be sufficient for most analyses. The effects of sample size on the accuracy of results can be established [10], hut this is outside the scope of the present study.

The failure criteria used in the analysis can significantly impact the blanket life. Figure 6 gives the lifetime distribution for the swelling and creep limits. The stress limit is not significant because the creep coefficient C is relatively high and the stresses are correspondingly low. The distribution functions are of similiar shape but the swelling-limited curve is shifted almost 200 dpa up the scale. Notice that the results of the Monte Carlo simulations are smoothed in Figs. 5 through 7 for clarity.

The stress limit enters the picture as the average creep coefficient is decreased. If the average value of C is lowered to 1.6 x 10^{-7} MPa^{-1} dpa^{-1}, the lifetime distribution becomes more complex because the stress limit leads to end-of-life at 150 to 400 dpa, When stress limits are reached early in life, the strain limits only affect the remaining blankets, i.e.. there is no interaction between the criteria. These features are displayed in Fig. 7 which differs from Fig. 6 only in the average value of C. For the higher average creep coefficient, the frequency of failure is essentially zero below about 320 dpa.

5.R Conclusions

It is shown in this paper that an analogue Monte Carlo technique can successfully be coupled to a deterministic inelastic structural analysis code. Such a strategy allows investigations of the influence of material property uncertainty propagation on the prediction of structural failure. The need for such a technique is particularly important in fusion reactor applications, since prototypical testing environments are nonexistent and radiation effects on material properties are uncertain. The following are conclusions of the present work, which specifically apply to the structural material HT-9 in a mirror fusion reactor:

1. When considering the buildup of stresses caused by swelling, the stress limit is potentially the most severe of the three lifetime criteria used in this paper.

2. For ferritic steels, the creep rate seems high enough to relax the swelling stresses and the stress limit is relatively unimportant.

3. The strain limit is life-limiting in all cases analyzed.

4. A lifetime of several hundred dpa is highly probable for a ferritic steel blanket in mirror fusion reactors.

These conclusions suggest that future material testing of ferritic alloys should consider radiation creep, to a degree. Once it has been shown that the creep rates of ferritic steels are high enough to relieve swelling stresses before significant buildup occurs, the actual value of the creep rate is unimportant. This is because the accumulated creep strain is driven by the amount of swelling strain it must offset, rather than by the creep rate. When the creep rate is large, the accumulated creep is very nearly equal to the accumulated swelling strain (with opposite sign). Hence, accurate knowledge of the swelling behavior of a material is more important than precise radiation/creep data for reliable lifetime estimates.

6.0 Acknowledgements

The research was performed under appointment to the Magnetic Fusion Energy Technology Fellowship program administered by Oak Ridge Associated Universities for the U.S. Department of Energy. The support of Department of Energy, Contract DE-FG03-84ER52110 to UCLA is appreciated.

7.0 References

[1] J. P. Blanchard and N. M. Ghoniem, "Inelastic Structural Analysis of the MARS Tandem Mirror Reactor," Nucl. Engrg. Des./Fusion 2 (1985) 19.

[2] R. G. Logan et al., "Mirror Mvanced Reactor Study Interim Design Report," Lawrence Livermore National Laboratorv Reoort. UCRL-53333., (April 1983).

[3] ASME Boiler and Pressure Vessel Code, Sections I, II, and III, and Code Case 1592, Class I Components in Elevated Temperature Service, The American Society of Mechanical Engineers, New York, NY (1977).

[4] R. F. Mattas, "Fusion Component Lifetime Analysis," Argonne National Laboratory Report. ANL/FPP/TM-160 (1980).

[5] R. J. Amodeo and N. M. Ghoniem, "Constitutive Design Equations for Thermal Deformation of HT-9." J. Nucl. Mater. 122 (1984) 91.

[6] W. Wolfer, M. Ashkin and A. Roltax, "Creep and Swelling Deformation in Structural Yaterials During Fast-Neutron Irradiation," ASTM STP-570, American Society for Testing and Materials, (1976).

[7] D. Olander, "Fundamental Aspects of Nuclear Reactor Fuel Elements," Technical Information Center, TIC-26711-P1, 115 Department of Energy (1976) 590.

[8] G. Hart, Uncertainty Analysis, Loads, and Safety in Structural Engineering (Prentice Hall, Inc., Englewood Cliffs., NJ, 1982) 65-82.

[9] D. Gelles and R. Puigh, "Evaluation of Ferritic Alloy Fe-2-1/4 Cr-1M_0 After Neutron Irradiation-Irradiation Creep and Swelling." Hanford Enaineerina Develooment Laboratory Reoort. HEDL-7405 (1983).

[10] L. L. Carter and E. D. Cashwell, "Particle Transport Simuiation with the Monte Carlo Method," Los Alamos National Laboratory Report, LANL, TID-26607 (1975).

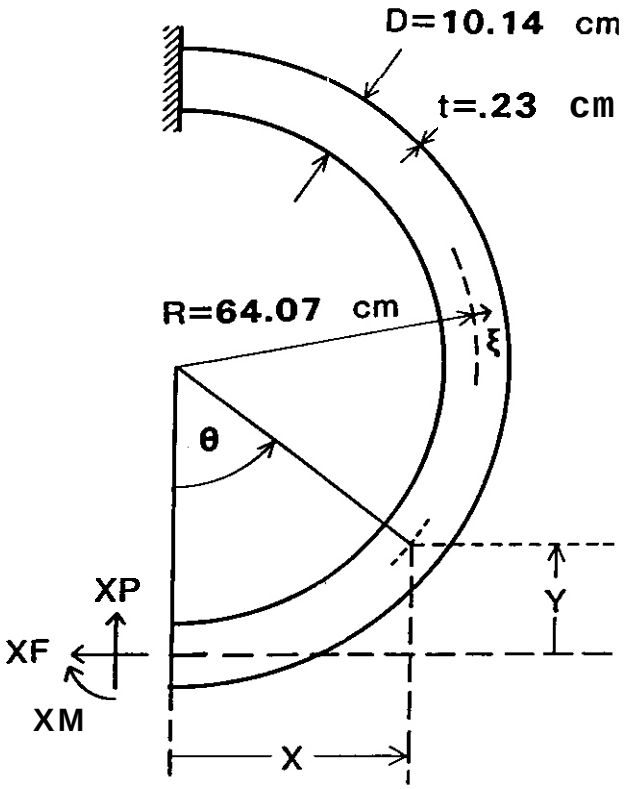

FIGURE 1. Model used for analysis of the MARS coolant pipes.

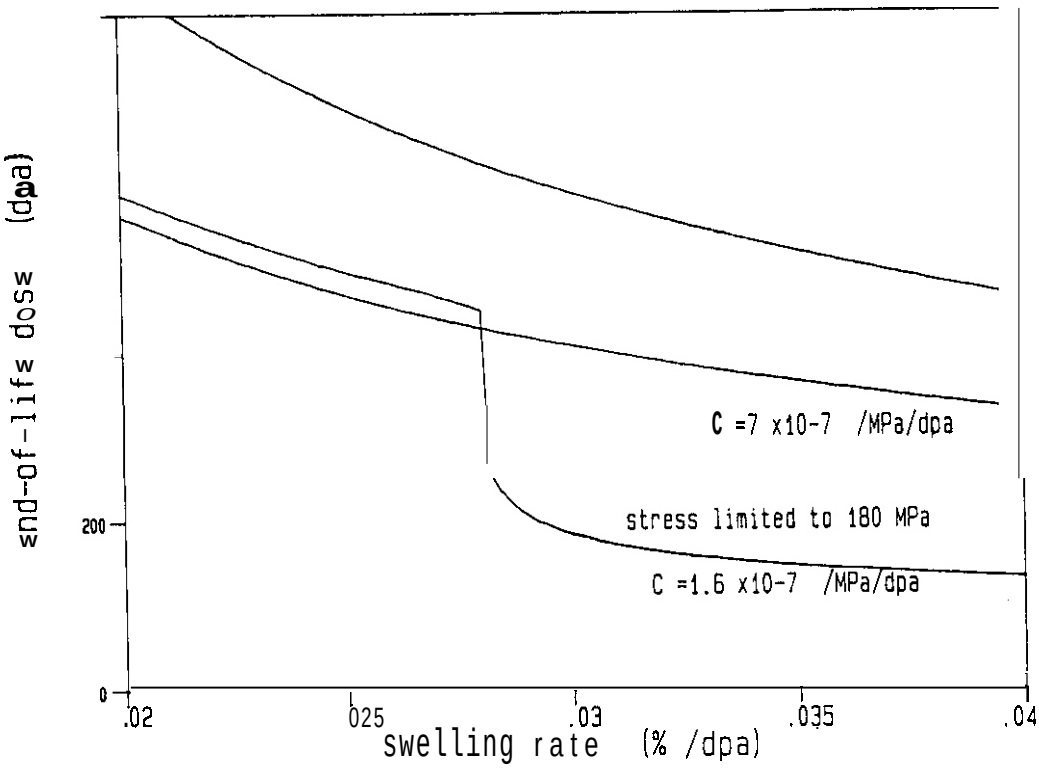

FIGURE 2. Lifetime as a function of swelling rate for the swelling limit and for the creep and stress limits at two different creep rates.

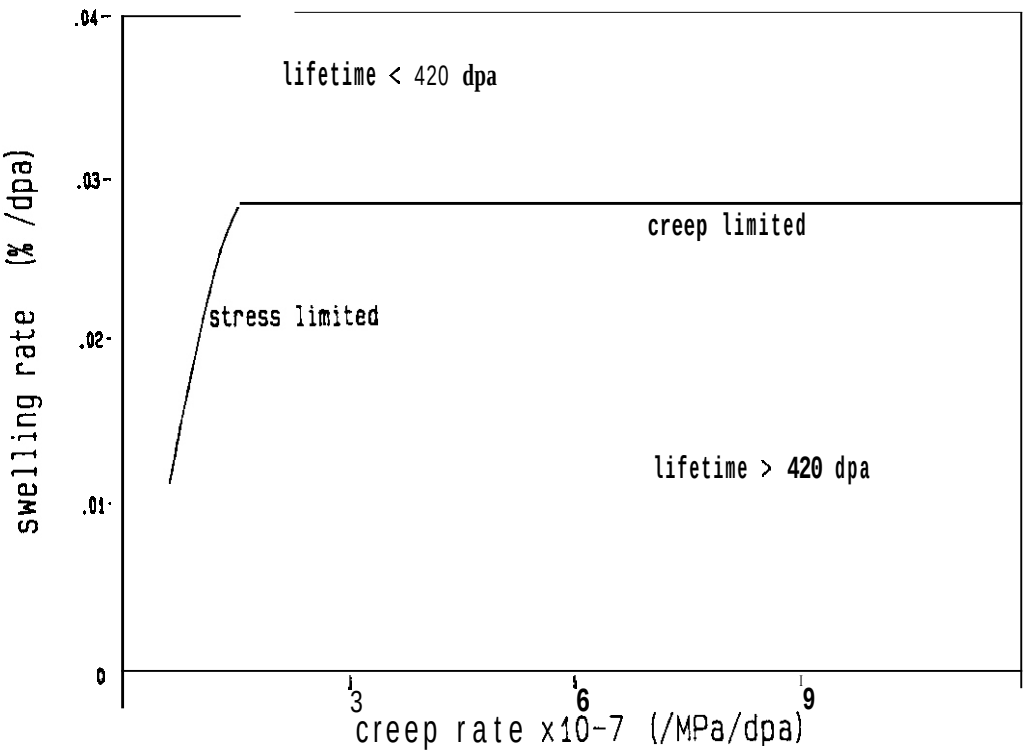

FIGURE **3. Constant-life curve assuming stress and creep damage limits are operative.**

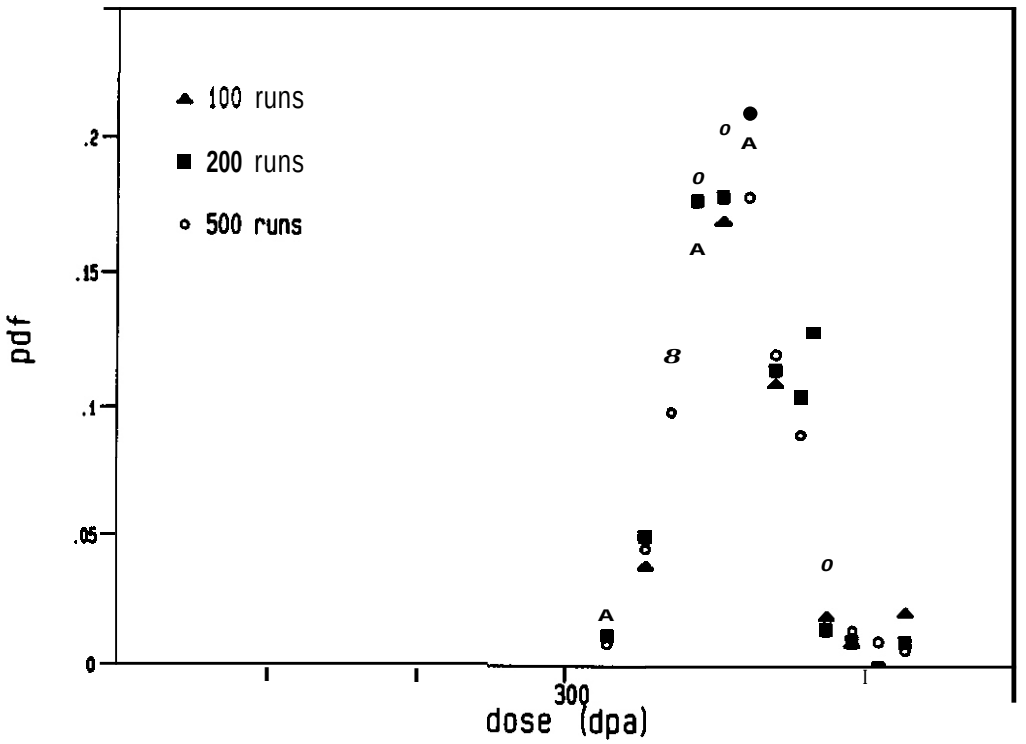

FIGURE 4. Probability density function for three different numbers of Monte Carlo histories.

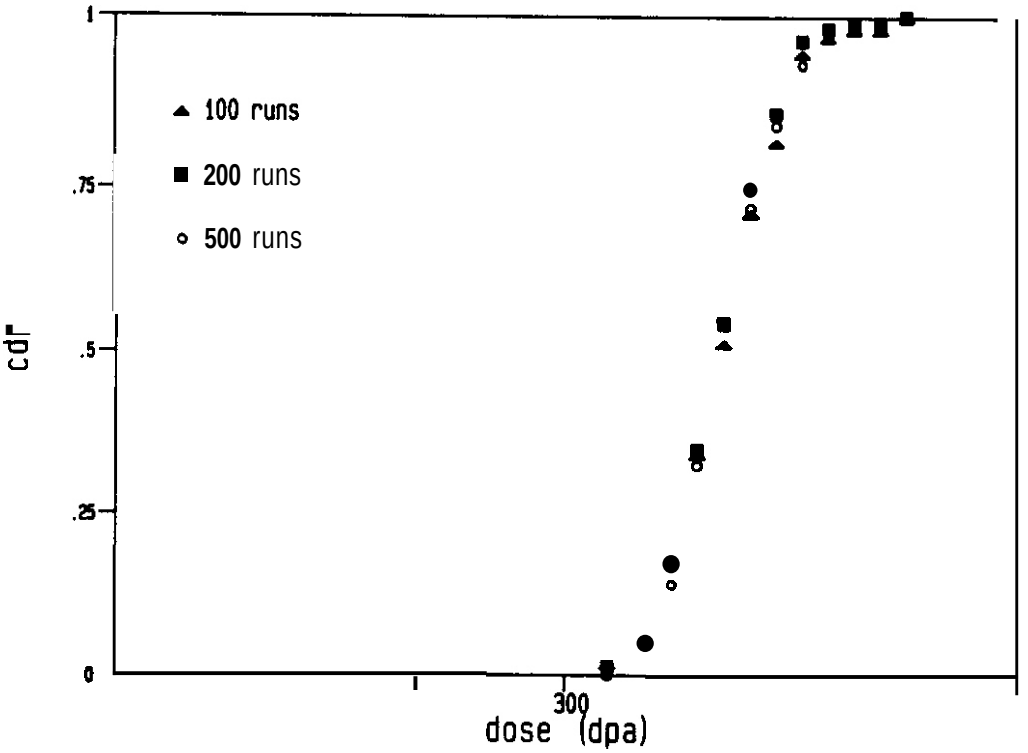

FIGURE 5. Cumulative distribution function for three different numbers of Monte Carlo histories.

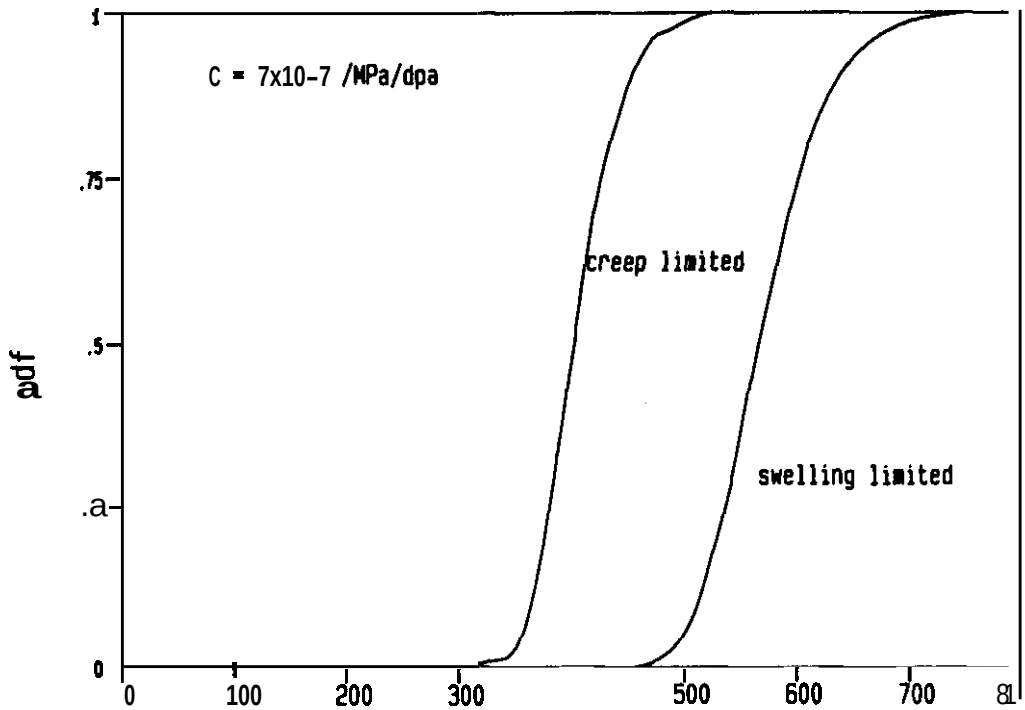

FIGURE 6. Cumulative failure probability far C = 7 × 10^{-7} MPa^{-1} dpa^{-1}.

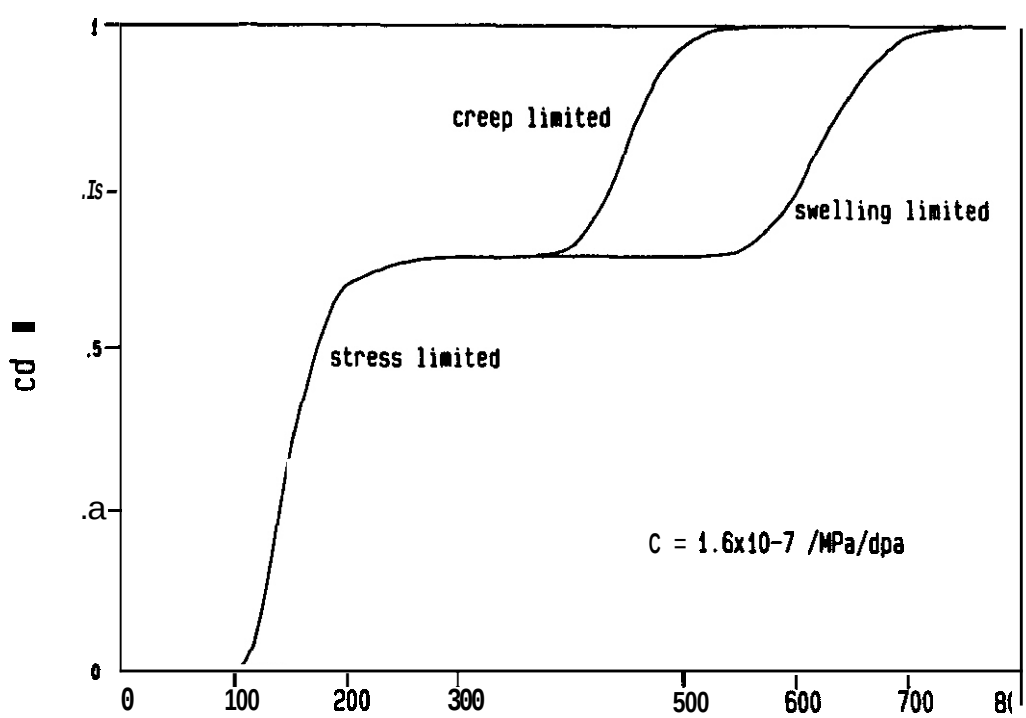

10^{-7}

CHAPTER 5

FUNDAMENTAL STUDIES OF SPECIAL PURPOSE MATERIALS

SWELLING OF PURE COPPER AND COPPER ALLOYS AFTER HIGH FLUENCE IRRADIATION IN FFTF AT ~450°C

F. A. Garner and H. R. Brager (Hanford Enqineering Development Laboratory)

1.0 Objective

The object of this effort is to provide data on the swelling of high conductivity alloys in response to fast reactor irradiation and extrapolate these data to predict alloy behavior in anticipated fusion environments.

2.0 Summary

The swelling of pure copper and various copper-base alloys has been determined at 47 dpa after irradiation in FFTF-MOTA at ~450°C. Data are also becoming available at 63 dpa. The alloys tend to fall into two broad categories: those that swell appreciably, sometimes with an S-shaped behavior, and those that resist swelling to very high neutron exposures. It appears that copper may have an intrinsic swelling rate of ~1%/dpa that is often not reached because of its tendency toward saturation of swelling. The most swelling-resistant alloys examined to date are CuAl25, MZC and Cu-2.0Be.

3.0 Program

Title: Irradiation Effects Analysis (AKJ)
Principal Investigator: O. G. Doran
Affiliation: Hanford Enqineering Development Laboratory

4.0 Relevant OAFS Program Plan Task/Subtask

Subtask II.C.I, Effect of Material Parameters on Microstructure

5.0 Accomplishments and Status

5.1 Introduction

In earlier reports[1,2] the swelling of pure copper and various copper-base alloys was reported after irradiation in FFTF-MOTA to 2.69 x 10^{22} n/cm^2 (E > 0.1 MeV) at a temperature estimated to be between 420 and 450°C. For pure copper this neutron exposure yields 16 dpa. The uncertainty in temperature arose because copper would react with the liquid sodium coolant, which was maintained at 407 ± 5°C. Therefore, the packet containing the copper specimens was filled with helium gas rather than with sodium. The lack of sodium coolant leads to a somewhat higher but indetetminant level of gamma heatinq.

The composition of each alloy is qiven in Table 1. Note that for a qiven neutron exposure, copper experiences ~33% more displacements than do Fe-Cr-Ni alloys. The specimens were in two forms, that of TEM disks and miniature tensile specimens. Since both types of specimens were prepared from the same sheet stock and annealed together, no difference in behavior is anticipated.

Data are now becoming available for these same copper alloys irradiated to 47 dpa (7.6 x 10^{22} n/cm^2) and 63 dpa (1.03 x 10^{22} n/cm^2). The latter displacement level represents the continued irradiation of companion specimens that are identical to those irradiated to 16 dpa and that were irradiated in the same MOTA

capsule. The second irradiation of 47 dpa was conducted at a marginally higher displacement rate compared with that of the first irradiation, and the coolant temperature was also slightly hiqher (426 vs 407°C).

5.2 Results

Whereas, the 16 dpa data were derived from the miniature tensile specimens, the higher fluence data were extracted from the TEM disks. There was often more than one disk, allowinq for an estimate of the variability of swelling. The miniature tensile specimens in the second irradiation exhibited considerable self-welding and have been set aside for later examination. While data collection at 47 dpa is complete, data at 63 dpa are still being collected. All currently available data are shown in Table 1.

Figure 1 shows the swelling behavior observed for those alloys that exhibit a moderate-to-hiqh amount of swelling. Pure copper exhibits a possible tendency toward S-shaped behavior, reaching 31% at 63 dpa. Copper with 0.1 wt% silver swells immediately at a rate of ~1%/dpa with no perceptible incubation period, and then falls in swelling rate, reaching 47.5% at 63 dpa. The copper alloy CuAgP, with three times as much silver and small amounts of phosphorus and magnesium, swells less but with a pronounced S-shaped behavior. CuNiBe initially swelled less than pure copper or CuAg, the amount depending on the preirradiation heat treatment. Note, however, that the cold-worked and aged condition is approaching a swelling rate of ~1%/dpa.

The alloys MZC, CuBe and CuAl25 swelled much smaller amounts and exhibit some degree of scatter, as shown in Table 1. The swellinq of MZC at ~1% was shown earlier at 16 dpa to be the result of phase-related density changes and not to be the result of void swellinq.[3] The accuracy of these measurements is ±0.16%.

TABLE 1

SWELLING OF VARIOUS COMMERCIAL COPPER ALLOYS AT ~450°C

Alloy	Alloy Composition (wt%)	Condition	% Swelling 16 dpa	47 dpa	63 dpa
Cu (MARZ)	cu (99.99%)	annealed	6.5	23.3, 22.2	31.3, 30.1, 33.2
CuAg	Cu-0.1 Ag	20% CW	16.6	38.2, 35.5	47.4
CuAgP	Cu-0.3 Ag-0.06 P-008 Mg	20% CW	7.9	16.0, 16.2	17.1
CuNiBe (1/2 HT)*	Cu-1.8 Ni-0.3 Be	20% CW and aged (3 h at 480°C)	1.70	14.6, 13.9	24.6, 22.3
CuNiBe (AT)*	Cu-1.8 Ni-0.3 Be	20% CW and aged (3 h at 480°C)	0.29	3.05	5.73, 6.59
CuBe (1/2 HT)	Cu-2.0 Be	20% CW and aged (2 h at 320°C)	-0.18	0.18, 1.10, 1.18	1.01, 1.53
CuBe (AT)	Cu-2.0 Be	annealed and aged (2 h at 320°C)	-0.66	-0.45, -0.24, +0.12	-0.25, -0.43
MZC	Cu-0.9 Cr-0.1 Zr-0.05 Mq	90% CW, aqed 1/2 h at 470°C	1.03	0.79	---
Cu-A125	Cu-0.25 Al (as Al_2O_3)	20% CW	0.13	0.11, 0.32, 0.70	---
Cu-A125	Cu-0.25 Al (as Al_2O_3)	20 CW + aged 1 h at 550°C	---	0.12, 0.82	---

*1/2 HT and AT are industrv designations for half-hard and tempered, and annealed and tempered, respectively.

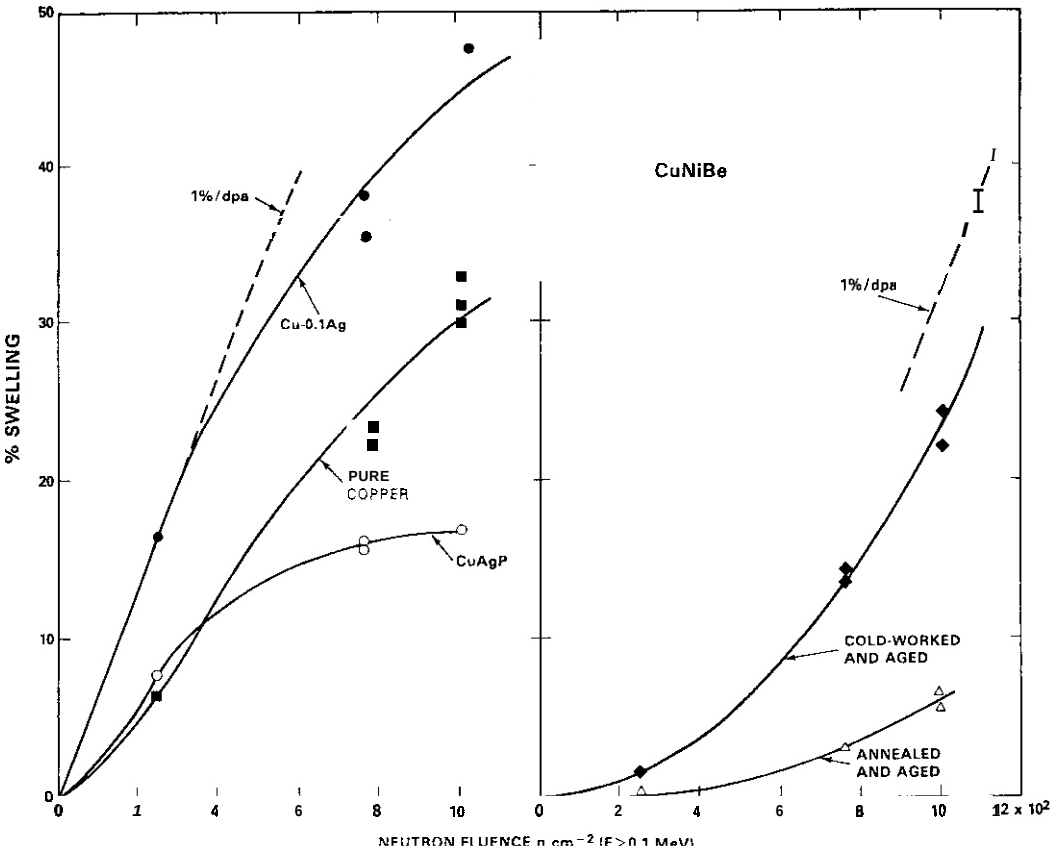

FIGURE 1. Swellinq observed in pure copper and several copper-base alloys after irradiation in FFTF at ~450°C. The data at 16 dpa were derived from miniature tensile specimens, those at hiqher doses were derived from TEM disks.

5.3 Discussion

The alloys examined in this study fall into two broad categories: those that exhibit pronounced swelling (sometimes with S-shaped behavior) with increasinq displacement level and those that resist the onset of swelling to rather high exposure levels. The S-shaped curves are typical of those seen for copper[3,4] and copper-nickel[4] alloys in charged particle irradiations, an example of which is shown in Figure 2. Note also that Figure 2 shows that addition of one atomic percent silver leads to a complete loss of the incubation period durinq electron irradiation at 250°C and the development of a linear-with-dose swelling behavior.[5] This same trend was observed in the current neutron irradiation study at ~450°C with two important exceptions. First, only 0.1 wt% (0.06 atomic percent) silver is needed to eliminate the incubation period. Second, at swelling levels greater than that reached in the electron irradiation experiment, a tendency toward saturation eventually develops.

If one ignores the possible effect of phosphorus and maqnesium, comparison of the swelling of the CuAg and CuAqP alloys suggests that increasing the level of silver leads to a subsequent decrease in swelling. A similar conclusion was reached in a study wherein 200 KeV copper ions were used to cause swelling in Copper binary alloys. Leister[5] found that 0.1 atomic percent of Ag, Au, Sb, Ni, Be and Pt all caused increases in swelling compared with that of pure copper, but that 1.0 atomic percent of any of these solutes yielded a relative decrease in swellinq.

The tendency toward saturation observed in both charqed particle and neutron irradiations of pure copper has also been observed in pure nickel, as shown in Figure 3. Note that the nickel alloy exhibits no incubation period when irradiated at the same temperature as that of current study, however. Nickel also tends to swell at ~1%/dpa before the onset of saturation behavior.

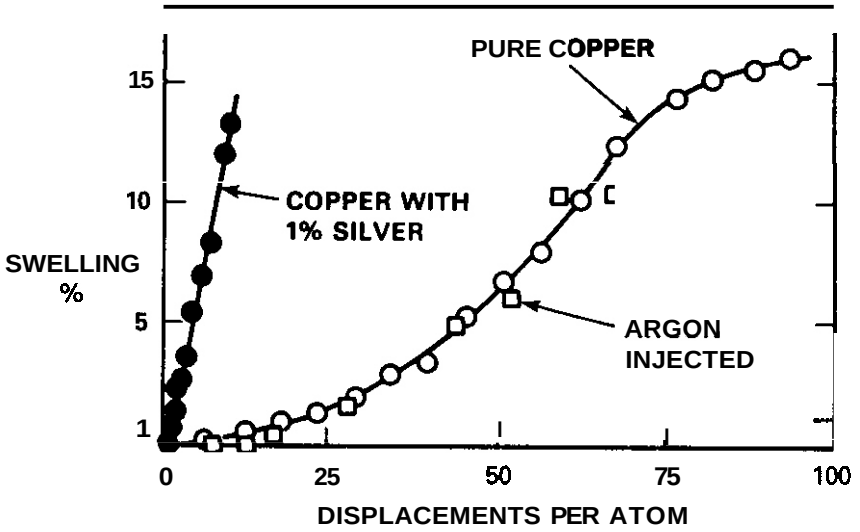

FIGURE 2. Swelling of Pure copper and copper +1% silver during irradiation with 1.0-MeV electrons at ∿250°C.

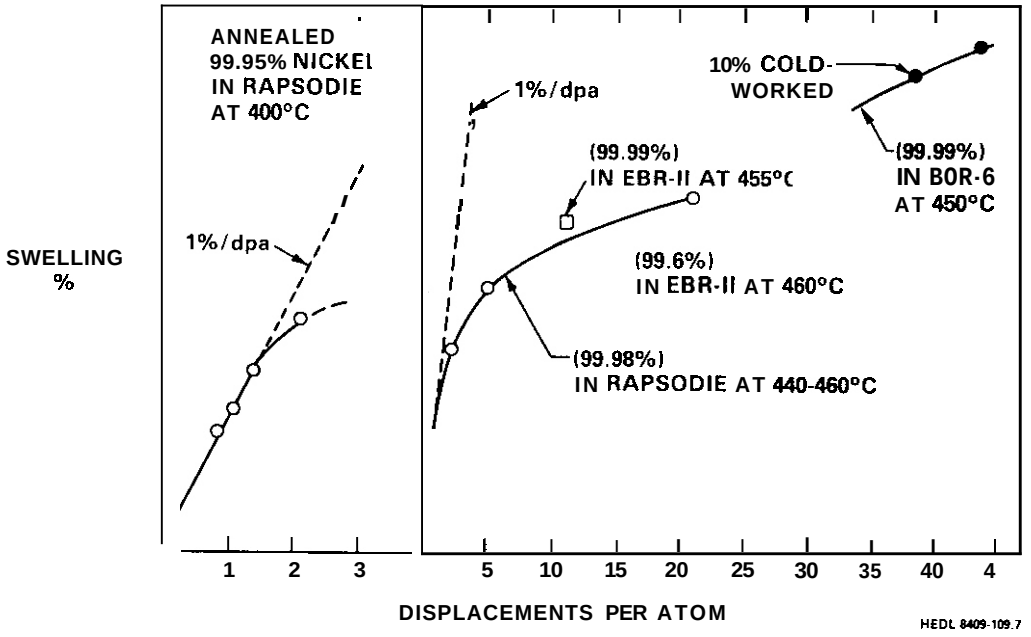

FIGURE 3. Swelling observed in relatively pure nickel in fast reactors at 400°C and at 440-460°C.[5]

5.4 Conclusions

The swelling of copper alloys at 450°C is very sensitive to the type and amount of solute and/or precipitate contained in each alloy. Pure copper tends to swell with a S-shaped behavior with increasing fluence and the incubation period can be shortened or prolonged by appropriate solute modification and thermal-mechanical treatment. The most swelling-resistant alloys examined to date are CuAl25, MZC and Cu-2.0Be.

6.0 References

1. H. R. Braqer, H. L. Heinisch, and F. A. Garner, J. Nucl. Mater. 133 & 134 (1985) pp. 676-679.

2. H. R. Braqer and F. A. Garner, "Swellinq of Commercial Copper Alloys and NiBe Irradiated in FFTF" Damage Analysis and Fundamental Studies quarterly Progress Report, DOE/ER-0046/19, November 1984, pp. 131-134.

3. H. R. Brager and F. A. Garner, "Microstructural Examination of Pure Copper and Three Copper Alloys Irradiated in FFTF," Damaqe Analysis and Fundamental Studies quarterly Progress Report, DOE/ER-0046/23, November 1985, pp. 63-70.

4. M. J. Makin in Voids Formed by Irradiation of Reactor Materials, S. F. Pugh, Ed., British Nuclear Energy Society, 1971, p. 269.

5. K. H. Leister, "Influence of Solutes on Heavy Ion Induced Void-Swelling in Binary Copper Alloys" (in German) Kernforschungzentrum Karlsruhe Report No. KFK 3499, May 1983.

6. F. A. Garner, "Swellinq of Neutron Irradiated 85Ni-15Cr at 400-650°C," in reference 2, pp. 66-73.

7.0 Future Work

Density chanqe measurements at 63 dpa will continue. Microscopy will be initiated on the high fluence specimens.

8.0 Publications

None.

NEUTRON IRRADIATION OF COPPER AND HIGH-CONDUCTIVITY COPPER ALLOYS IN EBR-II

R.J. Livak and T.G. Zocco (Los Alamos National Laboratory) and
L.W. Hobbs (Massachusetts Institute of Technology)

1.0 Objectives

Characterize the microstructural changes produced by fast neutron irradiation of copper and high-conductivity copper alloys for high heat-load applications.

2.0 *Summary*

The alumina-dispersed copper alloys (Glidcop A1-20 and A1-60) exhibited the greatest resistance to neutron damage among the six materials tested. For the conditions of this experiment (15 dpa at 385°C), the HZC alloy containing Cr and Zr did not show evidence upon TEM examination of microstructural alterations after irradiation. In contrast to the MZC alloy, the AMZIRC alloy underwent recrystallization and softening. Large, faceted voids were produced in the MARZ and oxygen-free coppers by the neutron irradiation.

3.0 Program

Title: High-Dose Neutron Radiation Damage Study of Copper Alloys for the CRFPR First Wall
(Independently Supported R & 0 - LANL)
Principal Investiyator: R.J. Livak
Affiliation: Los Alamos National Laboratory

4.0 Relevant DAFS Program Plan TaskISubtask

Subtask II.C.I Effects of Material Parameters on Microstructure

5.0 Accomplishments and Status

5.1 Introduction

Recent interest in the design of high power-density, compact magnetic fusion devices has focused attention on structural materials with good thermal conductivity required to dissipate the high thermal loads in the fusion power core. Copper-base alloys have the highest thermal conductivity of commonly available structural materials and are able to withstand relatively high thermal stresses. [1] The design of a compact reversed-field pinch reactor (CRFPR) developed at Los Alamos [2] incorporates the MZC copper alloy as the candidate first-wall material because of its satisfactory thermal-mechanical ranking along with low cost and ease of fabrication.

Very limited data are available on radiation damage effects in copper alloys exposed to nuclear reactor conditions, either fast fission or fusion neutron spectra. Because of the current interest in the use of copper alloys for fusion applications, experimental studies have recently been initiated at several laboratories. [3-6] Fast neutron damage effects in four commercial, high-conductivity copper alloys have Seen evaluated at Los Alamos for samples irradiated to about 15 dpa damage at 385°C in the EBR-II test reactor. Microstructural changes in these irradiated capper alloys, as determined by transmission electron microscopy (TEM), are described below. Changes in density [7], tensile properties [7], and electrical resistivity [8] for this set of EBR-II samples have been reported previously.

5.2 Experimental Procedure

Two elemental coppers and four dilute copper alloys were irradiated in EBR-II at 385°C to two fluences (E > 0.1 MeV) of 0.4 and 2.0 x 10^{26} n/m² corresponding to about 3 and 15 doa. The nominal comoositions of the six copper test materials (in wt%) are MARZ-grade copper - 99.999% purity, oxygen-free (OF) copper - 19.95% purity, A1-20 - 0.20% alumina, A1-60 - 0.60% alumina, AMZIRC - 0.17% Zr, and HZC - 0.5% Cr + 0.18% Zr + 0.04% Mg. Control samples were annealed at the same time and temperature (245 days at 385°C) as the full-

power days exposure of the irradiated samples. The irradiation temperature used is a realistic near-maximum temperature for high power-density, first wall designs based on copper alloys.

The prior thermomechanical treatment of the test materials has been described previously. [7] The irradiated and control samples included 3 mm diameter disks approximately 0.15 mm thick intended for the preparation of TEM foils. These samples were initially cleaned to remove any oxide using a chemical polish containing 40% nitric acid, 10% hydrochloric acid, and 50% orthophosphoric acid. The disks were then electrochemically thinned in a twin-jet, Tenupol-2 polishing unit (Stuers, Strongsville, Ohio) using an electrolyte of 25% phosphoric acid and 15% water cooled to 0-10°C at a voltage of 6-8 V dc. Thin foils of the irradiated samples were examined in a JEOL 200B electron microscope operated at an accelerating voltage of 200 kV. Both the JEOL 200B instrument and a Philips EM 400T electron microscope operated at 120 kV were used to examine the control samples.

5.3 Results

Examples of micrographs taken in the TEM examination of the irradiated and control samples are given in Figures 1-6. The control samples of the two elemental coppers had recrystallized giving a large grain size of about 50 µm diameter with few dislocations present. The two pure copper materials developed voids after the 3 dpa neutron exposure at 385°C, as shown in Figure 1. The faceted voids are uniformly distributed and are relatively large with diameters of about 200 nm. No helium bubbles were observed in over- and under-focused TEM micrographs taken of the irradiated copper samples. It was difficult to prepare thin foils of the 15 dpa fluence copper samples because of the large volume fraction of voids (6.6-6.8%. as measured by densitometry).

FIGURE 1. Bright field micrograph of the 3 dpa MARZ copper sample showing large, faceted voids produced by the neutron irradiation. Note the dislocations between the voids.

The cold-worked and age-hardened AMZIRC alloy had a well developed subgrain structure in the control samples (Figure 2a). The small, dispersed Cu_5Zr precipitates [9] are uniformly distributed in the matrix with a few larger inclusions also present. No voids were observed in over- and under- focused micrographs taken of this alloy after the 3 dpa neutron exposure; and the subgrain structure was retained with a fairly high dislocation density present (Figure 2b). Coherency strain contrast was observed around some of the small precipitates. Figure 3 shows large voids present in the AMZIRC alloy after the 15 dpa neutron exposure. The voids were observed to be inhomogeneously distributed frequently in bands; and the sample had recrystallized. There was no apparent change in the precipitate size and distribution.

The control sample of the MZC alloy also had a well developed subgrain structure as shown in Figure 4 with a few large constituent particles present and a uniform dispersion of smaller precipitates, presumably Cu_5Zr. This alloy did not show void formation after the 15 dpa neutron exposure, in contrast to the AMZIRC alloy. Comparison of the microstructure after neutron irradiation to 15 dpa revealed no appreciable change in the dislocation substructure and the precipitate dispersion.

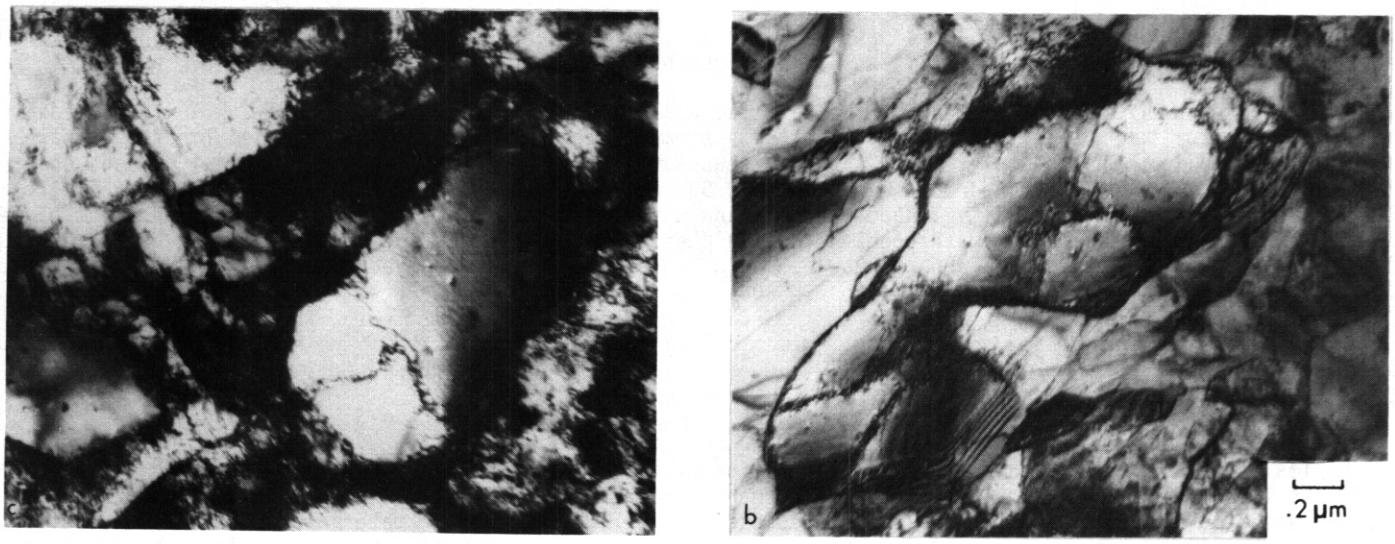

FIGURE 2. Bright field micrographs of the AMZIRC alloy showing the subgrain structure produced by cold rolling. (a) Control sample. (b) Low dose (3 dpa) sample showing retained dislocation substructure.

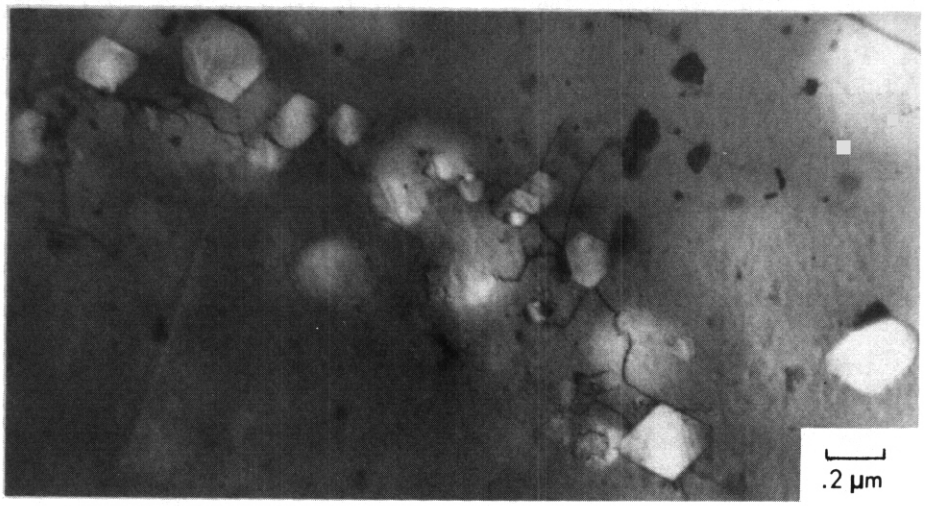

FIGURE 3. Bright field micrograph of the 15 dpa AMZIRC sample showing a localized area with large voids. The structure recrystallized after this higher fluence, neutron exposure.

FIGURE 4. Bright field micrograph of the MZC control sample showing the well-developed subgrain structure which was not altered after neutron irradiation to a damage level of 15 dpa.

The two alumina-dispersed copper alloys (A1-20 and A1-60) had similar microstructures that were heavily dislocated with a small subgrain size as shown in Figure 5. Neutron irradiation at 385°C did not produce any discernible changes in the microstructures of these alumina-dispersed alloys. No voids were observed in either the A1-20 or A1-60 samples after the 15 dpa neutron exposure, and the alumina particles appeared to remain stable under the test irradiation conditions.

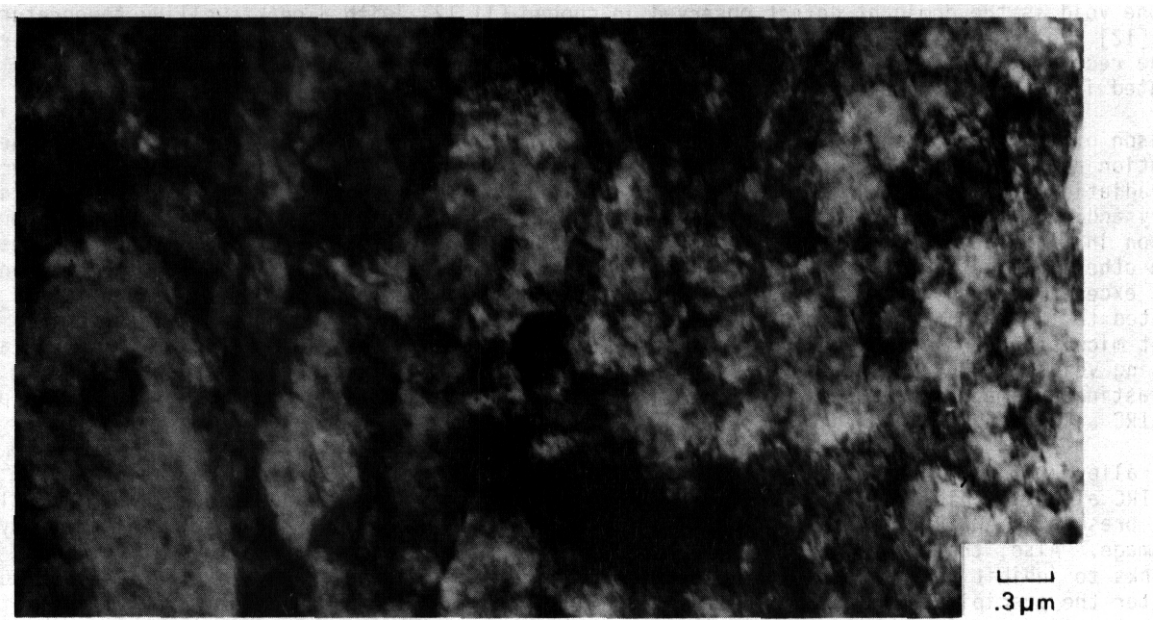

FIGURE 5. Bright field micrograph of the A1-60 control sample showing the small dislocation cell size that was not altered during irradiation.

The alumina particles produced by internal oxidation are present in the copper matrix as small (10-20 nm), triangular platelets as shown in the carbon extraction replica of Figure 6. Similar observations of alumina particles in internally oxidized copper have been reported by Ashby and Smith. [IO] As deduced from replicas made of the control samoles. the A1-20 allov contains a uniform dispersion of oarticles. whereas the A1-60 alloy has many small,' uniiormly dispersed'particles with a few, larger isolated partiiles present. Electron diffraction has identified the particles to be the gamma-Al_2O_3 phase.

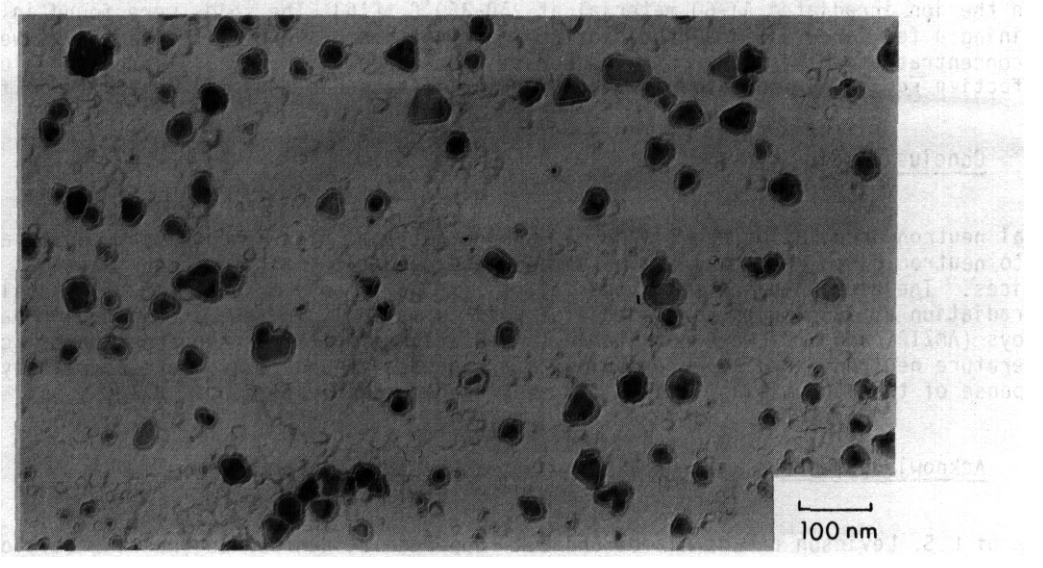

FIGURE 6. Extraction carbon replica prepared from the A1-60 control sample showing the alumina particle morphology and dispersion.

5.4 Discussion

The observed behavior of the neutron irradiated NARZ and OF coppers is in agreement with previous results reported in the literature. [11-13] For neutron irradiation above 250°C and fluences >1 x 10^{24} n/m² (E > 1 Mev), the void is the dominant defect observed in copper [11,12], with a peak swelling temperature near 335°C. [12] The irradiation temperature of 385°C is 0.48 of the absolute melting point of copper and higher than the recrystallization temperature. Large faceted voids have been observed previously in OF copper irradiated in a nuclear power reactor at 327°C. [13]

Comparison of the control and 15 dpa fluence samples of the AMZIRC alloy reveals that the fast neutron irradiation at 385°C accelerated the recrystallization of the initially cold-worked microstructure. Single ion irradiation studies on this alloy by Zinkle et al. [14] also found radiation-enhanced dislocation recovery and recrystallization. The presence of a high dislocation density appears to have suppressed void formation in the 3 dpa fluence AMZIRC sample, which had not recrystallized. Similar observations have been made in other irradiated metallic alloys where the dislocations act as efficient point defect sinks and thus prevent excess-vacancy driven void formation. The non-uniform occurrence of voids in the AMZIRC alloy irradiated to 15 dpa has also been observed in dual-ion irradiated samples of the same material. [5] No remanent microstructural heterogeneity has been identified in this material associated with the areas containing voids. Some copper-base alloys show evidence of solute or impurity banding resulting from the prior casting and mechanical working of the ingots, and this chemical segregation effect may be present in the ANZIRC alloy studied.

The MZC alloy exhibited greater resistance to radiation effects from a neutron fluence of 2 x 10^{26} n/m² than the AMZIRC alloy in this experiment at 385°C. The chromium and magnesium additions in the MZC alloy, which are not present in AMZIRC, may be contributing in some way to the greater stability of this alloy to radiation damage. Also, the higher density of precipitates in the MZC alloy may be more effective as point defect sinks to inhibit void formation. However, for higher irradiation temperatures or larger fluences that will alter the precipitate distribution, the MZC alloy is also expected to undergo recrystallization and subsequent void formation. Measured tensile properties reported previously [7] show that this alloy lost a third of its yield strength after the high-fluence irradiation, indicating that some dislocation recovery may have occurred during neutron irradiation.

The alumina-dispersed copper alloys (A1-20 and A1-60) exhibited the greatest resistance to neutron radiation damage of the six materials tested. These alloys retain good stress rupture strength at 850°C. [15] The alumina particles formed by internal oxidation were thermodynamically stable at the irradiation temperature of 385°C and effectively pinned the dislocation substructure to inhibit recovery and subsequent loss of strength.

Ion irradiation studies by Spitznagel and Davis on the A1-60 material [16] found evidence of particle resolution under silicon ion irradiation at temperatures below 350°C. Theoretical modelling of ion irradiation damage has predicted internal "sputtering" of particles caused by recoil effects. [17] Additional neutron irradiation experiments at temperatures below 400°C are necessary to determine if particle resolution will occur in these alumina-dispersed copper alloys under fast neutron irradiation. A few isolated voids were observed in the ion irradiated A1-60 material at 250-350°C. [16] The voids were found in regions of the foil containing a few large alumina particles and were not observed where the particles were smaller and denser in concentration. This observation suggests that the smaller, finely dispersed alumina particles may be more effective recombination sites for excess point defects and thus may inhibit void formation.

5.5 Conclusions

This initial neutron irradiation experiment has shown that some high-conductivity copper alloys may be resistant to neutron damage and thus are potential candidate materials far high heat-load applications in fusion devices. The alumina-dispersed copper alloys exhibited good microstructural stability to fast neutron irradiation at 385°C with no evidence of void formation. The two precipitation-hardened and cold-worked alloys (AMZIRC and NZC) were not stable to radiation effects for the experimental conditions studied. Lower temperature neutron irradiation experiments are needed to understand more completely the radiation damage response of these promising oxide-dispersed, high-conductivity copper alloys.

6.0 Acknowledgements

The efforts of L.S. Levinson at Los Alamos and E.K. Opperman at Hanford Engineering Development Laboratory in conducting the irradiation experiment in EBR-II contributed greatly to the successful completion of this research. F.W. Clinard. Jr. at Los Alamos has provided ongoing support and encouragement during the course of this program.

7.0 References

1. O.K. Harliny, G.P. Yu, N.J. Grant and J.E. Meyer, J. Nucl. Mater. 103 & 104 (1981) 127.

2. R.L. Hagenson, R.A. Krakowski, C.G. Bathke, R.L. Miller, M.J. Embrechts, N.M. Schnurr, M.E. Battat, R.J. LaBauve and J.W. Davidson, Report LA-10200-MS, Los Alamos National Laboratory (1984).

3. O.K. Harling and N.J. Grant, in: Copper and Copper Alloys for Fusion Reactor Applications, Eds. F.W Wiffen and R.E. Gold, Report CONF-830466 (USDOE, 1983) p. 353.

4. S.J. Zinkle, Ph.D. thesis, University of Wisconsin - Madison (May,1985) Report UWFDM-642.

5. J.A. Spitznagel and J.W. Davis, in: ADIP Semiannual Progress Report. September, 1984, DOE/ER-0045/13, p. 171.

6. H.R. Brayer, H.L. Heinisch and F.A. Garner. J. Nucl. Mater. 133 & 134 (1985) 676

7. R.J. Livak, T.G. Zocco and J.C. Kennedy, in: ADIP Semiannual Progress Report, March, 1985, DOE/ER-0045/14, p. 152.

8. H.M. Frost and J.C. Kennedy, in: ADIP Semiannual Progress Report, March, 1985, DOE/ER-0045/14, p. 161.

9. A.K. Lee and N.J. Grant, Mater. Sci. & Eng. 60 (1983) 213.

10. Y.F. Ashby and G.C. Smith, J. Inst. Metals, 91 (1962-63) 182.

11. J.L. Brimhall and B.J. Mastel, J. Nucl. Mater. 29 (1969) 123.

12. Y. Adda, in: Radiation Induced Voids in Metals, Eds. J.W. Corbett and L.D. Ianniello (USAEC, 1972) p. 31.

13. R.B. Adamson, W.L. Bell and P.C. Kelly, J. Nucl. Mater. 92 (1980) 149.

14. S.J. Zinkle, R.A. Dodd and G.L. Kulcinski, J. Nucl. Mater. 133 & 134 (1985) 680 and Report UWFDM-581, University of Wisconsin - Madison (1984).

15. P.K. Samal, Metal Powder Report, 39 (1984) 587

16. J.A. Spitznagel and J.W. Davis, in: ADIP Semiannual Progress Report, March, 1985, DOE/ER-0045/14, p. 168.

17. H.J. Frost and K.C. Russell, Acta Metall. 30 (1982) 953.

EXTERNAL DISTRIBUTION

UC-20 (107), 20c (56)

DOE-HQ/Office of Fusion Energy
ER-62
Washington, DC 20545

SE Parket

DOE-HQ/Office of
International Security Affairs
DP-33, Mail Stop 4C-024
Washington, DC 20585

DW Dorn

Argonne National Laboratory (3)
9700 South Cass Avenue
Argonne, IL 60439

LR Greenwood, CMT-205
A. Taylor, MST-212
BA Loomis, MST-217.

Argonne National Laboratory
EBR-II Division
Reactor Materials Section
P.O. Box 2528
Idaho Falls, ID 83403-2528

OL Porter

Battelle
Pacific Northwest Laboratory (2)
P.O. Box 999
Richland, WA 99352

JL Brimhall 306W/210
TD Chikalla PSL/1277

Carnegie-Mellon University
Metallurgical Engineering
3325 Science Hall
Pittsburgh, PA 15213

WM Garrison Jr

Centre d'Etudes de Chimie Metallurgique
15, Rue Georges-Urbain
Vitry-sur-Seine
94400 Vitry, France

G. Martin

Columbia University
School of Engineering & Applied Science
New York, NY 10027

RA Gross

Commission of the European Communities
Rue de la Loi 200
B-1049 Bruxelles, Belgium

J. Oarvas

Commission of the European Comnunities (2)
Joint Research Center
I-21020 Ispra, Varese, Italia

R. Dierckx, Physics Division
P. Schiller, Materials Science Division

Department of the Navy
Naval Research Laboratory (2)
Washington, DC 20375

JA Sprague, Code 6395
LE Steele, Code 6390

Energieonderzoek Centrum Nederland (2)
Netherlands Energy Research Foundation
Westerduinweg 3, Postbus 1
NL-1755 ZG, Petten (NH), The Netherlands

B. vanderSchaaf
W. vanWitzenburg, Materials Dept

GA Technologies Inc (3)
P.O. Box 85608
San Diego, CA 92138

JR Gilleland
GR Hopkins
T. Lechtenberg

General Dynamics/Convair
P.O. Box 85377
San Diego, CA 92138

H. Gurol, MZ 92-1072

General Electric
Advanced Nuclear Technology Operation (2)
310 DeGuign Drive
Sunnyvale, CA 94088

ANTO Library, M/C F-02
S. Vaidyanathan, M/C 5-53

Hahn-Meitner Institüt fur Kernforschung Berlin GmbH
Arbeitsgruppe C2
Glienickerstrasse 100
D-1000 Berlin 39, Federal Republic of Germany

H. Wollenberger

Hokkaido University (2)
Facility of Engineering
Kita-hu, Sapporo, 060 Japan

Michio Kiritani, Precision Engineering
Taro Takeyama, Metals Research Institute

Institiit fur Festkörperforschung der
Kernforschungsanlage Jülich GmbH
Postfach 1913
0-5170 Jülich 1, Federal Republic of Germany

P. Jung

EXTERNAL DISTRIBUTION (Cont'd)

Japan Atomic Energy Research Institute (2)
Physical Metallurgy Laboratory
Tokai Research Establishment
Tokai-mura, Naka-gun, Ibaraki-ken, 319-11 Japan

Tadao Iwata, Physics
Kensuke Shiraishi, Fuels Materials Research

Kernforschungszentrum Karlsruhe GmbH
Institut fur Material und Festkorperforschung II
Postfach 3640
D-7500 Karlsruhe 1, Federal Republic of Germany

K. Ehrlich

Kyushu University
Research Institute for Applied Mechanics
6 Kasuga-Koen, Kasuga-shi
Fukuoka, 816 Japan

Kazunori Kitajima

Lawrence Livermore National Laboratory (2)
P.O. Box 808
Livermore, CA 94550

MW Guinan, L-396
DW Heikkinen, L-397

Lawrence Livermore National Laboratory
P.O. Box 5511
Livermore, CA 94550

EC Dalder, L-643

Los Alamos National Laboratory
P.O. Box 1663
Los Alamos, NM 87544

DJ Dudziak, S-41F611

Massachusetts Institute of Technology (2)
77 Massachusetts Avenue
Cambridge, MA 02139

I-Wei Chen, 13-5118
NJ Grant, 8-407

Massachusetts Institute of Technology
Nuclear Reactor Laboratory
138 Albany St
Cambridge, MA 02139

OK Harling, NW12-204

Max-Planck-Institut fiir Plasma Physik (2)
The NET Team, IPP/NET
D-8046 Garching bei München,
Federal Republic of Germany

DR Harries
R. Toschi

McDonnell-Douglas Astronautics Co
P.O. Box 516
St. Louis, MO 63166

JW Davis

Naqoya University
Institute of Plasma Physics
Furo-chyo, Chikusa-ku,
Nagoya, 464 Japan

Taijiro Uchida

National Research Institute for Metals
Tsukuba Laboratories
1-2-1 Sengen, Sakura-mura,
Nihari-gun, Ibaraki, 305 Japan

H. Shiraishi

North Carolina State University
Box 7907
Materials Enqineerinq Department
Raleiqh, NC 27695-7907

JR Beeler Jr

Oak Ridqe National Laboratory (7)
P.O. Box X
Oak Ridge, TN 37831

ML Grossbeck
MCG Hall
LK Mansur
PJ Maziasz
NH Packan
RE Stoller
SJ Zinkle

Oak Ridqe National Laboratory (2)
P.O. BOX Y
Oak Ridge, TN 37831

LA Berry
RW Wiffen, FEDC Bldg

Osaka University
2-1 Yamada-oka, Suita,
Osaka, 565 Japan

Kenji Sumita, Nuclear Enqineerinq

Osaka University
8-1 Mihogaoka
Ibaraki, Osaka, 567 Japan

Toichi Okada, Institute of
Scientific & Industrial Research

Pacific Sierra Research Corp
1104B Camino Del Mar
Del Mar, CA 92014

RD Stevenson

EXTERNAL DISTRIBUTION (Cont'd)

Princeton University (2)
Plasma Physics Laboratory
Forrestal Campus
P.O. Box 451
Princeton, NJ 08544

JPF Conrads
Long-poe Ku

Risd National Laboratory
Postfach 49
DK-4000 Roskilde, Denmark

BN Singh

Rockwell International Corp
Rocketdyne Division
6633 Canoga Avenue
Canoga Park, CA 91304

OW Kneff, NA02

Sandia National Laboratories
Livermore, CA 94550

WG Wolfer

Science University of Tokyo
Faculty of Engineering
Kagurazaka, Shinjuku-ku,
Tokyo, 162 Japan

RR Hasiguti

Studiecentrum voor Kernenergie
Centre d'Etude de l'Energie Nucleaire
Boeretang 200
8-2400 Mol, Belgium

J. Nihoul

Swiss Federal Institute
for Reactor Research (2)
CH-5303 Wurenlingen, Switzerland

WV Green
M. Victoria

Tohoku University (2)
Research Institute for Iron,
Steel and Other Metals
2-1-1 Katahira, Sendai, 980 Japan

Katunori Abe
Hideki Matsui

Tokyo Institute of Technology
Research Laboratory for Nuclear Reactors
12-1, 2-chome, O-Okayama
Meguro-ku, Tokyo, 152 Japan

Kazutaka Kawamura

United Kingdom Atomic Energy Authority
Atomic Energy Research Establishment (2)
Oxfordshire OX11 ORA, UK

R. Bullough, Theoretical Physics

United Kingdom Atomic Energy Authority
Culham Laboratory
Applied Physics 2 Technology Division
Abingdon, Oxfordshire OX14 308, UK

GJ Butterworth

University of California (2)
School of Engineering and Applied Science
Boelter Hall
Los Angeles, CA 90024

RW Conn, KL-98
NM Ghoniem, KH-01

University of Michigan
Nuclear Engineering
Ann Arbor, MI 48109

T. Kammash

University of Missouri
Dept of Nuclear Engineering
Rolla, YO 65401

A. Kumar

University of Tokyo (3)
3-1, Hongo 7-chome,
Bunkyo-ku, Tokyo, 113 Japan

Naohira Igata, Met & Materials Science
Shiori Ishino, Nuclear Engineering
Shuichi Iwata, Nuclear Engineering

University of Virginia
Dept of Materials Science
Thornton Hall
Charlottesville. VA 22901

WA Jesser

Westinghouse
Advanced Energy Systems Division
Fuels Materials Technology
P.O. Box 10864
Pittsburgh, PA 15236

A. Boltax, Manager

Westinghouse
Research and Development Center
1310 Beulah Road
Pittsburgh, PA 15235

JA Spitznagel

INTERNAL DISTRIBUTION

DOE-RL/AMF
Site & Laboratory Management Division (SMD)
Laboratory Management & Technolagy
Services Branch
FED/210-B

KR Absher, Chief

HEDL (24)

HR Brager	W/A-58	RM Mann	W/A-58
LL Carter	W/B-47	WN McElroy	W/C-39
DG Doran (5)	W/A-57	RW Powell	VIA-58
FA Garner	W/A-58	RJ Puigh	W/A-58
DS Gelles	W/A-58	FA Schmittrath	W/A-58
R. Gold	W/C-39	WF Sheely	W/C-20
ML Hamilton	W/A-65	RL Simons	W/A-65
HL Heinisch	W/A-58	HH Yoshikawa/MJ Korenko	W/C-44
GD Johnson	WIA-65	Central Files	W/C-110
NE Kenny	W/C-115	Documentation Services	W/C-123